Model Membrane Structure and Morphology Studied by Atomic Force Microscopy

Edward Stephen Parsons

Department of Chemistry

Imperial College London

A Thesis Submitted for a Degree of Doctor of Philosophy

June 2016

Abstract

The plasma membrane is comprised of a complex mixture of lipids and proteins that most simply acts to compartmentalise the cells interior from its external environment. The structure of the membrane adopts that of the lipid bilayer motif that acts as a supporting matrix in which integral and peripheral membrane proteins can diffuse. This results in a heterogeneous and dynamic environment that has a direct impact upon biomolecular function. An understanding such a complex system is often sought through minimal models that mimic the behaviour(s) of the native membrane but with a greatly reduced number of molecular components. Despite their relative simplicity, they can yield an insight in to the key driving forces of specific membrane processes.

This thesis is concerned with the study of the structure and morphology adopted by model membrane systems, with atomic force microscopy providing a nanoscale view of the given membranes surface. Four distinct systems are studied: (i) By constructing phase-separated supported lipid bilayers with a systematic height mismatch between domains, it is demonstrated how height mismatch increases line tension, and drives the formation of smaller, more circular domains. (i) The sphingomyelin ripple phase is shown to be disrupted by cholesterol and ceramide dopants *via* two very different mechanisms, with cholesterol 'melting' the *gel*-like regions with little increase in ripple periodicity, whilst ceramide adds to the *gel* and elongates the periodicity. (iii) Thin films of inverse lipid phases are prepared and visualized, with the terminating lattice observable for the bicontinuous cubic phase of pure monoolein, although imaging of other inverse lattices remains elusive. (iv) It is shown that cholesterol is not required for collapse of the intermedilysin pre-pore complex prior to perforation, thus uncovering this collapse as a distinct mechanistic step. Each of these systems studied demonstrate the power of model systems in revealing the physicochemical behaviour that underpins membrane processes.

I, Edward Stephen Parsons, declare that all the work presented in this thesis is my own, except where otherwise stated.

Acknowledgements

First and foremost, I would like to thank John Seddon who has encouraged me to work on such a variety of interesting projects whilst providing a wealth of expertise and insight in membrane biophysics. I'd also like to thank Jane Saffell, Paul Luckham and Robin Leatherbarrow, who along with John, gave me the opportunity to do this PhD, and didn't complain when I followed my own scientific interests. I'd like to thank Nick Brooks, who inadvertently became somewhat of a supervisor, and Doryen Bubeck, who gave me the means and inspiration to work with protein pores in my final year.

Many of the projects I've worked on would not have been possible without a number of people. I am indebted to Nicola McCarthy, Hanna Barriga, Courtney Boyd and Arwen Tyler, who were integral to my research at various stages along the way.

I'd like to thank my failed business partners, Yuval Elani and Ben Amor; although we didn't solve the fatburg crisis, we had a good time trying.

Beyond the lab, I've had an amazing experience at Imperial, which is in the most part down to the company I've shared it with. Notable mentions to Nakai, Arwen, Kez, Nicola, Yuval, Ben, Doug, Norman, Hugh, Jim, Ali, Jenny, Dan, and everyone else in ICB and/or MBG that I've crossed paths with.

Finally, I'd like to thank my parents and sister, who have tolerated a PhD student for the past four years..

List of Publications

1. H.M.G. Barriga, E.S. Parsons, N.L.C. McCarthy, O. Ces, J.M. Seddon, R.V. Law and N.J. Brooks. Pressure–Temperature Phase Behavior of Mixtures of Natural Sphingomyelin and Ceramide Extracts. *Langmuir* **31**, 3678–3686 (2015).

2. A.I.I. Tyler, H.M.G. Barriga, E.S. Parsons, N.L.C. McCarthy, O. Ces, R.V. Law, N.J. Brooks and J.M. Seddon. Electrostatic swelling of bicontinuous cubic lipid phases. *Soft Matter* **11**, 3279–3286 (2015).

3. H.M.G. Barriga, A.I.I. Tyler, N.L.C. McCarthy, E.S. Parsons, O. Ces, R.V. Law, J.M. Seddon and N.J. Brooks. Temperature and pressure tuneable swollen bicontinuous cubic phases approaching nature's length scales. *Soft Matter* **11**, 600–607 (2015).

4. C. Boyd, E.S. Parsons, R.A.G. Smith, J.M. Seddon, O. Ces and D. Bubeck. Disentangling the roles of cholesterol and CD59 in intermedilysin pore formation. *Accepted for publication in Scientific Reports*.

Table of Contents

List of Figures

List of Tables

List of Abbreviations

AFM	Atomic force microscopy
CDC	Cholesterol dependent cytolysin
Cer	Ceramide
Chol	Cholesterol
CMC	Critical micelle concentration
DAPC	1,2-Diarachidoyl-sn-glycero-3-phosphocholine
DIB	Droplet interface bilayer
DLPC	1,2-dilauroyl-sn-glycero-3-phosphocholine
DMPC	1,2-dimyristoyl-sn-glycero-3-phosphocholine
DOG	1,2-dioleoylglycerol
DOPC	1,2-dioleoyl-sn-glycero-3-phosphocholine
DOPE	1,2-dioleoyl-sn-glycero-3-phosphoethanolamine
DOPG	1,2-dioleoyl-sn-glycero-3-phospho-(1'-rac-glycerol)
DOPS	1,2-dioleoyl-sn-glycero-3-phospho-L-serine
DPhPC	1,2-diphytanoyl-sn-glycero-3-phosphocholine
DPPC	1,2-dipalmitoyl-sn-glycero-3-phosphocholine
DSC	Differential scanning calorimetry
DSPC	1,2-distearoyl-sn-glycero-3-phosphocholine
ESCRT	Endosomal sorting complexes required for transport
FFT	Fast Fourier transform
GI-SAXS	Grazing incidence small angle X-ray scattering
GPI	Glycophosphatidylinisitol
GUV	Giant unilamellar vesicle
HOPG	Highly oriented pyrolytic graphite
ILY	Intermedilysin
MO	Monoolein
NMR	Nuclear magnetic resonance
PC	Phosphocholine
PE	Phosphoethanolamine
PFT	Pore forming toxin
PS	Phosphoserine
SAXS	Small-angle X-ray scattering
SLB	Supported lipid bilayer
SM	Sphingomyelin
SNARE	Soluble NSF Attachment Protein
SPM	Scanning probe microscopy

STM	Scanning tunnelling microscopy
SUV	Small unilamellar vesicle
WAXS	Wide-angle X-ray scattering

Chapter 1: Introduction

The work presented in this thesis concerns the construction and study of model membrane systems, in an attempt to gain a deeper understanding of the underlying principles at play in the native plasma membrane *in vivo*. To set the scene for these investigations, a description of the plasma membrane and associated biological phenomena is given. The unique physicochemical properties of lipids are presented with the view that their resulting lyotropic phase behavior has a direct impact upon membrane structure and function. A brief review of the model membrane systems that have previously given rise to physical insight and novel applications in biology is presented, with an emphasis placed on how atomic force microscopy has emerged as a powerful tool in this field.

1.1 The plasma membrane

The plasma membrane represents the physical barrier between a cell's internal contents and the environmental exterior, and despite its most basic form comprising a bilayer motif that possesses a thickness of only a few tens of ångströms, the membrane has evolved to selectively allow the passage of ions, small molecules and larger macromolecules into and out of the cells interior. In addition, in cooperation with its integral, peripheral and lipid-anchored membrane proteins, it mediates cellular adhesion and communication, and can undergo major remodeling such as in the fission and fusion that occurs during endo- and exocytosis. The lipid bilayer is comprised of a plethora of of distinct lipid species that make up this two dimensional matrix (the 'lipidome'), and it is now increasingly accepted that the physicochemical properties of these amphiphillic molecules allows them to play an active role *in vivo*.

1.1.1 A two-dimensional lipid bilayer matrix

The plasma membrane was first proposed to be comprised of fluid lipid bilayer by Singer and Nicholson in 1972[1], in which rapid diffusion of membrane lipids and proteins can occur within the plane of the membrane, as depicted in the schematic shown in *figure 1.1*. This elegant model of the plasma membrane can be seen to arise from the

amphiphillic nature of the lipid molecules from which it is built, which possess a hydrophilic headgroup attached to hydrophobic, hydrocarbon chains. In order to prevent direct contact between the hydrophobic chains and their aqueous surrounds, the lipid molecules self-assembly into the bilayer motif with a hydrophobic interior and hydrophilic lipid headgroups at the aqueous interface. The energetic driving force for this process of self-assembly is the hydrophobic effect, which is not fully understood but for which a qualitative description invokes the entropic cost of placing the polar, hydrogen-bonding aqueous phase against a non-polar, hydrophobic interface. By reducing the amount of configurational space available to the water molecules for hydrogen bonding, a hydrophobic interface introduces a degree of order to the system that has an associated entropic cost. The hydrophobic effect therefore acts to shield hydrophobic surfaces from their aqueous surround, thus reducing the free energy of the system.

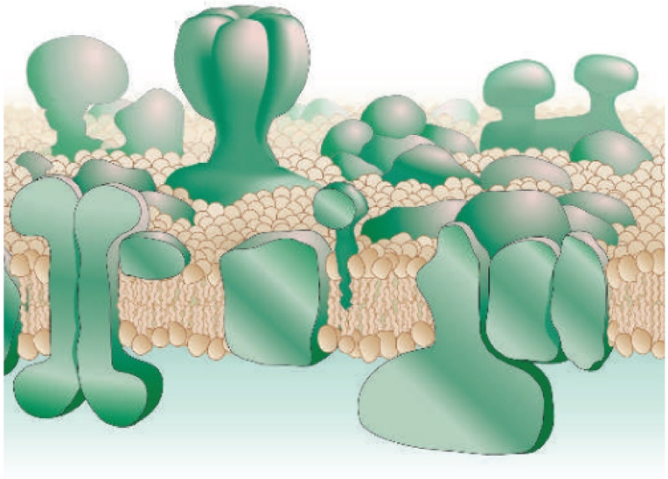

Figure 1.1: Schematic showing the structure of the plasma membrane, in which the fluid lipid bilayer matrix harbours membrane proteins that are mobile within the plane of the membrane. *Figure taken from*: D.M. Engelman, *Nature* **438**, 578–580 (2005).

The fluid nature of the lipid bilayer allows for lateral diffusion of its constituents, facilitating dynamic membrane processes[2] and gives rise to interesting biophysical phenomenon such as the clustering of membrane-bound adhesion molecules at a cell junctions[3], in which the diffusivity within the membrane directly results in stronger membrane-membrane adhesion. The amphiphillic structure of the lipid molecules

allows the resulting bilayer to accommodate proteins that are integral to the membrane, with a transmembrane region that spans the bilayer by displaying a hydrophobic interface towards the bilayers interior. Additionally, peripheral proteins can associate with the membrane by binding directly to lipid headgroups (e.g. GPI anchored proteins) or to integral membrane proteins, whilst further membrane associated proteins display a lipid anchor *via* post-translational modification (e.g. myristoylated proteins). The plasma membrane is thus a crowded place[4] in which there is a dynamic interplay between its molecular constituents.

1.1.2 Lipid 'rafts'

The lipid raft hypothesis has extended the model of the plasma membrane as a two-dimensional fluid matrix to encompass lateral compartmentalization, in which microdomains that are enriched in sphingolipids and cholesterol emerge[5-7] to focus the bioactivity of associated membrane proteins, as shown in *figure 1.2* below. Such lipid rafts have been defined as being ca. 5-200 nm in size and transient in nature, rendering their detection *in vivo* elusive as they lie at length scales beneath the diffraction limit. The advent of super-resolution microscopy has allowed for the detection of cholesterol-rich molecular complexes with a lifetime of 10-20 ms *in vivo*[8], whilst a wealth of biophysical studies on model membrane systems have comprehensively characterized the lateral phase separation that occurs within the plane of the membrane[9,10].

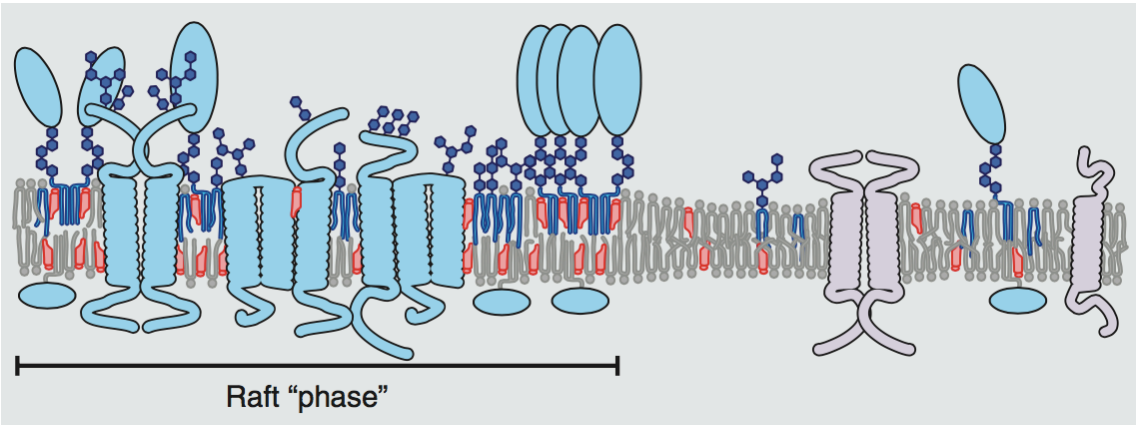

Figure 1.2: Schematic showing lipid rafts, enhanced in sphingolipids and cholesterol, and which focus the bioactivity of raft-associating membrane proteins. *Figure taken from*: D. Lingwood *et* al., *Science* **327**, 46–50 (2010).

A plethora of techniques have been applied to model membranes, including fluorescence microscopy of giant unilamellar vesicles (GUVs)[9], atomic force microscopy of supported lipid bilayers[10,11] and small-angle x-ray scattering[12,13] of stacked lipid bilayers, with the view that the underlying principles that dictate the size, morphology and lifetime of domains are somewhat transferrable to cellular membranes. The consensus is emerging that lipid rafts do indeed exist *in vivo*[7], but whether this is on a timescale that is relevant to biomolecular processes in the dynamic, out-of-equilibrium environment of the cell membrane remains to be seen.

1.1.3 Membrane remodeling

When considering the morphology of the plasma membrane, it is revealing to study processes in which the membrane contorts to achieve a specific biological function. The activation energies that are placed on the membrane during such processes can be lowered by the presence of certain lipid species that have specific physicochemical properties (such as a stored curvature elastic stress[14]) when present in a planar bilayer. Such processes include endo- and exocyctosis, in which the membrane is remodeled to accommodate vesicle fusion or fission, requiring a high degree of curvature at the point of fusion/fission and a significant energetic barrier that must be overcome. The formation of a pore within the lipid bilayer to allow for transport across the membrane represents another remodeling process that is energetically unfavorable, and occurs spontaneously but with low probability[15]. Finally, transport of a lipid species across the plane of the bilayer to the opposing leaflet (referred to as 'flip-flop') requires a hydrophilic head group to be transported through the hydrocarbon chain region[16]. All of these membrane remodeling processes mentioned have associated proteins that catalyze the process or provide energy directly *via* structural transformations, with SNARE proteins mediating membrane fusion[17], the ESCRT proteins driving membrane fission[18], pore-forming proteins creating and stabilizing membrane pores[19] and flippases transported lipids across the plane of the membrane[20]. Although macromolecular protein machinery is generally required to remodel the membrane, it is accepted that the lipidome has a functional role in allowing for the morphological changes of the membrane to take place.

1.2 Lipids and lyotropic phase behavior

Despite the apparent molecular simplicity of a lipid molecule, which is most simply defined as comprising a hydrophilic, polar headgroup attached to a non-polar, hydrocarbon chain, the lipidome is vast and contains thousands of distinct molecular species[21]. The biological function of this extensive lipid diversity remains unclear[22], and an understanding has been sought by reducing the membrane to its molecular constituents as a means of studying their individual contributions to the collective behavior of the cell membrane. As such, it is helpful to classify lipid species both by their chemical constituents and their physical properties.

1.2.1 Phospholipids, sphingolipids and sterols

The chemical space occupied by membrane lipids is vast, with combinations arising from differing headgroups and hydrocarbon tails resulting in a eukaryotic lipidome of over 1000 distinct species[23,24] that can be grouped according to their chemical features. In light of this thesis, they can be largely classified into three distinct types; (i) phospholipids, in which hydrocarbon chains are bound to the phosphate headgroup *via* a glycerol linkage, (ii) sphingolipids, in which a sphingosine backbone is linked to a fatty acid chain and a glycerol- or phospholipid headgroup, and (iii) sterols, in which a hydroxyl group comprises the headgroup of the rigid sterol ring. Each of these lipid species has their own subclass(es), but for the purposes of this thesis will be outlined briefly, with the chemical structure of distinct lipid species presented as appropriate in the following chapters.

Phospholipids represent the major lipid species of the cell membrane[22], with the distinct chemical entities that collectively constitute a phospholipid shown in *figure 1.3* below. Their hydrophobic region is comprised of a diacylglycerol that harbors saturated and *cis*-unsaturated hydrocarbon chains of varying lengths; longer hydrocarbon chains favour the crystalline packing of the gel (L_β) phase, whilst a cis-unsaturated carbon-carbon bond introduces a kink into the hydrocarbon chain which acts to disrupt the packing and thus favours the fluid (L_D) phase. The identity of the lipid headgroup largely determines the shape of the molecule, and therefore it's propensity to form

bilayers or self-assemble into structures that accommodate higher degrees of curvature. Phosphatidylcholine accounts for over half of the phospholipid content in most eukaryotic membranes; the cylindrical molecular volume that it occupies drives the formation of bilayer structures, owing to the equal molecular area required for the packing of PC headgroups and diacylglycerol chains respectively. Conversely, phosphatidylethanolamine headgroups occupy an area that is smaller relative to that required by the hydrocarbon chains, thus giving rising to a conical molecular volume that favours curved structures (as explained in *section 1.2.2* below). Phosphoserine (PS) lipids harbour a net negative charge that largely differentiates them from the rest of the lipidome and impacts upon their ability to act as signaling molecules.

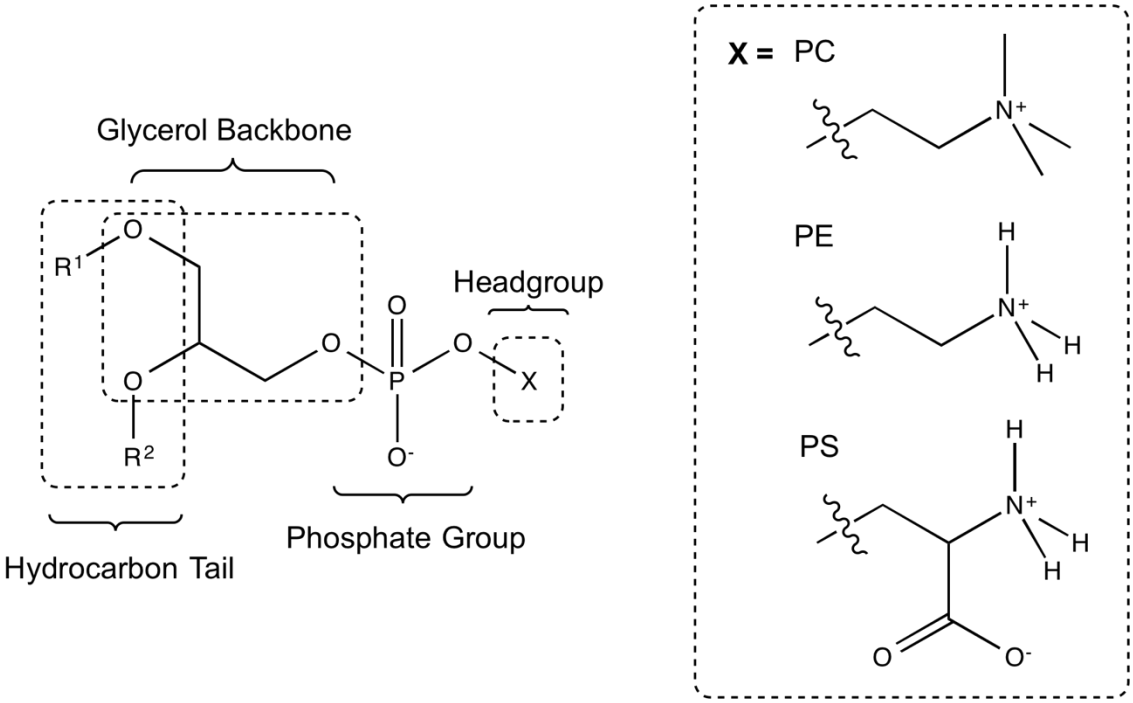

Figure 1.3: General chemical structure of phospholipids in which a phosphate group is bound to the fatty acid chains *via* a glycerol linkage. Common phospholipid lipid headgroups are also given; phosphocholine (PC), phosphoethanolamine (PE) and phosphoserine (PS).

Sphingolipids represent a further class of lipid molecules that are ubiquitous in the eukaryotic cell membrane, in which a sphingosine backbone is bound to a fatty acid chain *via* an amide bond, whilst the headgroup is functionalized either with a hydroxyl group (and thus classed a ceramide), or with a phosphocholine or phosphoethanolamine (classed as a sphingomyelin). In contrast to the phospholipids described above, the

amide linkage allows for this region of the molecule to act as both a hydrogen bond donor and acceptor, whereas the analogous ester linkage of phospholipids can only act as a hydrogen bond acceptor[25]. As a result, sphingolipids are able to self-associate with themselves through a flexible network of hydrogen bonds in the plane of the membrane. The hydrocarbon chain region of saturated sphingolipids is tightly packed, resulting in a bilayer that is ca. 30 % thicker than that of analogous unsaturated phospholipids[25]. In addition, the interface between hydrocarbon chains of neighboring sphingomyelin molecules has been reported to be relatively flatter than that between phospholipids, leading an increase in the van der Waals interactions between neighboring molecules and giving rise to the propensity of 'flat' sterol molecules to preferentially reside in sphingolipid-rich regions of the membrane[26].

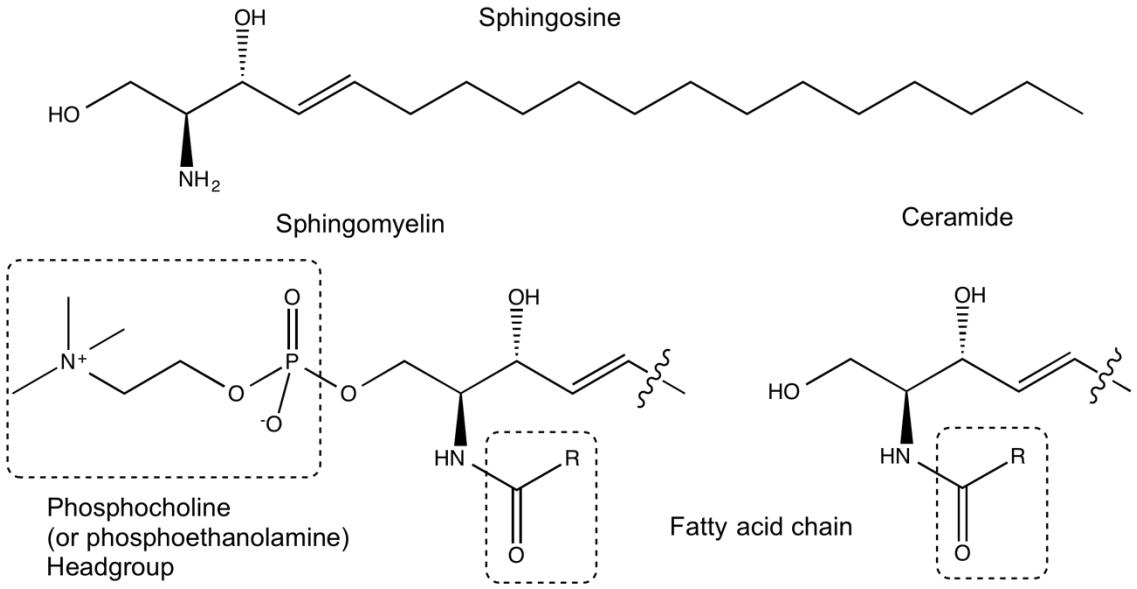

Figure 1.4: Representative chemical structure of sphingolipids, in which a sphingoid backbone (in this case sphingosine) is bound to a fatty acid chain. The presence of a phosphate linked headgroup significantly increases the hydrophilicity of sphingomyelin relative to ceramide.

Sterol lipids, based upon the sterol backbone of four fused hydrocarbon rings (as shown with cholesterol as an example in *figure 1.5* below), are significantly more hydrophobic than the other lipids that make up the plasma membrane owing to its headgroup being functionalized with a single hydroxyl. The rigid, non-polar nature of the sterol molecules allows it to penetrate deep within the lipid bilayer, strongly interacting with the hydrocarbon chains of neighboring lipid molecules and exerting a phase-modulating

effect. In proximity with long saturated chains, which favor the formation of the gel (L_β) phase, cholesterol disrupts the long-range packing and induces the fluid (L_O) phase to form. In contrast, cholesterol exerts an ordering effect of fluid phases by forcing their hydrocarbon chains to preferentially adopt an extended, *trans* state in order to accommodate the rigid sterol backbone, giving riser to closer packing of the membrane and decreasing the permeability of the membrane towards small molecules[27].

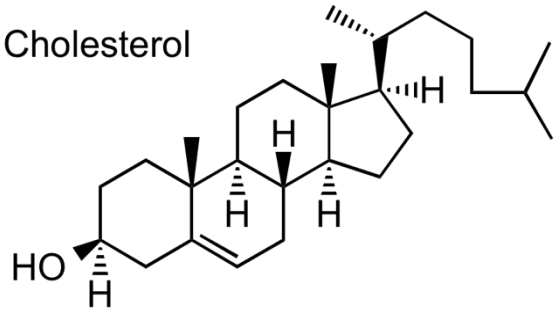

Figure 1.5: Chemical structure of cholesterol; the most abundant sterol molecule in the eukaryotic cell membrane.

Further important classifications of lipid molecules exist which will not be the subject of an in-depth description here, but are briefly touched upon in this thesis, include glycolipids[28], free fatty acids[29] and monoacylglycerols[30].

1.2.2 Headgroup size vs. hydrocarbon chain length and the lateral pressure profile

The common chemical features of lipid molecules (i.e. a hydrophillic headgroup attached to a hydrophobic tail) lend themselves to being characterized according to the relative contributions (in both size and in polarity) from the headgroup and tail regions respectively. One such classification is through the geometric packing parameter, defined as:

$$\rho = \frac{v}{a_0 l_c}$$

where ρ is the packing parameter, v is the molecular volume, a_0 is the area occupied at the interface between the lipid headgroup and it's aqueous surround and l_c is the length of the hydrocarbon chain in its critical packing (i.e. above the CMC) conformation[31]. Lipids whose headgroup area is roughly balanced with that occupied by their

hydrocarbon chains thus occupy a cylindrical volume with low interfacial curvature, and are classified as type 0 lipids with $\frac{1}{2} < \rho < 1$. Conversely, lipids with a large headgroup area relative to that occupied by the hydrocarbon chain, such as lyso-PC with a single hydrocarbon chain, curve away from the interface (positive interfacial curvature) and are classified as type I lipids with $\rho < \frac{1}{2}$. Finally, lipids whose headgroup area is relatively small compared to that occupied by the hydrocarbon chains curve towards the interface (negative interfacial curvature), and are classified as type II lipids with $\rho > 1$, as shown in *figure 1.4* below.

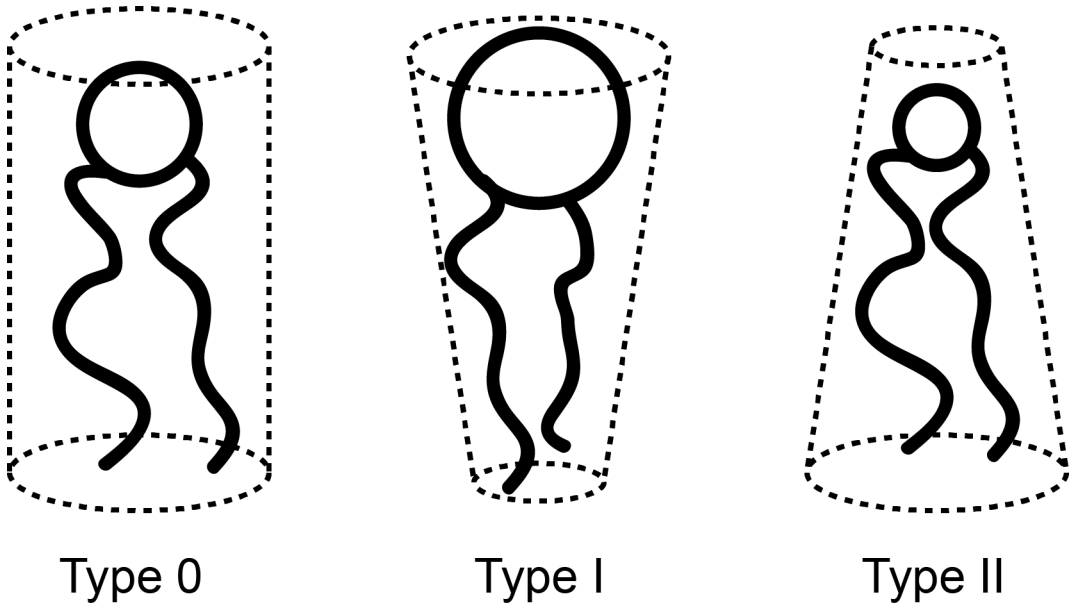

Figure 1.6: Classification of lipids based on the relative geometric contributions from the headgroup and tail regions respectively.

The shape of the individual lipid molecule, as classified in *figure 1.6* above, largely dictates the morphology of a monolayer of that give lipid. This preferred morphology is also influenced by intensive thermodynamic variables such as temperature and pressure; an increase in temperature gives rise to an increase in splay of the hydrocarbon chains, thus driving negative interfacial curvature, with pressure exerting the opposite effect. The solvating medium and its interactions with the lipid headgroups can further affect the preferred interfacial curvature[32]. By understanding the factors that influence the interfacial curvature in a given system, a qualitative view of the mechanical stresses within the plane of the lipid bilayer can be extrapolated.

The interfacial curvature of a lipid monolayer can be seen to to arise from the contributions to the lateral pressure exerted by both the headgroup and hydrocarbon chain region respectively, which compete with the interfacial tension that drives the formation of the monolayer, as shown in *figure 1.7*. Interactions between the lipid molecules within the bilayer are comprised of the steric repulsions resulting from the conformational disorder of the hydrocarbon chains, and the electrostatic, hydrogen bonding and steric interactions between the lipid headgroups. For the monolayer to exist at equilibrium, the pressures arising from these intermolecular interactions must be balanced with the interfacial tension so that there is no net pressure acting upon the membrane, thus:

$$\int \pi\,(z).\,dz = 0$$

When constrained to a lipid *bilayer*, as in the native cell membrane, the respective monolayer leaflets are unable to balance their lateral pressures by adopting a geometry that is favored collectively, and there is therefore a tension with the bilayer that is referred to as stored curvature elastic stress. The stored curvature elastic stress is determined by the lipid composition of the bilayer and is affected by any thermodynamic variable (such as temperature, pressure, pH, ionic strength etc.). These elastic stresses that exist within the membrane impact upon the function of membrane proteins[14], and it has been demonstrated that the changes in stored curvature elastic stress can act a communication line in protein-protein interactions[33].

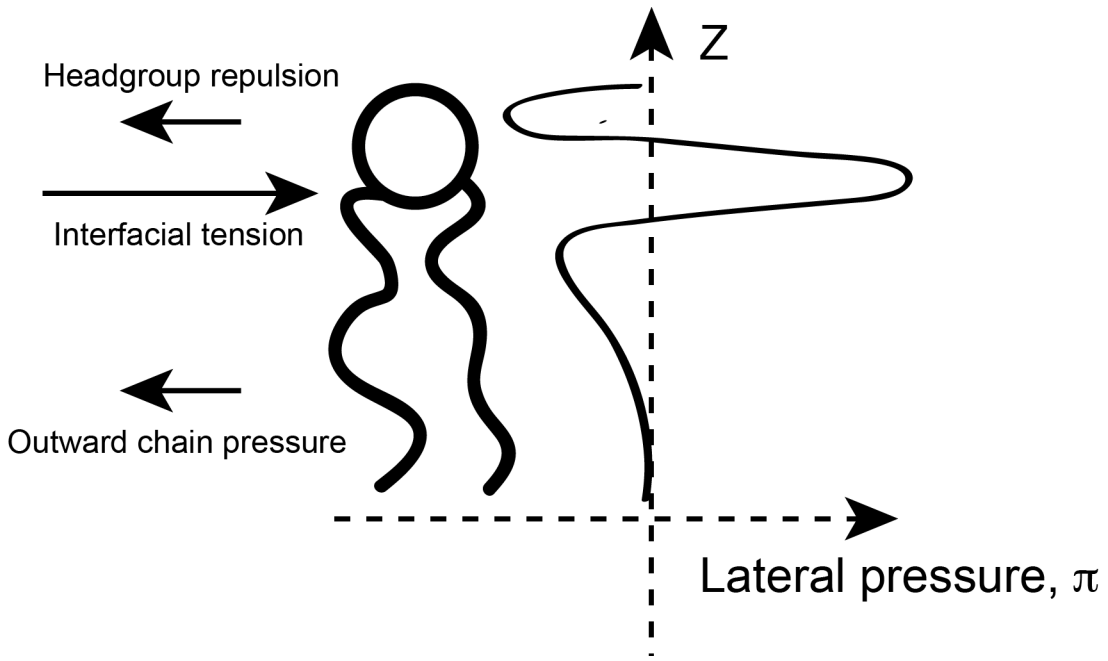

Figure 1.7: Lateral pressure profile through a lipid in a bilayer.

Beyond the lateral stresses that arise within a lipid monolayer that is constrained to a bilayer lattice, the elastic stress can be relieved with the adoption of non-lamellar liquid-crystalline phases. The spontaneous curvature of the system leads to the adoption of phases that can accommodate the lipid molecules geometric requirements.

1.2.3 Lyotropic phase behavior

The array of distinct phases that arise from hydrated lipid samples, from planar bilayers to hexagonally packed cylindrical micelles and bicontinuous cubic phases, can be rationalized in terms of geometric contributions from the individual lipid molecules as discussed previously, with the general trend in phase behavior resulting from molecular geometry shown in *figure 1.8*. Lipid molecules with a headgroup that occupies a larger area relative to their hydrocarbon chains (type I lipids, positive interfacial curvature) adopt the micellar phase, in which the lipid molecules pack into spherical aggregates where the headgroups interface with the aqueous surroundings, shielding the hydrophobic core. In additional to dispersed spherical micelles, 2D hexagonal micellar phases (H_I) can form in which the lipids are packed into a hexagonal array of cylindrical micelles. Lipids in which the headgroup area is balanced with that occupied by the hydrocarbon chains (type 0 lipids) adopt the ubiquitous bilayer motif, that can itself

adopt a variety structures within the plane of the membrane that differ in their packing and the extent of their order in their respective hydrocarbon chains. Differing degrees of order give rise to the liquid-disordered, liquid-ordered, ripple and gel lamellar phases, and are discussed in detail in subsequent chapters. Where there is a negative interfacial curvature, with a larger area occupied by the hydrocarbon chains relative to the lipid headgroup, inverse phases are formed. The 2D hexagonal inverse micellar phase (H_{II}) is formed of the close packing of cylindrical micelles with an aqueous core[32]. Further discontinuous, inverse micellar phases with the highest degree of negative interfacial curvature result from the close packing of spherical micelles in which the lipid headgroups surround an aqueous core[34], and have been found to exist in systems both with the hexagonal close packing of identical micelles[35], and cubic packing of two sets of non-identical micelles[36]. Finally, the inverse bicontinuous cubic phases represent an important class of lyotropic structures in which a lipid bilayer is draped over an infinitely periodic minimal surface and separates two interconnecting water channels that never meet[37], and are favored by a lower negative interfacial curvature than that of the H_{II} phase[34,38].

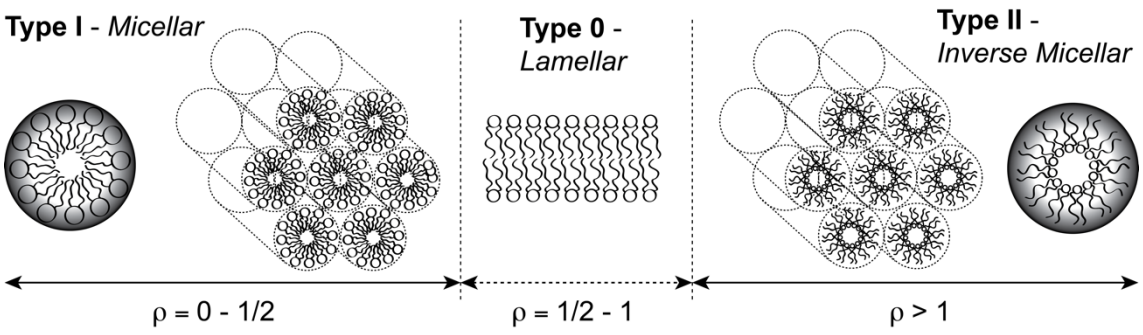

Figure 1.8: Schematic showing how the shape of the lipid molecule affects the 2- or 3-dimensional packing, and thus the resulting phase behavior; ρ is the packing parameter.

By understanding the lyotropic phase behavior of lipid systems with a minimal number of distinct molecular components, it is possible to extrapolate their molecular contributions to real cell membranes. For example, a lipids species that shows a propensity to adopt a highly curved structure can be thought to exert an associated elastic stress when confined to a planar bilayer, and can thus be a (mechanical) effector

in the function of membrane proteins. Beyond biological function, an understanding of the molecular basis of lyotropic phase behavior allows us to engineer lipid systems with specified properties[39] for use in applications such as membrane protein crystallization[40] and materials templating[41].

1.2.4 Physical parameters

In interpreting the observed behavior of biological and model systems, it is important to have a knowledge of the physical properties that arise from the supramolecular assembly of the lipid bilayer membrane[42,43]. One such description that models the membrane as a thin sheet was proposed by Helfrich[44], where three parameters are used to describe the material moduli; (i) the isothermal bending modulus that corresponds to the rigidity of the monolayer towards bending, (ii) the spontaneous curvature that describes the propensity of the monolayer to deviate from a planar sheet, and (iii) the isothermal area compressibility modulus that corresponds to the resistance of the monolayer to lateral compression. The most easily measured, and therefore most widely reported, is the bending modulus, which for a typical fluid bilayer of DOPC has a value of $K_c = 8.2 \times 10^{-20}\ J$ with an area compressibility modulus of $K_A = 260\ mN/m$,[45] with the energies required for the deformation of a fluid bilayer of the order of kT (as the lipid bilayer respresents a molecular scale system and energies can thus be scaled to J molecule^{-1}).

Beyond the mechanical properties that dictate the propensity of the membrane to deform, it must be noted that the lipid bilayer is most often found to exist as a two-dimensional fluid in which there is free diffusion of molecular species within the plane of the membrane. The diffusion coefficients of lipids confined to the liquid-disordered (L_D) and liquid-ordered (L_O) phase were reported as 3 μm^2 s^{-1} and 0.2 μm^2 s^{-1} respectively[46]. As such, measurements of the diffusion coefficients of both lipid molecules and of membrane proteins can inform the rates at which bimolecular membrane processes can be expected to occur. In combination with the mechanical properties of the membrane, these physical parameters set the scene for a confined but

dynamic environment that is ripe for deformation by macromolecular protein machinery.

1.3 Model membrane systems and their applications

In an attempt to grasp the underlying physical principles at play in the plasma membrane, model systems have been sought that display a given phenomenon but with a vastly simplified molecular composition and thus ease of making and interpreting a given measurement. This model is often reduced to two- or three-component lipid systems which exhibit certain phase behavior, or to a single protein species interacting with a lipid bilayer membrane; examples of such models are presented below.

1.3.1 Bulk lipid dispersions

The bulk phase behavior exhibited by lipids in an aqueous environment (i.e. as a *lyotropic* liquid crystal) reveals the propensity of a given lipid to curve towards or away from interface with water (as defined by the spontaneous curvature and discussed in *section 1.2*). Such phase behavior is most easily studied using ensemble, reciprocal-space techniques such as small-angle X-ray scattering (SAXS), and require a bulk lipid sample. The sample has a much greater density of lipid than found in other model membrane systems, and can thus be applied in studying lyotropic behavior at limited hydration; generally, the lipid system is found to be at full hydration at > 50 weight %water (more than sufficient to obtain signal with SAXS). In addition to the long range order present in such samples that is detected by SAXS, NMR can reveal information regarding the dynamics of the system and the molecular conformation of the constituent lipids[47], whilst DSC can probe the thermal behavior of lipid dispersions and identify a given phase transition temperature[48].

1.3.2 Synthetic vesicles as minimal models (SUVs for studying curvature, GUVs for studying phase separation, mechanical properties etc.)

Vesicle systems in which a single (i.e. unilamellar) lipid bilayer encompasses it's aqueous cargo are possibly the most widely adopted model membrane, owing to their simplicity in formation and their obvious parallels with both the native cell membrane and sub-cellular vesicles. Such vesicles system can largely be split into two distinct cases; experiments that study the behavior of a single vesicle (generally a giant unilamellar

vesicle (GUV) with a diameter on the micron scale), and those that study the ensemble behavior of a dispersion of vesicles (generally small unilamellar vesicles (SUVs) with diameters of the order of nanometers).

At a macroscopic level, giant unilamellar vesicles that are ca 10-100 μm in diameter gives access to a system that is both easily visualized by optical microscopy and of the same length scales as the native cell membrane. Further droplet-based methods have been developed in the formation of GUVs as a means of gaining fine control over their size, dispersity and asymmetry[49]. Incorporation of distinct lipid components give rise to phase separations with the vesicle membrane, that can be studied with the presence of a fluorescent dye that selectively partitions into a given phase of the membrane as shown in *figure 1.9* below[9,50]. Their relatively large size that can be easily visualized optically allows for mechanical characterization of the membrane, both *via* the contour analysis of a fluctuating vesicles[51] and by the application of a tension through the use of a micropipette aspirator[52]. Beyond studying the physical properties that arise from the lipid composition of the vesicle, GUVs can be readily functionalized with biomolecules as means to elicit a certain response or study a given biophysical phenomena; for example, functionalization of GUVs with adhesion molecules has allowed for the effects of diffusion within the membrane upon adhesive strength to be studied[3]. In the emerging field of bottom-up synthetic biology, coupling of the compartmentalizing capabilities of GUVs with the control offered by DNA origami is allowing for vesicle based nanostructures to be engineered[53].

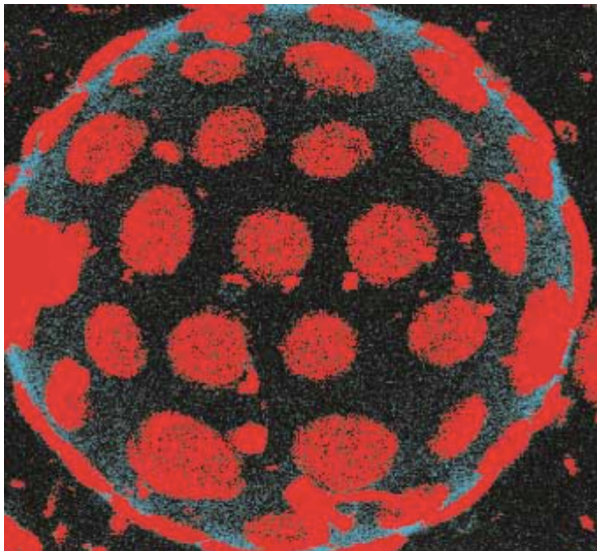

Figure 1.9: Fluorescence microscopy image of a phase separated giant unilamellar vesicle, containing liquid-ordered domains (dyed red) within a liquid-disordered matrix, that is ca. 20 μm in diameter. *Image taken from*: T. Baumgart et al., *Nature* **425**, 821–824 (2003).

Small unilamellar vesicles (SUVs) provide the means to study a single lipid bilayer membrane by ensemble techniques (cf. bulk lipid dispersions), and have been widely adopted in assays that give a fluorescence response upon transport of a given species across the membrane. One such example is in the use of vesicles of varying sizes to study the effect of membrane curvature upon protein function[54], . The size of monodisperse vesicles suspensions can be finely controlled *via* extrusion through a polycarbonate membrane with defined pores, allowing control over the curvature within a lipid bilayer by varying the size of the vesicles in suspension.

1.3.3 Droplet interface bilayers

The formation of an interface between two water-in-oil droplets, in which a lipid monolayer acts to stabilize the water-oil interface, gives rise to an interfacial lipid bilayer between the two water droplets that has been termed a droplet interface bilayer (DIB)[55,56]. This simple design allows for the content of each droplet to be loaded with a aqueous solution in which the pH, ionic strength and solubilized molecules can be readily controlled. In addition, an asymmetric bilayer can be engineered by forming a DIB

between two droplets in which a different species of lipid forms the respective interfacial monolayers[57].

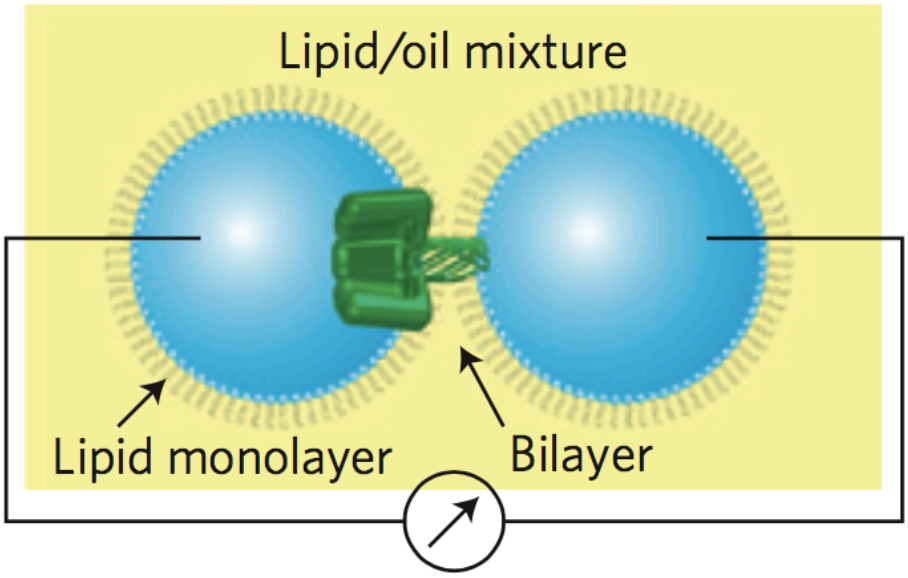

Figure 1.10: Schematic of droplet interface bilayer (DIB) that is spanned by a membrane pore, through which the current across a single pore can be detected. *Figure taken from:* D. Needham, *Nature Nanotechnology* **6**, 761–762 (2011).

DIBs have been readily adopted as a model membrane system owing to their ease of formation and interrogation by optical microscopy. In DIB format, it is possible to probe transport across the bilayer following the formation of a membrane pore, either with a fluorescent readout or with the application of a modified path-clamp setup which records the current across the bilayer, as shown in *figure 1.10* above[58]. Most recently, an interferometric based microscopy technique has been applied in the label-free imaging nanodomains at the DIB interface[59], extending the DIB model to the study of lateral phase separation within the membrane.

1.3.4 Supported lipid bilayers

Supported lipid bilayers (SLBs) have emerged both as a means of studying lipid bilayer by scanning probe microscopies[60] and of rendering biosensor surfaces biocompatible[61,62], as shown in *figure 1.11* below.

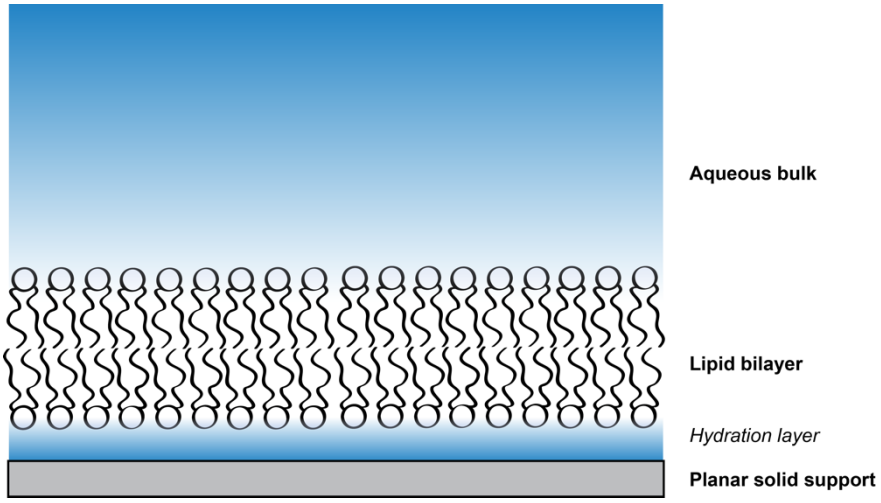

Figure 1.11: Schematic of a supported lipid bilayer, in which the lipid bilayer is separated from the underlying surface by a thin hydration layer.

There are two distinct methods of forming SLBs: (i) Langmuir-Blodgget deposition, in which the supporting surface is pulled through an water-air interface that harbors a lipid monolayer, followed by pushing the supported monolayer through the air-water interface (similarly harboring a lipid monolayer) in the aqueous bulk to give a supported lipid bilayer[63], and (ii) vesicle deposition, in which small unilamellar vesicles are incubated upon the solid surface and form a supported bilayer *via* adsorbtion, rupture and coalesence[60]. A combination of Langmuir-Blodgett deposition followed by vesicle fusion represents the simplest method in forming asymmetric supported bilayers for interrogation by AFM[64]. Further supported lipid bilayer films can be formed by spin coating the lipid onto a solid surface from solvent following by subsequent hydration[65], but have not been widely adopted as an undefined multilayer is formed.

1.4 Atomic force microscopy in membrane biophysics

The atomic force microscope (AFM) was developed as an extension of the scanning tunneling microscope (STM) that achieved true atomic resolution and won the Nobel prize in physics in 1986[66,67]. The ubiquity and applicability of AFM has arguably led it to surpass the initial expectations placed on scanning probe microscopy, and has given important insight into biological systems, ranging from the direct visualization of the double helix of DNA[68], force measurements of protein (un)folding on the timescale of molecular dynamics simulations[69] and real-time observation of myosin molecules

translocating along actin filaments[70]. As a technique that is inherently surface sensitive (which is also viewed as the main limitation of AFM), it lends itself to the study of the plasma membrane[71]. Model systems in which a native membrane extract or synthetic lipid bilayer is deposited upon an atomically smooth substrate have been most widely adopted, with both static and dynamic AFM imaging, alongside nanomechanical analysis, have provided an unprecedented view of the lipid bilayer membrane.

1.4.1 Imaging

Static imaging of supported lipid bilayers by AFM has been widely adopted, and has likely reached its resolution limit as evidenced by the reported images of individual lipid headgroups in a gel-phase DPPC bilayer[72] and of hydration layers at a domain boundary[73]. However, as the membrane is a soft and dynamic environment, the scope of AFM is much greater than the resolution attainable of gel phase bilayers. Phase-separated bilayers have been extensively studied, with the height difference of ca. 1 nm between the distinct phases easily detected by AFM[74], and has thus paved the way for studies with variable temperature as the phase separated membrane approaches a critical point[10]. An example from the literature of such phase separation is shown in *figure 1.12* below, with a corresponding schematic showing how AFM can readily detect the height difference between distinct lamellar phases. Beyond pure lipid systems, AFM imaging of the assembly of protein complexes upon the membrane surface is providing a nanoscale view of the assembly of such macromolecular machinery in near-physiological conditions[75,76].

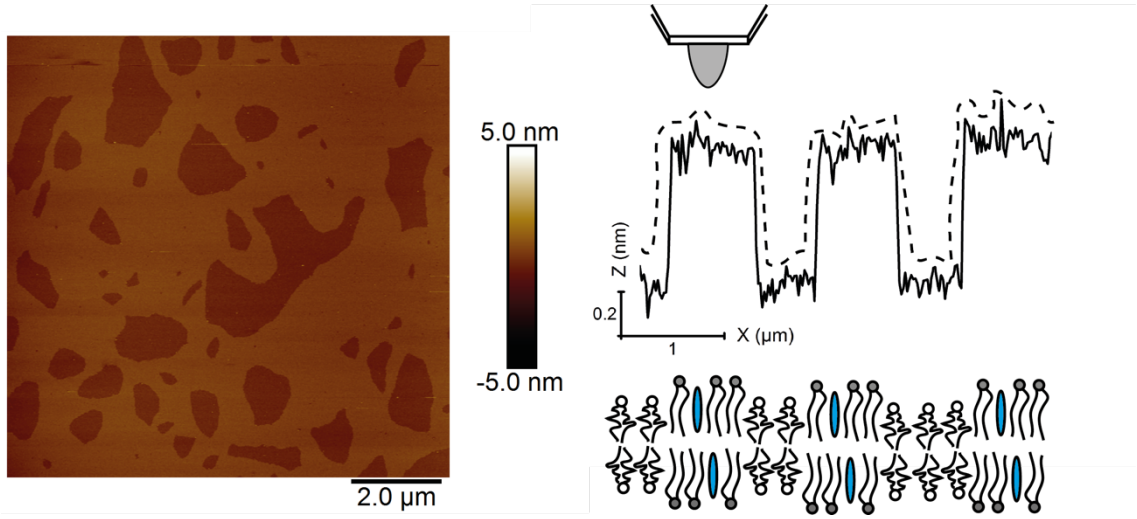

Figure 1.12: AFM image and corresponding cross-section showing phase separation in a supported lipid bilayer membrane (composed of 1:1:1 DOPC:DPPC:Chol), with a schematic demonstrating how AFM is used to visualize domains by detecting the height difference at the domain boundary with z resolution on the order of ångstroms. AFM can thus simultaneously visualize the size and morphology of microdomains whilst also providing a measurement of the height mismatch at the domain boundary, as is discussed in detail in *chapter 3*.

1.4.2 Force Mapping

In addition to the molecular scale imaging capabilities of AFM in liquid, it has also been extensively applied in studying the nanomechanical properties of model membranes owing to its intrinsic capacity to act as a force probe. By approaching and retracting the AFM probe towards and away from the surface, the force required to breakthrough the membrane can be detected, along with the inverse measurement of the adhesion between the AFM probe and the bilayer surface as the probe is retracted. The effect of the nature of the lipid headgroup, the length and (un)saturation of the hydrocarbon chains, the presence of the cholesterol and the salt concentration of the surrounding aqueous phase have all been investigated[77,78], with example force data for saturated lipid of varying hydrocarbon chain lengths shown in *figure 1.13*. Recent developments in AFM technology have led to imaging modes in which a force curve is collected for each pixel in the image, allowing for comprehensive mechanical maps of the membrane to be attained[79].

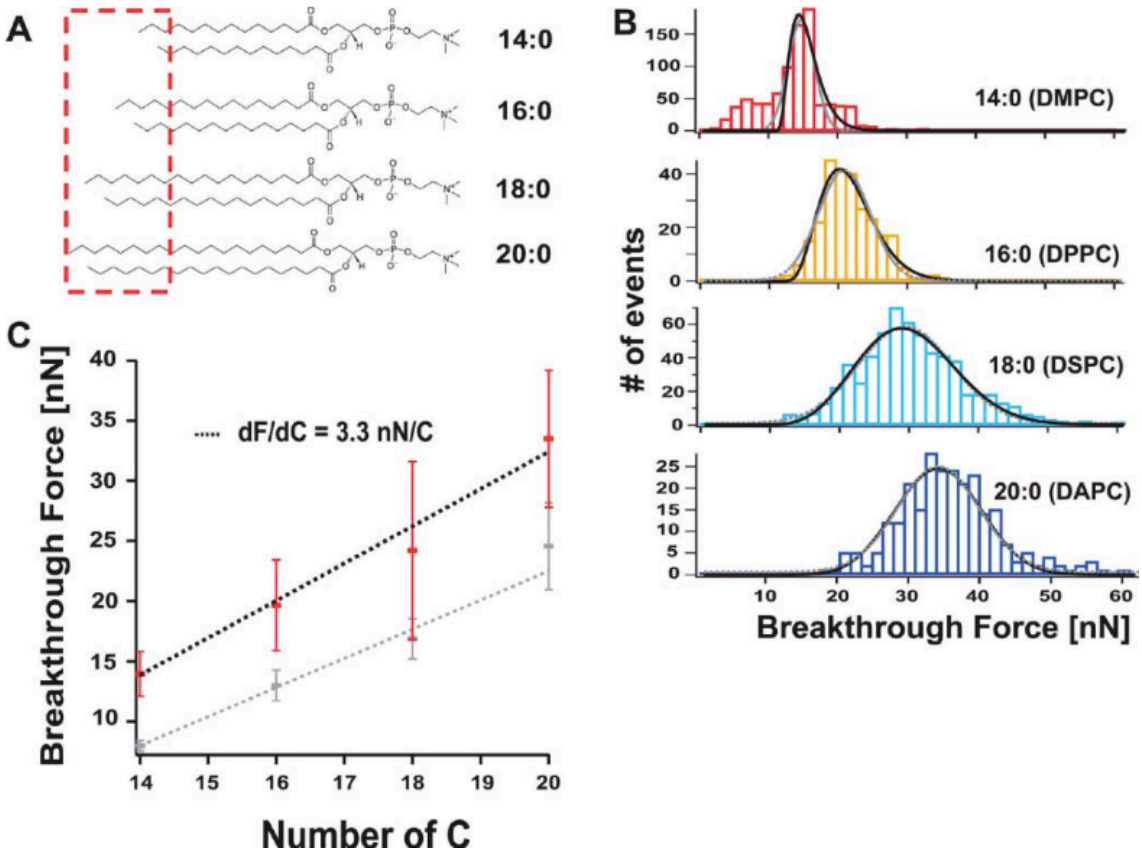

Figure 1.13: Breakthrough force data taken from supported lipid bilayers where the length of the hydrocarbon chain is systematically increasing by two carbon atoms from DMPC through DPPC and DSPC to DAPC, and should thus be contrasted with the values of breakthrough force measured in this thesis for these same lipid present in three component systems of saturated-PC:Chol:DPhPC (see chapter 3). *Figure taken from*: S. Garcia-Manyes *et al.*, *Journal of the American Chemical Society* **132**, 12874–12886 (2010).

1.4.3 High-speed AFM

Recent developments in AFM technology have led to a dramatic increase in the temporal resolution that can be obtained in the study of biomolecular processes[80], with frame rates of up to 10 Hz now attainable. Initial studies utilizing high-speed AFM were able to make real-time observations of SUVs fusing with a mica surface in the formation of a supported lipid bilayer[71], in which tubular vesicles were formed upon the surface prior to rupture to give a planar lipid bilayers. The motion of a membrane protein diffusing in a lipid bilayer has be imaged with frame rates of the order of 100 ms[81], with a view to understanding how crowding within the membrane affects the diffusion of its protein

constituents, and the impact of crowding upon specific interactions between protein interfaces.

1.5 Thesis aims

In light of the knowledge that has previously been built regarding the physical nature of lipids and the biological insights than can be gained from their model systems, this thesis aims to further apply these principles to novel problems in membrane biophysics, where AFM provides a useful tool that is further enhanced in combination with reciprocal space and calorimetric techniques. Chapter 3 concerns the study of phase-separated model membranes in which there is a height mismatch between distinct domains; how does the height mismatch, and resulting line tension, affect the size, morphology and lifetime of domains? Chapter 4 unravels the mechanism of ripple phase disruption in sphingomyelin; how does the nature of the dopant (cholesterol and ceramide respectively) affect the mechanism of ripple phase disruption as the bilayer tends towards a planar structure? Chapter 5 attempts to set out a general methodology for imaging the surface lattice of inverse lipid phases by AFM; how does the three-dimensional lattice terminate at the interface? Chapter 6 investigates the mechanism of membrane pore formation by a cytotoxic, oligomeric protein assembly, ILY; at what stage during the assembly process is cholesterol required for pore formation to proceed? Each of these problems is addressed, with an insight gained into the structure and morphology of these model membrane systems.

Chapter 2: Materials, methods and instrumentation

In order to image model lipid bilayer membranes by AFM, and to extract measurements of their (bio)physical properties, protocols for the formation of such model membranes and methods for AFM imaging of sensitive biologics in a near-physiological liquid environment were established *in-house*. This chapter outlines the materials and methods that were used in the formation of the model membranes studied, and gives a detailed account of protocols used when operating an atomic force microscope in liquid.

2.1 Materials

2.1.1 Lipids, Proteins and Aqueous Solutions

All phospholipids (DOPC, DPhPC, DLPC, DMPC, DPPC, DSPC, DAPC, egg-SM, egg-Cer, DOPE, DOPG, DOPA and DOPS) were supplied by Avanti Polar Lipids (Alabaster, Alabama USA) in powder form and stored at -20 °C prior to use. Monoolein (1-oleoyl-rac-glycerol), dioleoyl glycerol and cholesterol were supplied by Sigma-Aldrich (Dorset, UK) and stored at -20 °C prior to use. The synthetic glycolipid used in *chapter 4* was a kind gift from Prof. Rauzah Hashim (University of Malaya, Kuala Lumpa). Lipids were mixed in chloroform, which was then removed under a stream of nitrogen and dried under vacuum at -196 °C. Dry lipid films were hydrated with milliQ water (for all AFM, SAXS and DSC experiments unless otherwise stated), HPLC-grade water (for SAXS of swollen cubic phases) and buffer (for AFM of ILY pores; 200 nM NaCl, 20 mM Tris-HCl, pH 7.5). The CD59 receptor and ILY protein monomers (including the pre-pore locked and monomer locked mutants) were kindly provided by Courtney Boyd and Dr Doryen Bubeck (Imperial College London).

2.1.2 AFM consumables

Nanosensors PNP-TR contact and tapping mode probes were supplied by Windsor Scientific (Slough, UK), where each chip contained two cantilevers formed of a triangular beam, with the tip that had a specified nominal radius of < 10 nm. Resonance frequencies of the cantilever were quoted as 17 and 67 kHz, with spring constants of 0.08 and 0.32 N m^{-1} respectively. The softer, 0.08 N m^{-1} cantilevers were used for imaging in

contact mode, whilst the cantilever with higher resonant frequencies (nominally 67 kHz) were used for imaging in tapping mode in liquid. High aspect ratio Nanosensors Biotool PNP-TR probes were also supplied by Windsor Scientific (Slough, UK) and used to record tapping mode images of ILY pores (see chapter 6), with a nominal tip radius of < 8 nm and 'spike length' of 300 nm and attached to triangular beam cantilever with a resonance frequency of 67 kHz and force constant of 0.32 N m^{-1}. Mica disks, glass disks and highly oriented pyrolytic graphite (HOPG) substrates were supplied by Agar Scientific (Stansted, UK), and were cleaved with sellotape prior to use. Substrates were glued (with a Loctite™ epoxy) to stainless steel sample disks (required for magnetic attachment to the AFM scanner) with a diameter of 10 mm and also supplied by Agar Scientific (Stansted, UK). For incubation at elevated temperatures, sample disks were placed in sealed, clear, polystyrene boxes upon a Planilon membrane, also supplied by Agar Scientific (Stansted, UK).

2.2 Methods

2.2.1 Preparation of supported lipid bilayers

Supported lipid bilayers were prepared by incubation of small unilamellar vesicles (SUVs) upon the solid support (glass or mica) at temperatures above the main phase transition of the lipids in question. SUVs were formed by hydrating the thin lipid film in water or buffer at a concentration of 1 mg/ml, and vortexed to afford a cloudy suspension indicative of particulates with a diameter greater than the wavelength of visible light (i.e. > 300-700 nm). The vesicle suspension was then sonicated in a bath sonicator (Elmasonic PH350EL) at 37 kHz, at room temperature and where the power generated from sonicating generally heated the bath to ca. 40 °C. The suspension was sonicated until clarity, where the resulting vesicles were taken to have a diameter less than the wavelength of visible light; this generally took between 5 minutes and 1 hour, and varied depending upon the lipid species, the concentration and the position in the bath sonicator (i.e. whether the suspension was placed in a sonic 'hotspot'). Prior to incubation upon the solid support, calcium chloride was added to give a concentration of 5 mM, aiding the formation of a supported bilayer by bridging the negative charge of the hydrated solid surface and the phospholipid headgroup. The mica disks were

cleaved with sellotape to give a clean, atomically smooth surface. The SUV suspension (50-100 μL) was incubated upon the mica substrate in a humid chamber, ensuring that the surface was kept hydrated throughout, at a temperature above the main phase transition of the lipids concerned for 45 minutes. Upon cooling to room temperature, the surface was rinsed with 10 x volume of water/buffer, ensuring that any excess vesicles were removed from the suspension (so as to not interfere with the laser signal during AFM imaging). Any vesicles adsorbed to the supported lipid bilayer surface were generally removed by directing the flow of the rinse step parallel to the bilayer surface. Care was taken to ensure that the surface was kept hydrated at all times; dehydration leads to destruction of the supported bilayer as the hydrophilic lipid headgroups do not form an energetically favourable interface with air.

2.2.2 Preparation of lipid films

Thin inverse lipid films (that form inverse phases upon subsequent hydration), in which there is repeating unit cell of the 3d lipid structure (with the number of units cells protruding from the substrate ≥ 10) above the supporting substrate, were prepared by spin coating the lipid upon the solid support directly from solvent. Lipids were dissolved in chloroform to a final concentration of 10 mg ml^{-1}. The solid support (HOPG or glass) and secured to a metallic disk. The disk was attached to the spin coater by suction and brought up to a speed of 2000 rpm. The lipid-in-chloroform stock (10 μL) was added dropwise to the spinning surface over a period of 30 seconds, which yielded the formation of a thin film as evidenced by the appearance of Newton fringes upon the solid support, characteristic of a film thickness that is less than the wavelength of visible light. The lipid film was placed under vacuum for ≥ 1 hour to ensure the removal of any residual solvent. The film was then hydrated *in-situ* within the AFM prior to imaging for ≥ 1 hour, allowing for the film to absorb water into its interior as it adopts an inverse phase, and to reach thermal equilibrium with the AFM instrumentation. The resulting inverse lipid film was kept hydrated throughout the imaging process.

2.2.3 Preparation of protein pores

Supported lipid bilayers were prepared as described in *section 2.2.1*, with the final rinse step undertaken with Tris buffer (200 nM NaCl, 20 mM Tris-HCl, pH 7.5). The CD59 receptor and ILY monomers were mixed with a 1:1 ratio prior to incubation upon the supported lipid bilayer. CD59/ILY was added to the hydrated supported bilayer to give a final (protein) concentration of ca. 50 μM, and generally incubated at 37 °C for 1 hour (at shorter incubation times/lower temperatures, pore assembly did proceed; to capture AFM images in the final (stable) state of the given ILY species, these conditions were found to be optimal). The supported bilayer harbouring ILY oligomers was then rinsed with ca. 10 x concentration of buffer to remove any excess protein both from solution and adsorbed to the membrane surface. The resulting model membrane was brought to equilibrium with the AFM over a period of ca. 1 hour to facilitate stable, high-resolution imaging at room temperature. Care was taken to ensure that the surface was kept hydrated throughout.

2.2.4 Preparation of bulk lipid mixtures for DSC

Dry lipid powders were weighed directly into hermetic aluminum or stainless steel DSC pans (TA instruments, New Castle, Delaware USA) to give the desired lipid ratio. The lipid samples were then hydrated to 70 wt. % water and sealed under compression prior to thermal analysis. Each sample was heat-cycled *in-situ* within the DSC to ensure complete mixing and thus cooperativity of transitions.

2.2.5 Preparation of bulk lipid mixtures for SAXS

Lipid mixtures were either weighed directly from their powder form, or prepared from stock chloroform solutions (10 mg/ml). The lipids were mixed in chloroform and dried under a stream of nitrogen gas to afford a thin lipid film. The lipid film was then freeze-dried (-196 °C under vacuum) to ensure that any residual solvent was removed. The lipid film was then hydrated, generally to 70 weight % water, in either milliQ or HPLC grade purified water, dependent upon application. The hydrated lipids were vortexed and thermal cycled ≥ 10 times to ensure complete mixing. The bulk lipid mixtures were either added to glass capillaries and flame-sealed, or to Teflon spacers (in which the lipid

sample is sandwiched between two mylar windows separated by a Teflon o-ring) prior to SAXS measurement.

2.3 Instrumentation

2.3.1 Atomic force microscopy

All AFM experiments were performed using a Veeco (now Bruker) Mulitmode IV AFM equipped with both 'E' and 'J' piezoelectric scanners, for a scanning at small lengths scales with an *x*/*y* range of 5 μm and larger length scales with an *x*/*y* range of ca. 60 μm respectively. The AFM was isolated from major sources of electronic and vibrational noise by housing the instrument in a standalone laboratory, upon an anti-vibration table that was modulated by a bed of compressed air. Care was taken to ensure that all cables connecting the AFM to the external controller were free of tension, and thus their propensity to transmit vibrational noise was minimized.

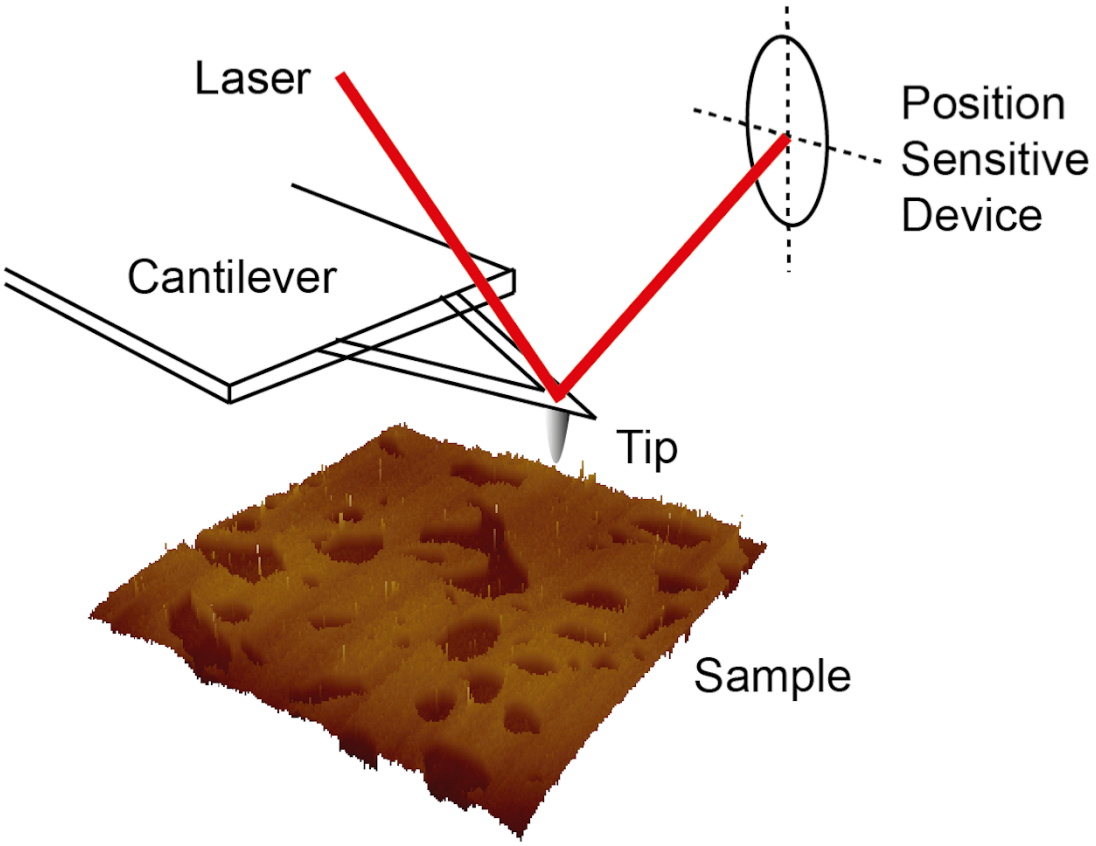

Figure 2.1: Schematic showing basic operation of an AFM, in which the deflection of the cantilever is measured *via* a reflected laser beam that strikes the position sensitive device (in this case a quadrant photodiode). The sample is scanned beneath the atomically sharp tip with the use of a piezoelectric crystal, whereby feedback back between the measured displacement of the cantilever and the displacement of the piezo ensures that force is kept constant.

2.3.1.1 Laser alignment

In order to align the laser upon the furthermost point of the AFM cantilever (which is then reflected into a quadrant photodiode), the AFM was mounted upon an optical microscope which allowed for visualization of the micrometer-scale cantilever beam. Crude alignment of the laser (*via* visualization provided by the optical microscope) was followed by finer alignment using the pattern formed by the laser when reflected off the cantilever beam as a guide; two distinct spots reflected from a triangular beam correspond to the laser hitting both beams. When on the apex of the the triangular cantilever beam, a single spot is observed, which disappears when the laser drops off the end of the cantilever. By aligning the laser towards the apex of the cantilever beam, the highest sensitivity (as can be measured as nm/V) is obtained as displacement in z is

amplified for a 'longer' beam. A similar approach is taken with rectangular beam cantilevers. Once aligned upon the apex of the cantilever, the mirror is adjusted to deflect the laser light onto the quadrant photodiode (as observed in the SUM readout on the AFM base, which is maximized when light is hitting the diode), and then adjusted to the center of the quadrant for tapping mode imaging, and vertically off center (at ca. -1.0 V) for contact mode imaging.

2.3.1.2 Operation in liquid

All AFM experiments presented in this thesis were performed in liquid, requiring the sensitive handling of lipid and protein samples that are inherently unstable at an interface with air; great care was therefore taken to ensure that samples were kept hydrated at all times (both during sample loading and data capture). Sample disks bearing an aqueous droplet were loaded upon the piezoelectric scanner *via* magnetic attachment prior to the installation of the AFM head (i.e. the hardware in which the AFM tip is loaded, containing laser source, mirror and quadrant photodiode). The AFM liquid cell (machined out of quartz) was cleaned by immersing in a bath a mild detergent (2 % solution of PPC-54 detergent concentrate) and rinsed with ≥ 10 x volume until there was no trace of residual surfactant (as any air bubbles were observed to be very unstable with a lifetime of the order of a few seconds), and air dried under a stream of nitrogen gas. The AFM cantilever was loaded into the liquid cell using fine ESD tweezers, ensuring that any static was not discharged to the delicate tip. A 1 ml syringe loaded with the given aqueous solution was inserted into the liquid cell, and the solution was pushed through until a droplet covered the AFM probe. The liquid cell was then loaded into the AFM head, taking care that the aqueous droplets covering both the model membrane surface and the AFM probe converged without dehydration of the underlying substrate. Once loaded, the laser is aligned up the AFM probe as described above and the sample is allowed to equilibrate with the AFM instrument at room temperature, to allow for the most stable imaging. Imaging is possible immediately upon loading the sample and aligning the laser, but images will appear to 'drift' over a number a frames, and with a significant difference in the applied imaging force over the course of a single frame.

2.3.1.3 Contact mode imaging

The simplest imaging procedure is by operating in 'contact mode', where the tip is in direct contact with the substrate and feedback from the piezoelectric scanner proceeds to maintain a constant deflection setpoint (i.e. a constant force) between the tip and the sample. In order to minimize force between the tip and the sample, and thus minimize damage to the soft matter sample, the deflection setpoint can be minimized; most easily achieving by decreasing the setpoint until the tip lifts off the surface, and then gently increasing to regain contact. The feedback between the piezoelectric scanner and the measured values of z can be adjusted *via* the gain settings (both proportional and integral). Proportional gain produces an output (in the piezo) that is proportional to the error in the signal between the trace and retrace lines as measured by the photodiode. Integral gain accounts for both the magnitude of the error signal and it's duration over time, whereby the integral (i.e. the sum of the error signal over time) is applied to the output in the piezo, thus eliminating the steady-state error that arises from a purely proportional feedback loop. Both integral and proportional gains are adjusted so that the trace and retrace scan lines are approximately the same (in the sense that they are tracking one another), with proportional gain generally set at a higher arbitrary value for the instrument used here. Spatial and temporal resolution are inherently interconnected, with the highest spatial resolution achieved at slow scanning rates (for example imaging at 1 (line) Hz with 1024 pixels per line), although imaging at higher frame rates can be enhanced by optimizing the gain settings. Identifying sample damage that is induced by contact mode imaging is most easily achieved by 'zooming out' to a larger scan size (provided the piezoelectric scanner has a larger range than the initial field of view), whereby any sample damage is evidenced by a characteristic 'square' in the image where the tip has perturbed the sample. Despite operating with significant shear forces between the tip and the sample that can perturb soft samples, contact mode imaging of supported lipid bilayers can provide the most direct measure of height. The height signal is taken directly from the deflection measured by the photodiode, which feeds back to the piezo in order to maintain constant deflection.

2.3.1.4 Tapping mode imaging

The more sensitive mode of imaging available with the Bruker Multimode IV AFM is tapping mode imaging, whereby the AFM tip is brought to resonance and thus intermittently contacts the sample during lateral scanning. Tapping mode (or amplitude modulation) is the AFM mode used to collect the majority of images presented in this thesis. Operation in liquid complicates the tapping mode procedure (relative to tapping mode imaging in air), as the liquid medium acts to dampen the AFM tip that is oscillating at its resonance frequency. Generally, the resonance frequency is decreased by an order of magnitude when imaging in an aqueous environment, with the emergence of additional resonance modes. In isolation from the underlying substrate, the resonance mode is selected by tuning in at that given frequency (by driving the liquid cell piezo at that same frequency), but it is offset to lower frequencies at ca. 90 % of the peak amplitude, to account for the increase in frequency as the substrate is brought into contact. Upon engaging the AFM probe with the surface, the amplitude of the cantilevers oscillation is shifted (i.e. decreased) as the probe hits the surface. The amplitude set-point can be adjusted to apply more or less force upon contact with the sample; a higher amplitude set-point corresponds to a lower imaging force and *vice versa*. As discussed for contact mode imaging, gain settings (both proportional and integral) must be adjusted to ensure that the trace and retrace line profiles are suitably tracking one another. In contrast to contact mode, the height measurement is taken *via* the motion of an oscillating cantilever, whereby the amplitude of the oscillation decreases linearly as the tip interacts with the surface beyond the initial contact regime. For soft matter samples, the height measured between two mechanically distinct phases can be skewed from its 'real' value owing to the difference is the visoelastic response between the two phases.

2.3.1.5 Force 'spectroscopy'

The AFM was further applied in collecting force data, whereby the piezoelectric scanner drives the sample to approach and retract from the AFM tip, recording both the deflection of the AFM cantilever (as measured by the quadrant photodiode, denoted Z_c) and the displacement of the piezo (and derived from the applied voltage, calibrated

against previous images of a pitch of known dimensions, denoted Z_p)[82]. The resulting deflection vs. z data can then be converted into a force *vs*. separation profile with knowledge of the spring constant of the cantilever (k_c) and the sensitivity (in nm/V) of the measurement of the deflection of the cantilever (when in the hard contact regime). The force is calculated as $F = k_c Z_c$, and plotted against the separation between the tip and the sample surface (as taken from the sum of the piezo and cantilever displacement, $D = Z_p + Z_c$), as shown in *figure* 2.2 below.

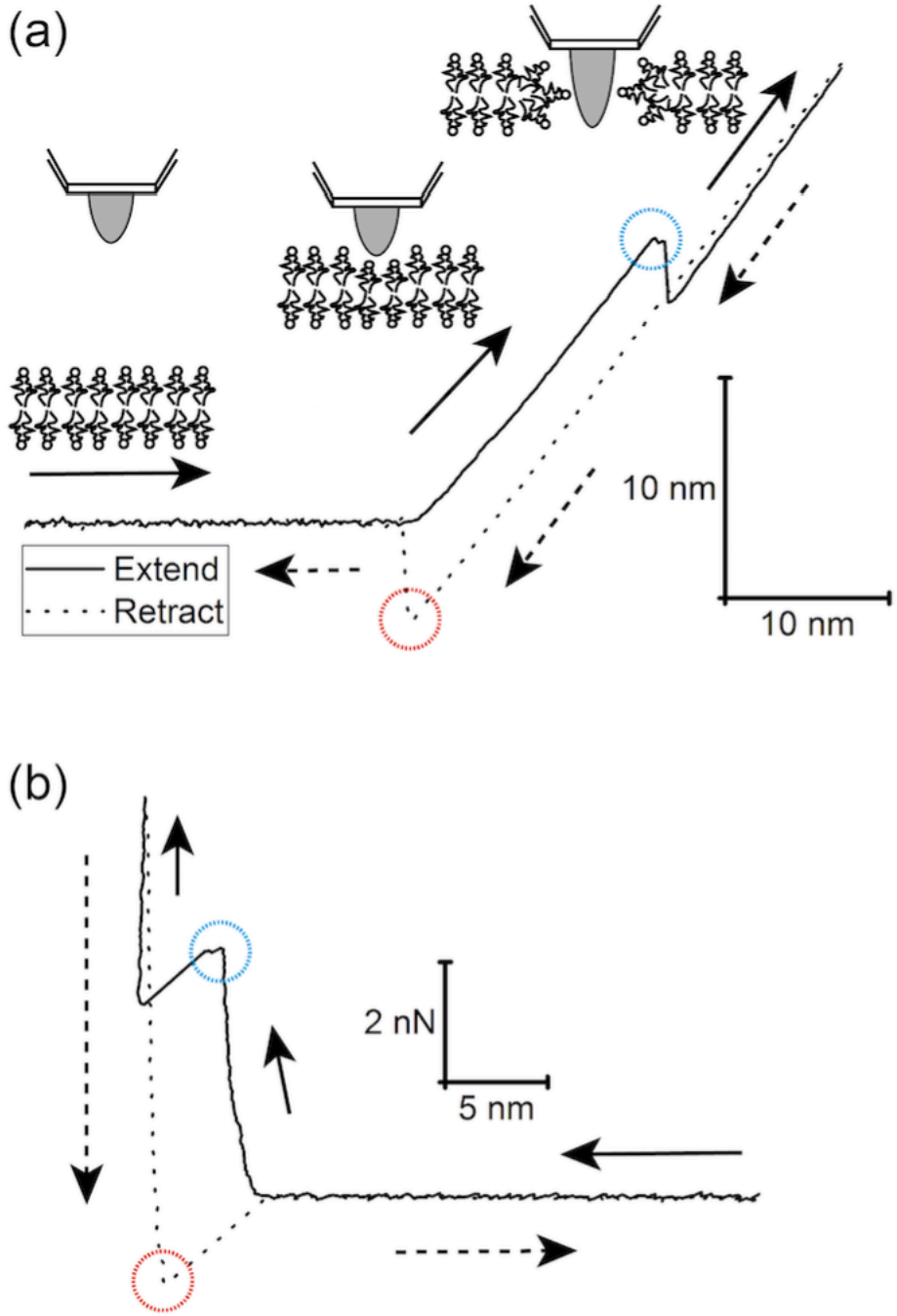

Figure 2.2: Example force curves recorded between an AFM tip and a supported lipid bilayer. Figure (a) show the raw data recorded and plotted at displacement in z against the deflection of the cantivlever, where the sample is driven towards and away from the probe by the piezoelectric scanner, shown in the x axis, whilst the deflection of the cantilever as recorded by the quadrant photodiode is shown in the y axis. Figure (b) shows the raw data converted to a applied force vs. tip-sample separation curve, from which the breakthough force (highlighted in blue), breakthough distance, and force of adhesion (highlighted in red) can be extracted.

The spring constant of the cantilever is specified by the manufacturer (Nanosensors), as simulated from the geometry of the cantilever that is constructed of monocrystalline silicon and is thus reported to represent a precise value, with a tolerance of ± 20 % of the true spring constant. The spring constant can be further measured by equating the resonance of the cantilever owing to thermal noise with that of a harmonic oscillator, at temperature T, given by:

$$\frac{1}{2}k_c\langle\Delta Z_c^2\rangle = \frac{1}{2}k_B T \Rightarrow k_c = \frac{k_B T}{\langle\Delta Z_c^2\rangle}$$

where the mean square of the cantilever defection, $\langle\Delta Z_c^2\rangle$, is obtained by integrating the noise power spectrum over the whole frequency range, which can be easily achieved in the propriety Nanoscope software. However, for the cantilevers used here (with a specified spring constant of 0.32 N/m), this thermal tuning method was not found to be reproducible, possibly owing to a damping of the relatively short, resonating cantilevers in liquid to give a signal beneath the detection limit. As a result, specified values of the spring constant were used, thus yielding absolute values of force and separation but with a finite accuracy determined by the manufacturers specifications. Force curves were recorded at distinct points across the surface, upon a pitch separated by ca. 100 nm intervals. Across all measurements, approach and retract rates were kept consistent at 1 μm s^{-1}

2.3.1.6 Image analysis

Images were processed using a variety of software dependent upon analysis in question, including Bruker Nanoscope Analysis (general image processing and extraction of force data), Gwiddion (extracting FFT's from repeating surface features), ImageJ (particle/contour analysis of domain) and WsXM[83] (general image processing). Briefly, images were plane leveled to remove and then flattened using a second or third order polynomial to remove tilt and bow from the image. Height data was extracted both by taking cross-sections through specified regions of the image, or by extracting a depth histogram which bins the z coordinate for each pixel in the image. Extracted data was further processed using OriginLab prior to presentation in this thesis.

2.3.2 Small-angle x-ray scattering

By studying the small-angle region of elastically scattered X-rays from regions of high electron density within a lyotropic sample, the mesoscopic ordering of the liquid crystalline sample can be probed. The repeating lattices within the lyotropic phase (e.g. the stacked lipid bilayers of the lamellar phase or close packing of micelles arising in inverse lipid phases) give rise to Bragg reflections that meet the condition:

$$n\lambda = 2d_{hkl}\sin\theta$$

where n is the order of the reflection, λ is the wavelength of the incident X-ray beam, d_{hkl} is the spacing between Miller planes denoted with integers h, k and l and θ is the angle between the incident and scattered (diffracted) beams. As a result, for a given wavelength of light, smaller angles are required to probe larger repeating structures, and thus requires a long path (i.e. flight tube) between the sample and detector in order to resolve such small-angle reflections. As the lyotropic samples are not aligned and are formed of many randomly oriented domains, the resulting (powder) diffraction patterns are comprised of series of concentric rings at distinct values of s. Characterization of a lyotropic liquid crystal by SAXS is achieved by first assigning the symmetry of phase, whereby the long range order in one, two or three dimensions gives rise to Bragg reflections with reciprocal spacing ($s_{hkl} = 1/d_{hkl}$) that are present in characteristic ratios, as shown in *table 2.1* below. By assigning the symmetry of the phase, the lattice parameter, a, can be extracted[32].

Phase	Equation	Peak position ratio	Miller indices (*hkl*)
Lamellar	$s_h = \frac{h}{a}$	1, 2, 3, 4, 5, …	(100), (200), (300), (400), (500), …
Micellar	-	Diffuse peak corresponding to size of micelles	-
Micellar cubic	$s_{hkl} = \frac{\sqrt{h^2+k^2+l^2}}{a}$	F_d3_m: $\sqrt{3}, \sqrt{8}, \sqrt{11}, \sqrt{12}, \sqrt{16}, ...$	(111), (220), (311), (222), (400), …
Bicontinuous cubic	$s_{hkl} = \frac{\sqrt{h^2+k^2+l^2}}{a}$	I_m3_m: $\sqrt{2}, \sqrt{4}, \sqrt{6}, \sqrt{8}, \sqrt{10}, ...$	(110), (200), (211), (220), (310), …
		P_n3_m: $\sqrt{2}, \sqrt{3}, \sqrt{4}, \sqrt{6}, \sqrt{8}, ...$	(110), (111), (200), (211), (220), …
		I_a3_d: $\sqrt{6}, \sqrt{8}, \sqrt{14}, \sqrt{16}, \sqrt{20}, ...$	(211), (220), (321), (400), (420), …
Hexagonal	$s_{hkl} = \frac{2\sqrt{h^2+k^2+hk}}{\sqrt{3}a}$	$\sqrt{1}, \sqrt{3}, \sqrt{4}, \sqrt{7}, \sqrt{9}, ...$	(100), (110), (200), (210), (300), …

Table 2.1: The reciprocal spacings of common lyotropic phases.

All SAXS measurements presented here were recorded using external synchrotron radiation sources, both at Diamond Light Source (Harwell, UK) and the European Synchrotron radiation facility (Grenoble, France), on their soft matter SAXS beamlines I22 and ID02 respectively. The energy of the X-rays was generally around 18 keV, with a corresponding wavelength of 0.689 angstroms. The distance between the sample and detector varied between 1.2 and 6 m, dependent upon the scheduled experiment; shorter flight tubes allowed for the wide-angle region to simultaneously be detected (giving an insight into the packing of hydrocarbon chains with repeat distances of ca. 4 Å), whilst longer flight tubes allowed for the characterization of structures with repeat distances on the order of tens of nm. Both beamlines were equipped with a high-pressure SAXS cell[84], allowing for sample environments at hydrostatic pressures of up to ca. 3000 kbar; although not the focus of the experiments presented in this thesis, the application of high pressure allowed for fast equilibration times when cycling the sample across a phase boundary in order to obtain homogenous samples.

2.3.3 Differential scanning calorimetry

Differential scanning calorimetry was performed using a Perkin-Elmer Diamond DSC, in the which the sample was heat cycled against a blank DSC pan, where the difference in power required to heat the sample against the blank reference was recorded (and

previously calibrated against an indium standard). Briefly, lipid samples were weighed directly into the DSC pans (to a weight of < 25 mg), hydrated to 70 wt. % water and sealed. The resulting sample pans were heat cycled from 5-95 ºC within in the DSC ca. 5 times until the traces shows a cooperative transition indicative of a homogenous sample. The heating traces presented were recorded after this process of homogenization, with cooling scans showing the inverse heat flow relating to phase transition, albeit with some hysteresis. Heating and cooling rates ranged between 5 and 15 °C min^{-1}, dependent upon the magnitude of the signal arising from the sample, with faster heating rates gives rise to sharper transitions that are more easily identified at the expense of an accurate measurement. At slower heating/cooling rates, phase transitions are allowed to occur before the temperature of the DSC chamber has crossed the temperature of the phase boundary, and are therefore more accurate where the transition temperature is taken as the onset on the peak in heat flow. However, such slower heating/cooling rates act to broaden the transition, and may not yield sufficient signal for transitions with a small enthalpy.

Chapter 3: Hydrophobic mismatch in phase-separated lipid bilayers

The lipid raft hypothesis has gradually built on the historic '*fluid mosaic*' model of the cell membrane first proposed by Singer and Nicholson in 1972[1], in which the lipid bilayer membrane was first identified as a two-dimensional matrix in which functional protein molecules could diffuse. As biophysical evidence has accumulated, it is now widely recognized that within model membrane systems (derived from both cell membrane extracts and minimal synthetic lipid mixtures) liquid-liquid phase separation occurs within the plane of the lipid bilayer to give microdomains that have been observed to span length scales from nm to μm's[6]. Notably, the presence of cholesterol induces the formation of the liquid-ordered (L_O) phase in sphingolipids and phospholipids that display a high degree of saturation in their respective hydrocarbon chains[9,50]. It has therefore been postulated that 'lipid rafts' can be thought of as *psuedo* liquid-ordered (L_O) domains that exist within the liquid-disordered (L_D) matrix, that is composed predominantly of phospholipids displaying a significant degree of unsaturation. As a result, it is hypothesized that such phase-separation within the cell membrane has a functional role in vivo, through which compartmentalization can occur by recruiting biomolecules with an affinity for the cholesterol-rich domains, thus focusing their bioactivity[5], as depicted in the schematic shown in *figure 3.1*. However, verification of lipid rafts *in vivo* has not been satisfactorily achieved owing to the nm length scales that they are proposed to occupy, below the diffraction limit and thus unobservable by traditional light microscopy. In addition, their temporal evolution has not been characterized such that it can be known if they exist on timescales that are relevant to biological function[85]. Finally, control over the size and morphology of such microdomains, which exist out of equilibrium, is not understood[7,13].

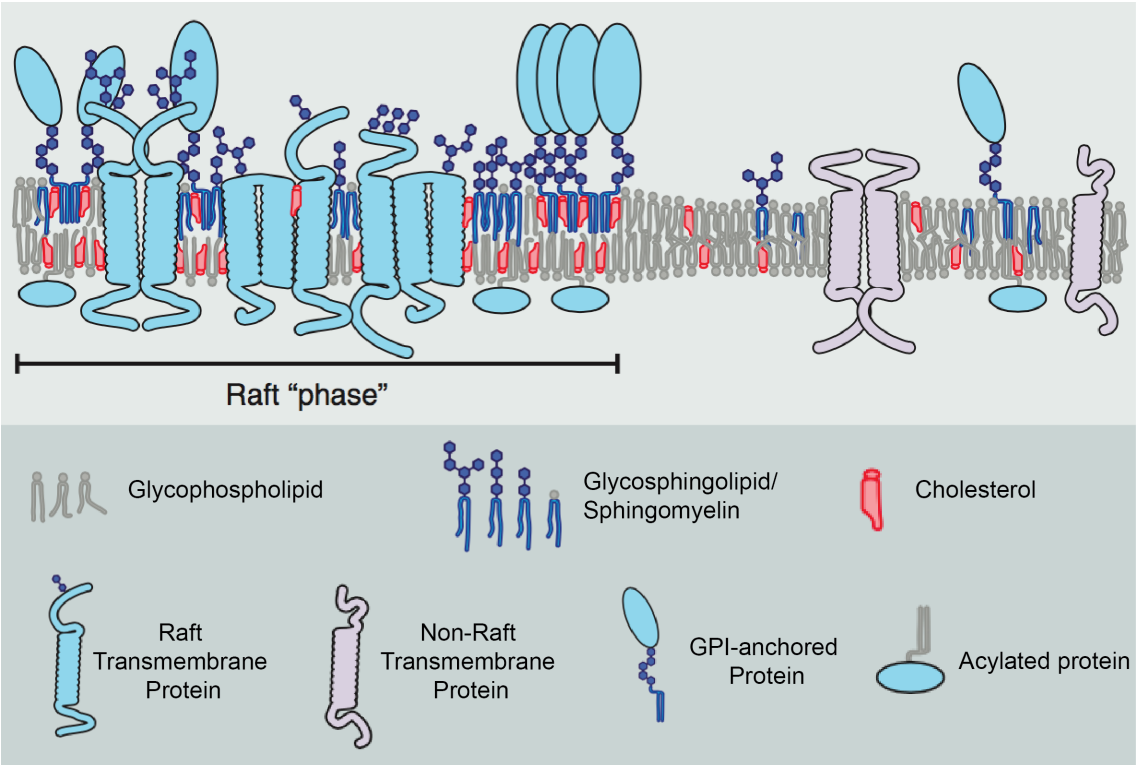

Figure 3.1: Schematic depicting the lipid rafts that are postulated to result in lateral compartmentalization within the live cell membrane. The 'raft' phase is rich in cholesterol and sphingolipids, selectively incorporating raft-associating transmembrane and GPI anchored proteins. *Figure taken from*: Lingwood, D. & Simons, K. Lipid rafts as a membrane-organizing principle. Science **327**, 46–50 (2010).

The liquid ordered phase has received much attention both in its interesting physical properties that make up such an ordered two-dimensional fluid, and in its possible implications for the plasma membrane *in vivo*[86,87]. This *ordered* state can be thought of as possessing relative order in the orientation of the lipid hydrocarbon chains, with disorder in the lateral plane of the lipid bilayer; that is, it exists as a 2D fluid whereby lateral diffusion can occur on the order of 10 $\mu m^2/s$[88]. The order within the hydrocarbon chain region is imposed by cholesterol, a lipid molecule that is abundant in eukaryotic cells, typically reaching concentrations of 30 molar %. Cholesterol is an atypical lipid in that the 'chain' region is comprised of a rigid sterol ring that acts to disrupt the tightly packed *gel*-phase whilst ordering the liquid-*disordered* phase[89]. The liquid ordered phase can be further characterized as giving rise to a broad WAXS peak at 4.2 Å, as possessing acyl chains that are all in the *trans* state, and gives rise to ^2H quadrupolar NMR splitting

at 50 kHz[87]. In coexistence with the liquid disordered phase, a characteristic boundary region with a convex or concave profile is observed that is distinctive to liquid-liquid coexistence.

A possible means of spatial regulation of lipid rafts is via the hydrophobic mismatch that exists at the domain boundary between a liquid-ordered 'lipid-raft' and its liquid-disordered lipid matrix[90,91], which has an associated line tension, that depends quadratically on height mismatch[92], and in turn governs the size and morphology of the resulting domains[93]. This line tension arises when the difference in height between the two domains, as determined by the hydrocarbon chain length of the respective lipid moieties, exposes a hydrophobic domain edge to the lipid-water interface and can be defined as the energy per unit length of this interface, which thus manifests itself as force whose vector acts perpendicular to this interface. The formation of such a hydrophobic domain edge is unfavorable, with the exposed area scaling with the mismatch between the respective lipid chain lengths, and has an associated energetic cost. In order to offset this cost, the membrane domains hypothetically distort to favor morphologies that minimize the length at the domain edge, whereby the line tension can similarly be defined as the force acting to 'pull' the domain inwards[94]. Furthermore, it has been suggested that hybrid lipids that possess both saturated and unsaturated hydrocarbon chains, such as POPC, can act an 'linactants' (i.e. a 2D analogue of a *surfactant*) whereby both saturated and unsaturated hydrocarbon chains are present, and thus stabilize the domain edge by favourably interacting with the respective coexisting phases simultaneously[95,96].

An interesting problem can be observed in the propensity of the respective leaflets of a phase-separated bilayer to 'register'[97]; that is, to line up so L^O regions oppose L^O whilst L^D opposes L^D. A possible means of minimizing the hydrophobic mismatch would be for *anti*-registration to occur, although this is rarely observed experimentally. This interplay between the hydrophobic (height) mismatch and registration/anti-registration has been the subject of recent theoretical studies and molecular modelling studies[97-99], where the following conclusions relevant to this work were reached[97]: (i) The formation of domains occurs via a two-step process locally asymmetric, anti-registered domains are initially

formed before reaching their registered, equilibrium state. (ii) An estimated crossover length of 20 nm is proposed, where anti-registered domains are favoured at smaller length scales (n.b.- this is likely inherently coupled to the magnitude of height mismatch). (iii) Increasing the height mismatch increases the purity of the resulting phases, owing to an increase in the immiscibility of the lipids on a microscopic scale. From such observations it can be seen how intricately linked the height mistmatch is to both lateral phase separation and transbilayer organization.

Biophysical studies have shown that such hydrophobic mismatch has a direct impact upon the sorting of membrane proteins, notably in the case of the SNARE family that mediate membrane fusion[100]. The effect of height mismatch on domain morphology can be systematically probed by studying 3-component model membrane systems (in this case saturated-PC:Chol:DPhPC) that phase separate to give liquid-liquid coexistence; by varying the hydrocarbon chain of one of the respective phospholipid entities, the effect of hydrophobic mismatch can be deduced and an estimate of the value of line tension can be assigned provided that the average thickness of the lipid bilayer is known. A combination of AFM topographic imaging[10] and force spectroscopy[77] has the capability to measure both height mismatch and bilayer thickness without the requirement for further experimental techniques.

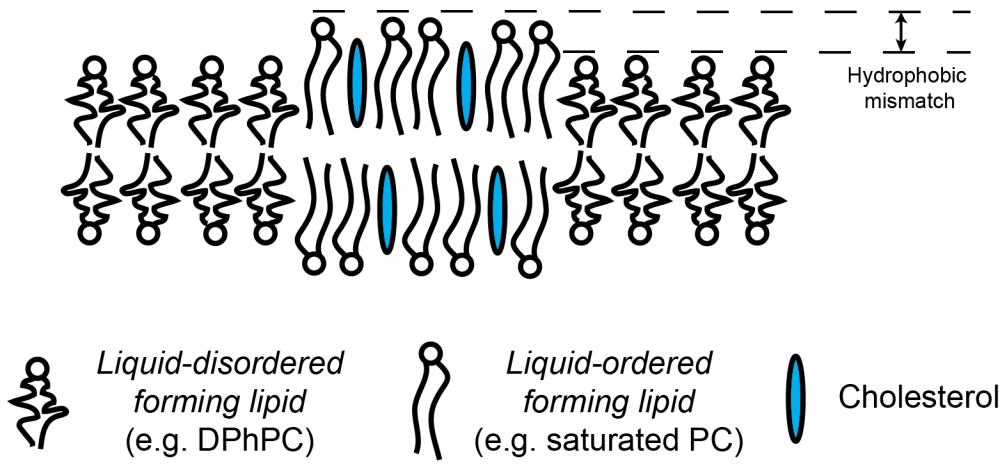

Figure 3.2: Schematic of the cross-section through a model membrane showing liquid-liquid coexistence. At the domain edge, there is a mismatch in the height between the two domains that gives rise to an associated line tension.

The work presented in this chapter applies established AFM methodologies to phase-separated supported lipid bilayer membranes, thus providing a means of demonstrating our ability to apply AFM in the study of model membranes *in-house* in the absence of fine and variable control over intensive thermodynamic properties (as in this case all AFM experiments are performed at room temperature). It is demonstrated that interesting insights into how hydrophobic mismatch at the domain boundary affects domain morphology can be gained, with quantification of the hydrophobic mismatch and domain circularity, and a derived estimate of their associated line tension. In addition, it was observed that higher degrees of hydrophobic mismatch give rise to less stable domains with a propensity for rapid coalescence and domain ripening. Variations in the temperature of the model systems would represent a more comprehensive study, and with complimentary techniques (SAXS and DSC), the 'demixing' temperature (i.e. the point at which the respective liquid domains become miscible) can be identified; previous studies have shown that the demixing temperature has a strong dependence upon domain height mismatch[94], whilst most recent reports have argued that this relationship varies with the lipid ratios within the three-component system[101]. In addition, an understanding of domain formation and dissolution with temperature paves the way for further work at the most revealing region of the given systems phase diagram[10].

3.1 AFM of saturated-PC:Chol:DPhPC mixtures

Methods of studying phase separation within model membrane systems have developed from their initial observation as inferred from detergent resistant regions of the native cell membrane, to super-resolution nanoscopy of live cell membranes[8]. Atomic force microscopy provides an ideally-suited tool in the study of *model* lipid rafts (*n.b*. AFM of live cell membranes only allows for low resolution imaging owing to the flex intrinsic to the unsupported native cell membranes), with the height mismatch between L_O and L_D domains providing contrast that can be detected with vertical ångström resolution at lateral length scales from nm to μm. In addition, AFM can give an insight into the mechanical properties of the model membrane *via* force spectroscopy, in which the force

required to break though the supported lipid bilayer can be measured and mapped at distinct points across the surface; this methodology also provides an indirect method of measuring bilayer thickness. A comprehensive view of a model membrane can therefore be constructed using solely AFM, in which it is possible to visualize domain size and morphology whilst simultaneously measuring domain height mismatch and bilayer thickness.

The model membranes used in this study consist of three-component lipid mixtures of saturated-PC:DPhPC:Chol, with systematic variation in the saturated-PCs hydrocarbon chain length, for which chemical structures shown in *figure 3.3*. Phase separation occurs between liquid-ordered (L_O) domains rich in saturated-PC and cholesterol, and the liquid-disordered (L_D) lipid matrix rich in DPhPC, allowing for height mismatch to be measured at the domain boundary. Systematic variation in the length of the saturated hydrocarbon chain (from DLPC (C_{12}) through to DAPC (C_{20})) allows for differentiation in the observed height mismatch, whilst DPhPC is a synthetic lipid in which the substituent methyl groups act to disrupt the packing of the hydrocarbon chains in a manner analogous to an unsaturated C-C double bond, thus forming the liquid-disordered (L_D) matrix without risk of oxidation. DPhPC was chosen here owing to it's robust physicochemical properties in order to minimize the risk of discrepancies between datasets, as these experiments were performed in parallel with both fluorescence microscopy and SAXS using equivalent model membranes systems conducted by Nicola McCarthy *et al*. In addition, the very low melting point of DPhPC allows for simple differentiation between the lipids in the L_O and L_D phases respectively, even in the presence of saturated lipid with low melting temperatures (i.e. DLPC). This three-component lipid bilayer represents a different system to that studied by Schwille[94], in which height mismatch was controlled by varying the length of the unsaturated lipid, with sphingomyelin comprising the L_O phase. As the L_D region is more likely to adapt it's thickness, a mixture in which the L_D forming lipid is kept constant should represent a more robust system for studying the effect of height mismatch.

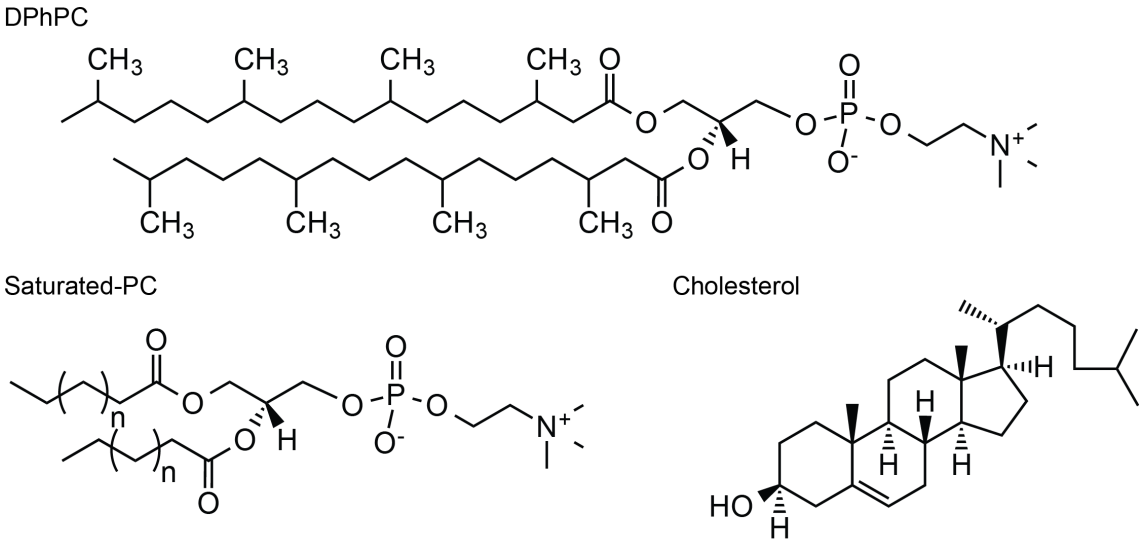

Figure 3.3: Chemical structures of the lipids used in the 3-component mixtures. DPhPC (1,2-diphytanoyl-*sn*-glycero-3-phosphocholine) is a synthetic analogue of naturally occurring, unsaturated $\boldsymbol{L_D}$ forming lipids, with the methyl substituents disrupting the packing of the hydrocarbon chains; it is however more robust for use in model systems owing the the absence of any unsaturated *C-C* bonds.

The saturated-PC lipid maintains the same phosphocholine headgroup across the mixtures studied, but with a systematic increase of 2 carbon atoms per hydrocarbon chain, as shown in *table 3.1* below. The associated increase in the main phase transition temperature of the saturated-PC upon increasing chain length gives an insight into how that given lipid will behave in a 3-component mixture with DPhPC and cholesterol, with DLPC likely miscible with DPhPC at room temperature as both lipid species adopt the liquid disordered phase at temperatures below freezing (-2 and <5 °C respectively; no detectable phase transition for DPhPC between -120 and +120 °C, as reported by Avanti Polar Lipids)[102]. Increasing the hydrocarbon chain length for saturated-PC leads to an associated increase in the main phase transition temperature, owing to the increased van der Waals interactions between hydrocarbon chains. It is expected that the presence of cholesterol within the three-component mixtures will preferentially reside in regions rich in saturated-PC, disrupting the packing of the hydrocarbon chains and allowing the formation of the liquid-ordered (L_O) phase.

Lipid		No. of carbon atoms in hydrocarbon chain	Main transition temperature (°C)
DLPC	1,2-dilauroyl-*sn*-glycero-3-phosphocholine	12	-2
DMPC	1,2-dimyristoyl-*sn*-glycero-3-phosphocholine	14	24
DPPC	1,2-dipalmitoyl-*sn*-glycero-3-phosphocholine	16	41
DSPC	1,2-distearoyl-*sn*-glycero-3-phosphocholine	18	55
DAPC	1,2-diarachidoyl-*sn*-glycero-3-phosphocholine	20	66

Table 3.1: Table showing the saturated-PC lipids using in this study along with the number of carbon atoms in their respective hydrocarbon chains and the main phase transition temperatures. Chemical data as reported by the supplier, Avanti Polar Lipids (Alabaster, Alabama USA).

The relative ratios of saturated-PC:DPhPC:Chol must be considered for that given mixture to exhibit liquid-liquid phase separation. As DPhPC and the saturated-PC lipids (disregarding DLPC) reside in distinct lyotropic phases (fluid and gel respectively when hydrated and at room temperature), their binary equimolar mixtures will exhibit phase separation, and it is therefore the concentration of the cholesterol dopant that must be tuned to form a two-phase, L_O-L_D system. Fluorescence microscopy of equivalent giant unilamellar vesicles (GUVs) have reported liquid-liquid phase-separation for 1:1:1 and 2:2:1 molar ratios[9], and have therefore been adopted here. As the focus of this work is to measure the height mismatch between domains, with subsequent derivation of the associated line tension, the domain morphology is not directly relevant but will be discussed. The AFM images presented in this section (*3.1*) provide a qualitative overview of how height mismatch affects line tension; values of height mismatch, domain circularity and the derived line tension extracted from these images are presented in *section 3.3*.

3.1.1 Saturated-PC:DPhPC:Chol (2:2:1 mol %)

AFM images of supported bilayers containing 2:2:1 saturated-PC:DPhPC:Chol reveal phase separation with an associated height mismatch between the distinct phases that increases by ca. 0.5 nm for each additional -CH_2CH_2- group (as shown in *figure 3.4*). Isolated domains with a matrix of the supporting lipid rich in DPhPC, at a lower relative height, are characteristic of formation *via* nucleation and growth (cf. spinodal decomposition, which results in an interconnected bicontinuous network)[9]. It is therefore possible to quantify their 'circularity'; how far the domains deviate from being perfectly circular, where line tension drives circularity. It is likely that for mixtures with a lower relative cholesterol content than 1:1:1, cholesterol is more strongly partitioned between the two domains occupied by each respective lipid, predominantly residing in the saturated-PC rich region.

For the system with the shortest saturated hydrocarbon chain (DLPC, C_{12}), no phase separation was observed to occur under the conditions studied as evidenced in the tapping-mode AFM images in figure 3.4. As predicted, the low main transition temperature (-2 °C) of DLPC allows for the complete miscibility with DPhPC, with the resulting supported lipid bilayer indistinguishable from the underlying mica substrate by AFM imaging alone. Increasing the length of the hydrocarbon chain by 2 carbon atoms (which correspondingly acts to increase the main transition temperature of the individual lipid; see table 3.1), results in sub-micron sized domains that adopt their most circular morphology for the intermediate hydrocarbon chain lengths of DPPC and DSPC (C_{16} and C_{18} respectively). At longer hydrocarbon chain lengths (DAPC; C_{20}), a height mismatch of ca. 2 nm is observed, whereby the higher region, rich in DAPC, dominates and forms an interconnected network, plausibly *via* the rapid coalescence of smaller domains (unobservable by the AFM used here). In addition, fractures run through the DAPC-rich regions, suggesting the presence of the gel (L_β) phase. The gel phase, with a marked increase in the ordering of hydrocarbon chains with an associated loss in diffusion within the plane of the membrane, as compared with liquid (lamellar) phases, is favored on increasing hydrocarbon chain length. To corroborate the presence of the gel phase in a supported lipid bilayer, additional techniques are required that have not

been applied; fluorescence recovery after photobleaching (FRAP) can differentiate between liquid and gel regions of supported lipid bilayers with measurements of their diffusion coefficients[103].

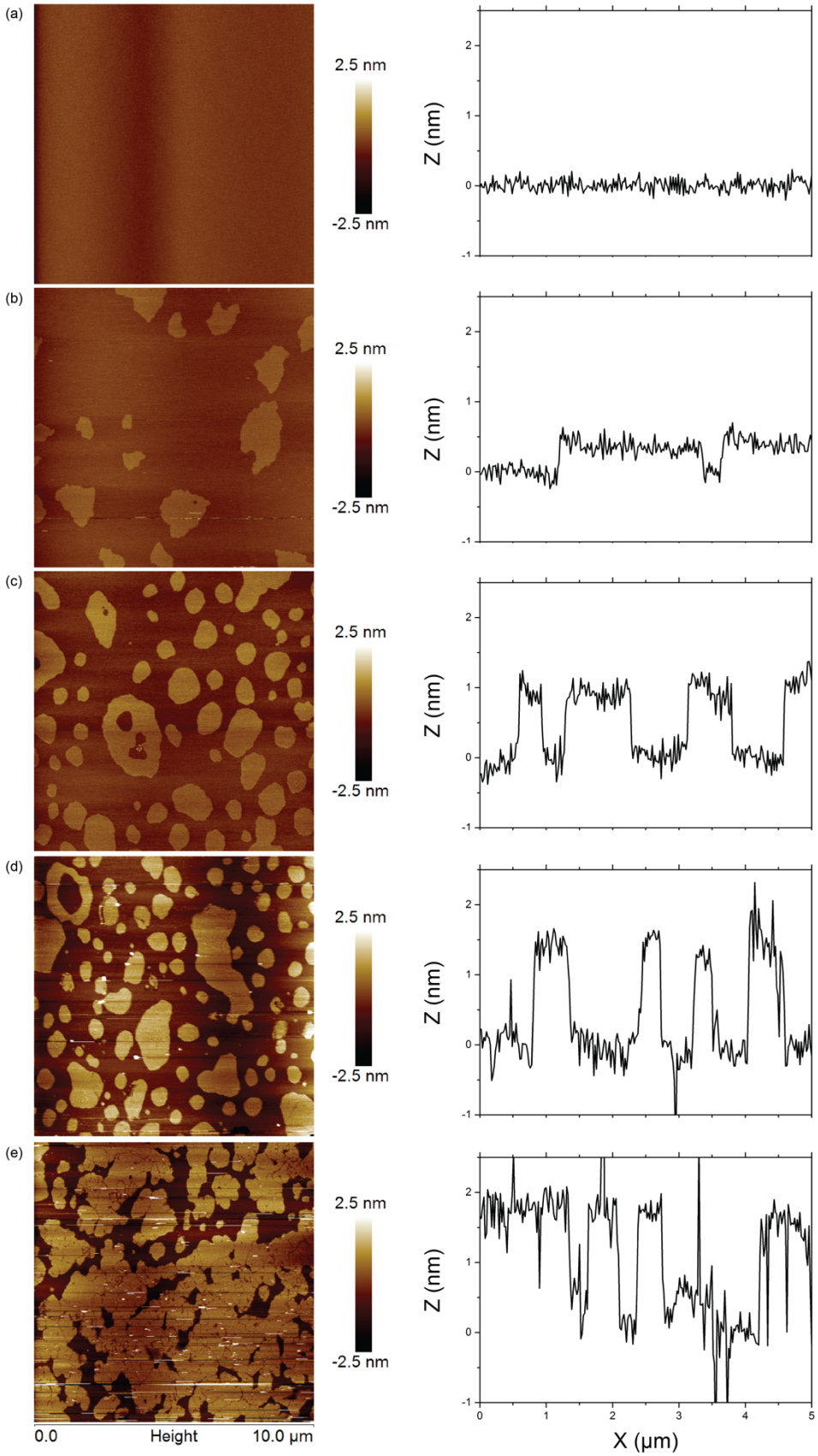

Figure 3.4: Tapping mode AFM and corresponding cross sections for 2:2:1 mixtures of saturated-PC:DPhPC:Chol, where saturated-PC is (a) DLPC (C_{12}) , (b) DMPC (C_{14}), (c) DPPC (C_{16}), (d) DSPC (C_{18}) and (e) DAPC (C_{20}).

3.1.2 Saturated-PC:DPhPC:Chol (1:1:1)

At ratios of 1:1:1 saturated-PC:DPhPC:Chol, there is a relative decrease in the height mismatch for each respective system, as compared with their equivalent 2:2:1 mixtures, but the overall trend in increasing height mismatch on increasing the length of the hydrocarbon chain for saturated-PC remains the same. Here, each -CH_2CH_2- group in the saturated-PC's hydrocarbon chain corresponds to a ca. 0.25 nm increase in height mismatch (as show in *figure 3.5*), with the consistent formation of domains that persist with a lesser degree of coalescence and ripening over similar time scales to those studied for the 2:2:1 systems discussed previously (see *figure 3.4*), suggesting that more stable liquid-ordered (L_O) domains are formed. The higher relative amount of cholesterol favors the formation of the L_O phase, most evident in the images of DAPC (C_{20}) containing mixtures, whereby distinct circular domains can be seen which were not observed for equivalent 2:2:1 mixtures (*figure 3.5 (d)*). 1:1:1 mixtures containing DMPC (C_{14}) show clear phase separation with a height mismatch of ca. 0.25 nm, albeit with jagged domains edges that are generally associated with the gel phase; the possibility arises that at shorter hydrocarbon chain lengths, cholesterol cannot be accommodated. Alternatively, the mixture may be close to a critical point, giving rising to an unstable morphology in which the domain edge deviates from the circular shape that is characteristic of a liquid phase. It is interesting to note that for DPPC (C_{16}), there is an inversion in the dominant phase, with the higher liquid-ordered regions forming the lipid matrix that surrounds liquid-disordered domains rich in DPhPC, showing cholesterol to strongly and preferentially partition into the area rich in DPPC. For the longer chain lengths of DSPC (C_{18}) and DAPC (C_{20}), 1:1:1 mixtures gave rise to more circular domains, thus indicating liquid-liquid coexistence.

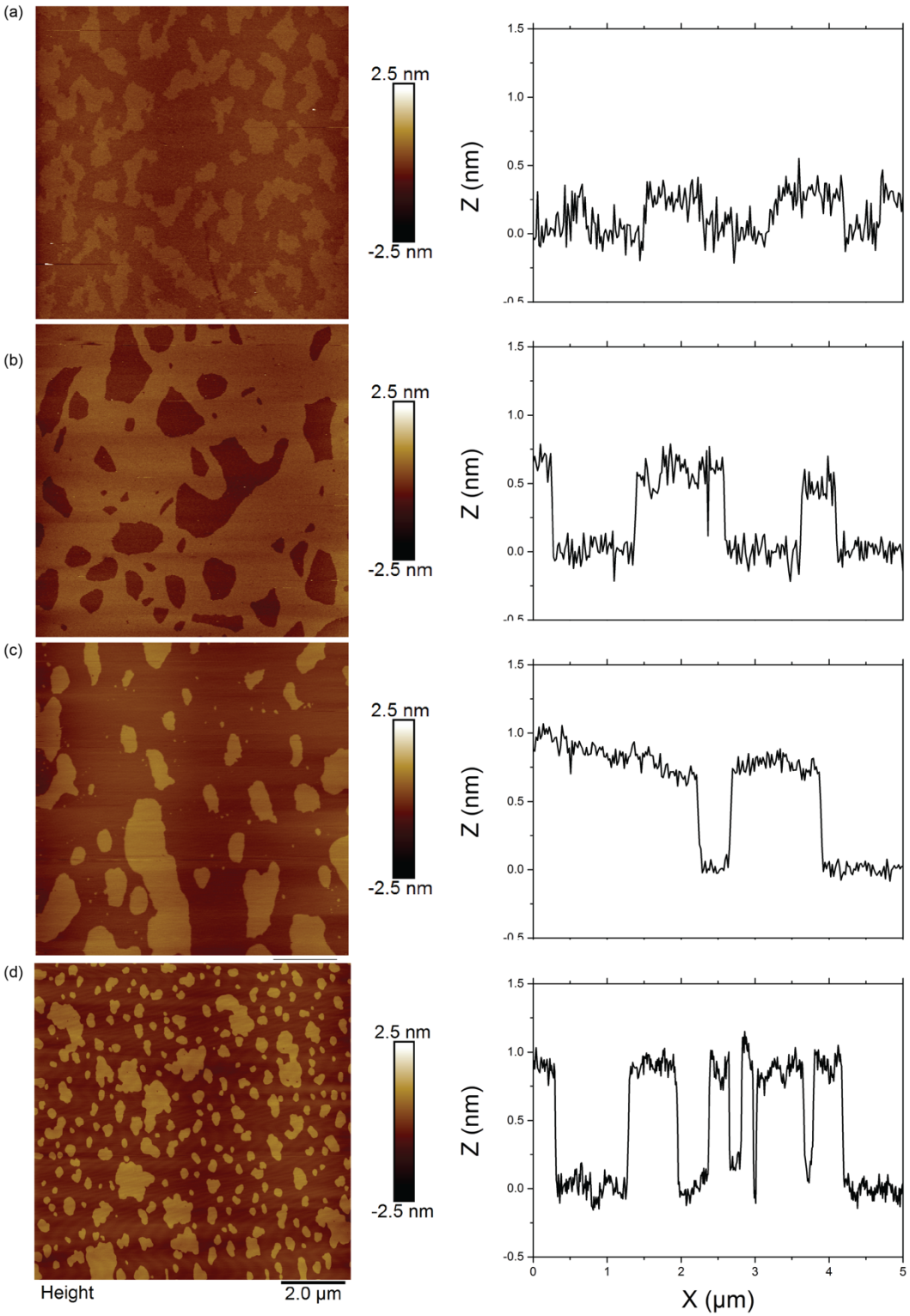

Figure 3.5: AFM images and corresponding cross-sections of 1:1:1 mixtures of saturated-PC:DPhPC:Chol, where saturated-PC is (a) DMPC (C_{14}), (b) DPPC (C_{16}), (c) DSPC (C_{18}) (d) DAPC (C_{20}).

3.1.3 Domain ripening for systems containing longer saturated hydrocarbon chains (DSPC and DAPC)

Time-lapse AFM imaging, with a frame rate on the order of minutes using the standard AFM methodologies available *in-house*, reveals how domains coalesce and 'ripen' over time (at constant temperature). Notably, for the systems studied here it was observed that with lipids containing longer hydrocarbon chains (i.e. DAPC) domain ripening was observed for both 1:1:1 and 2:2:1 mixtures (as shown in *figure 3.6*). Significant deviations from the circular domains characteristic of liquid-liquid coexistence emerge, with domain ripening progressing faster at lower relative concentrations of cholesterol (i.e. for 2:2:1 mixtures), where there is a greater propensity for the formation of the gel (L_β) phase.

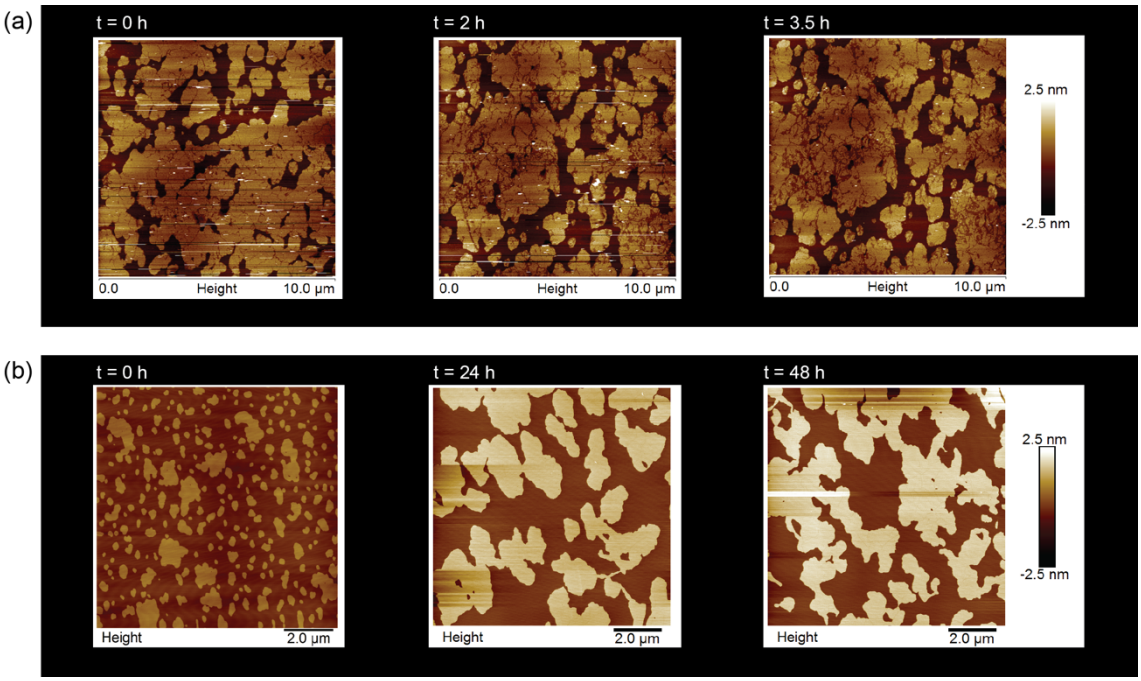

Figure 3.6: Time-lapse AFM of (a) DAPC:DPhPC:Chol (2:2:1) over a period of 3.5 hours and (b) DAPC:DPhPC:Chol (1:1:1) over a period of 48 hours. Ripening of the DAPC-rich regions can be observed, with the emergence of domain morphologies and fractures which suggest contribution from the gel ($\boldsymbol{L_\beta}$) phase. *N.B. – Sequence (a) represents imaging of the same membrane area over a period of 4 hours (intermediate images not shown), whereas sequence (b) represents distinct model membrane samples (of the same lipid composition) that were imaged 0, 24 and 48 hours after incubation above their* T_m.

At the longest time points for which images were recorded (3.5 and 48 hours for 2:2:1 and 1:1:1 mixtures respectively) fractures within the DAPC-rich regions can be observed, with the same fractured domains increasing in their height mismatch with the DPhPC-rich background with time. Such observations are indicative of dominant gel (L_β) phase, with the longer hydrocarbon chains of DAPC leading to the adoption of more crystalline packing. In addition, compositions of 2:2:1 DAPC:DPhPC:Chol ripen with the the emergence of an additional region with a distinct height in z (as an intermediate between the DAPC-rich and DPhPC-rich regions); the opens up the possibility of 3-phase coexistence, or a region that contains asymmetric packing of the respective monolayers that would give rise to a third distinct membrane thickness[104].

3.2 AFM force spectroscopy as a means of measuring bilayer thickness

In addition to the unprecedented imaging capabilities of AFM, the nanoscale tip can be utilized as a force probe, and as such is applied here in determining the force at which the model lipid bilayer ruptures as the AFM tip punctures through to the underlying substrate[105,106]. Importantly, the distance between this breakthrough event and the underlying substrate can be measured and taken as the bilayer thickness[107], as is required in deriving line tension at the domain boundary (as discussed below in *section 3.3*). As the membrane is placed under compression prior to rupture, thus potentially shortening the breakthrough distance relative to the width of the unconstrained bilayer, this value is not absolute but serves as a useful indicator whilst simultaneously shedding light on the nanomechanical properties of the bilayer (with values of breakthrough force). It must further be noted that it is not possible to measure absolute separation distances between the tip and the underlying substrate with AFM alone, as separation distances are inferred from the deflection of the cantilever and are not measured independently (cf. SFA, in which the distance between two opposing mica sheets is measured optically[108]). In quantifying the lipid bilayers nanomechanical properties, it it possible to derive values of line tension from the observed distribution in breakthrough force according to a continuum nucleation model outlined by Butt[105,106], but it is important to note that these values represent the line tension associated with the spontaneous formation of a hole in

the bilayer as induced under load by the AFM tip, and do not represent values of line tension at a domain boundary. This method is therefore not applied here, where values of line tension are the domain boundary are estimated from the measured height mismatch. However, the breakthrough force is revealing in distinguishing between areas of L_O and L_D, and serves as a useful measure of the yield strength of the bilayer.

An example of the force vs. distance data for model membranes composed of DMPC:DPhPC:Chol is shown in *figure 3.7*. On approach to the membrane surface, repulsion between the AFM probe and lipid bilayer headgroups can be observed as an increase in force. Once a certain threshold is reached (characteristic of the local membrane composition), the bilayer yields and the AFM probe breaks through to the underlying substrate; the corresponding 'breakthrough distance' quoted if therefor taken as the width of the bilayer under load. A secondary breakthrough event is observed before the AFM tip comes into hard contact with the mica surface; this corresponds to a hydration layer comprised of calcium ions (that are present during the formation of the supported bilayer) and associated water molecules, and is visible as the initial breakthough of the bilayer occurs at relatively low forces of < 10 nN, allowing for events occurring at higher applied forces to be observed. *Figure 3.7* shows two distinct (primary, i.e. discounting the hydration layer) breakthrough events that are proposed to correspond to DMPC-rich domains (i.e. liquid-ordered *with a higher breakthough force*) and DPhPC-rich liquid-disordered regions respectively. The model membrane surface can be mapped by recording force curves at distinct points across the surface, with the resulting dataset converging towards a value of breakthrough force(s) for that given system.

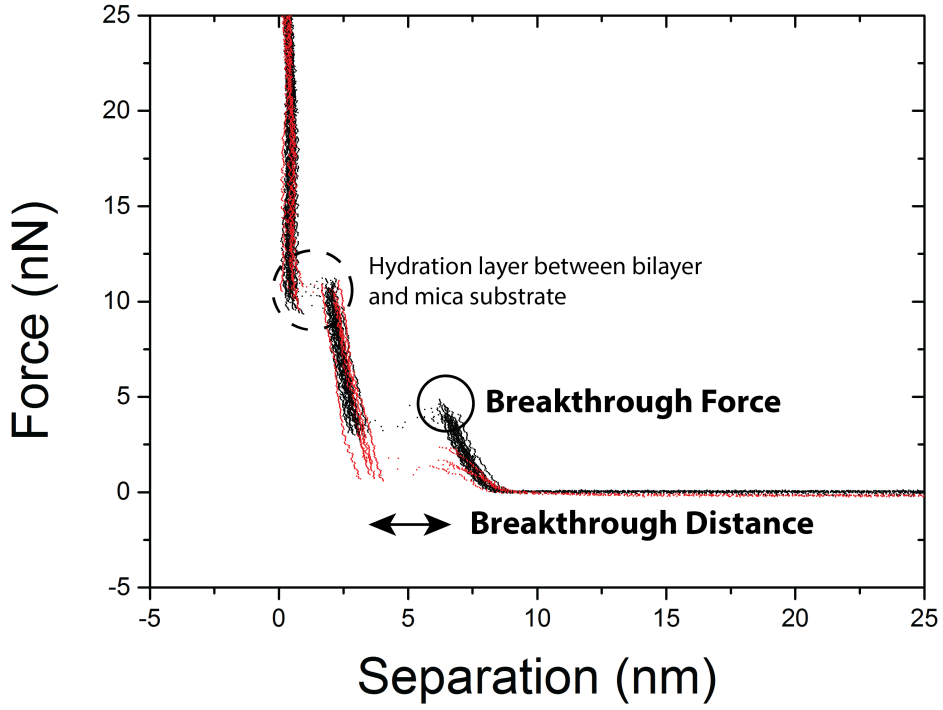

Figure 3.7: Example force vs. separation curves on approach of the AFM probe to the lipid bilayer surface (n = 22). The breakthrough force is taken as the initial maxima on approach to the surface, with a breakthrough distance that corresponds to the width of the lipid bilayer. The second jump-to-contact results from the hydration layer between the lipid bilayer and mica substrate. The black data points are proposed to correspond to rupture of DMPC-rich domains, with red data points corresponding to the DPhPC-rich lipid matrix.

Plotting the breakthrough force vs. breakthrough distance (as shown in *figure 3.8* for DMPC:DPhPC:Chol 1:1:1) highlights the distinct events that arises from a two-phase system. A primary distribution arises with a low breakthrough force of 2 nN with an associated breakthrough distance of 2.9 nm, thus correlating with the 'softer' DPhPC-rich, L_D regions. A secondary distribution containing events with higher breakthrough forces of 4 nN have a corresponding larger breakthrough distance of 3.5 nm, thus representing the stiffer DMPC-rich, L_O domains that are observed in the AFM image of the same system shown in *figure 3.5(a)*.

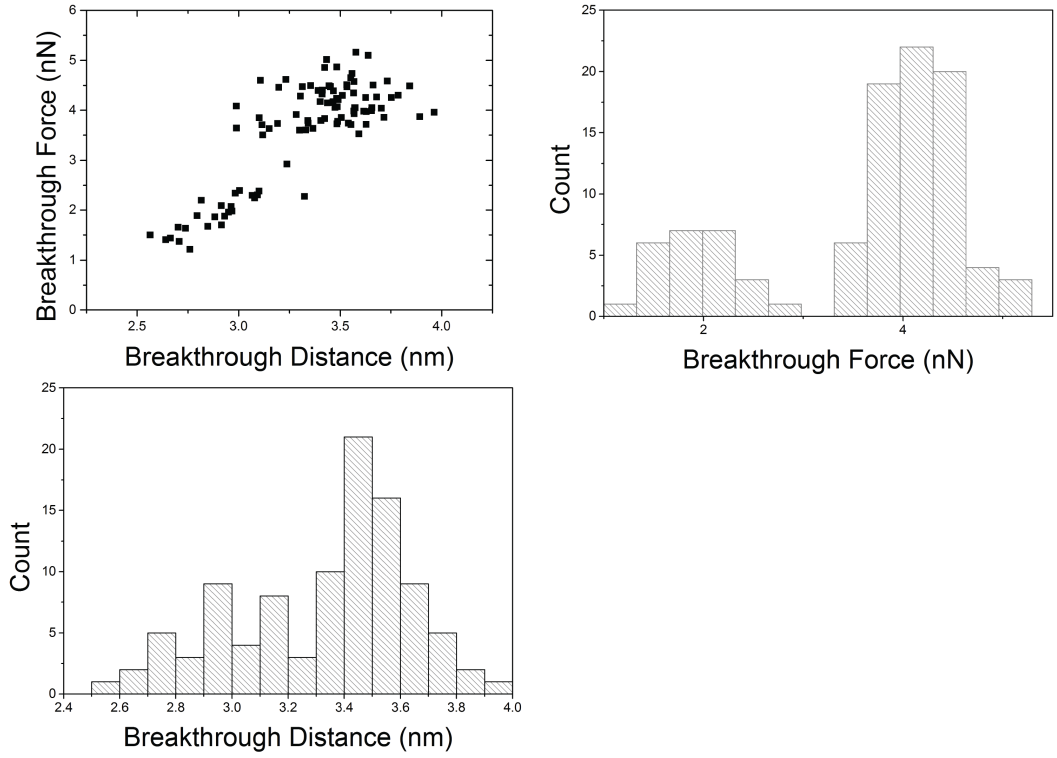

Figure 3.8: Breakthrough force vs. breakthrough distance and corresponding histograms for DMPC:DPhPC:Chol (1:1:1); n=100.

1:1:1 mixtures of DPPC:DPhPC:Chol display similar behavior in their breakthrough events to the equivalent DMPC system discussed previously, with two distinct distributions in breakthrough distance that converge at 3.1 and 3.7 nm respectively (as shown in *figure 3.9* below). However, values of breakthrough force are not so easily differentiated; all measured values lie within 1 nN with an average value of ca. 4 nN. As both DPPC and DPhPC contain C_{16} hydrocarbon chains, it is plausible that the bilayer is less (chemically) heterogeneous, with cholesterol more equally partitioned between the two regions, resulting in similar values of breakthrough force for the coexisting L_O and L_D phases.

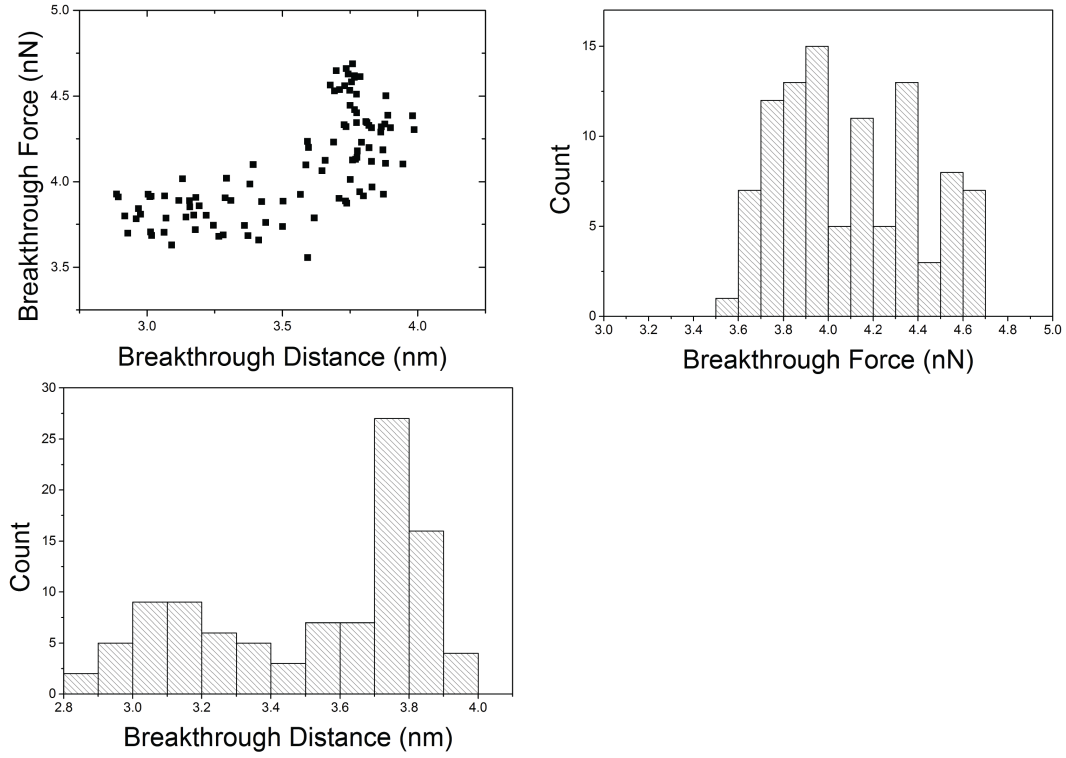

Figure 3.9: Breakthrough force vs. breakthrough distance for DPPC:DPhPC:Chol (1:1:1); n = 100.

N.B. - *Force data for systems containing DSPC was not obtained (force curves corresponding to the DSPC imaging data shown in figure 3.5 displayed significant artefacts which rendered their inclusion redundant).*

Force curves resulting from 1:1:1 mixtures of DAPC:DPhPC:Chol showed a significant increase in the measured breakthrough forces relative to the DMPC and DPPC systems discussed previously. Distinct breakthrough events can be observed at ca. 5 nN and 12 nN respectively, although the breakthrough distance is less well defined with a single population converging at a distance of ca. 3 nm (as shown in *figure 3.10*). The significantly longer hydrocarbon chain of DAPC (C_{20}) results in a greater degree of van der Waals attractions between the lipids with in the plane of the bilayer, thus rendering the bilayer less susceptible to deformation, with DAPC bilayers being able to withstand higher applied forces before breakthrough occurs. It's important to note that the breakthrough force is increased for both the DPhPC-rich and DAPC-rich regions, suggesting that the saturated lipid is somewhat dispersed throughout the entire bilayer, albeit with a strong preference to reside in the L_O region. The breadth of the distribution

of breakthrough force is also increased to range over 5 nN, with previous AFM imaging (shown in *figure 3.6*) revealing that domains containing DAPC have a propensity to fracture, suggesting a contribution from the gel (L_β) phase that could represent the highest breakthrough forces measured. The breakthrough distance shows little variation between the distinct regions even through there is a significant degree of height mismatch (as observed in the AFM images shown in *figure 3.5*). The higher applied forces required for rupture of the DAPC-rich region may lead to artefacts in the force curves that act to shorten the measured breakthrough distance; stiffer cantilevers and a variation in loading rate would thus give a more comprehensive measure of breakthrough distance.

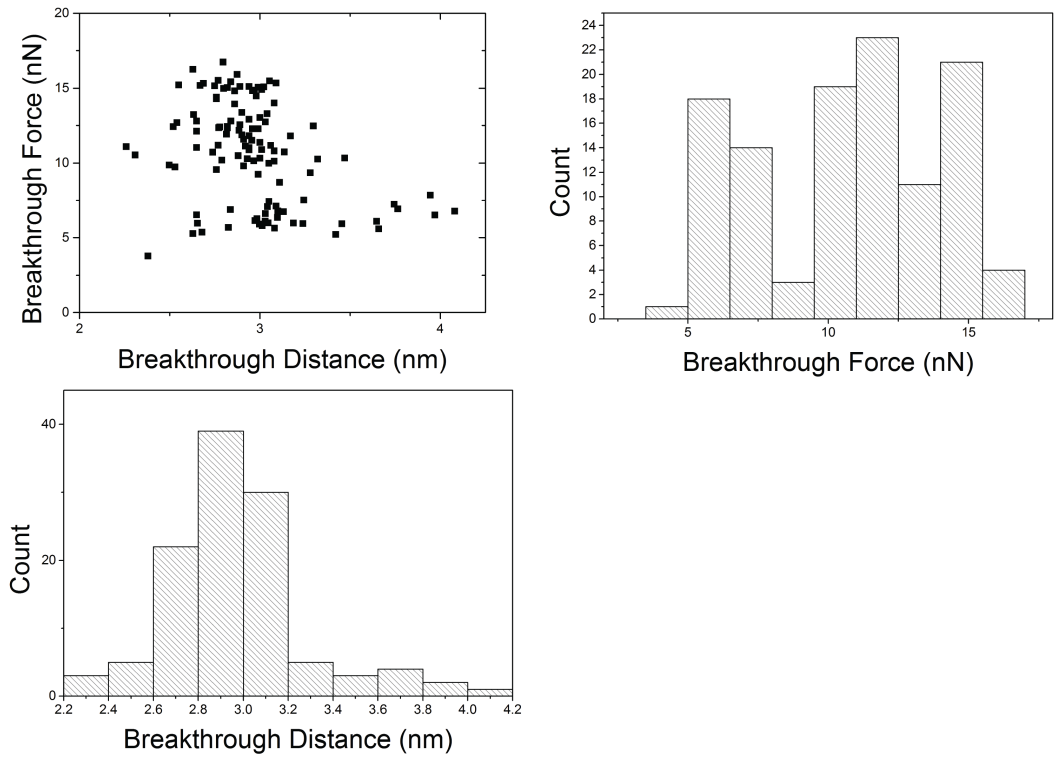

Figure 3.10: Breakthrough force vs. breakthrough distance for DAPC:DPhPC:Chol (1:1:1); n =120.

On increasing the hydrocarbon chain length of the saturated-PC, the breakthrough force (and thus yield strength) of both L_O and L_D regions of the lipid bilayer are seen to increase, with the more pronounced increase observed in the saturated-PC rich, L_O region. This observations agrees qualitatively with force spectroscopy experiments of single component, saturated-PC bilayers (reported by Garcia-Manyes[77]), that have

shown that breakthough force increases linearly from 15 to 35 nN on increasing chain length from DMPC (C_{14}) to DAPC (C_{20}), although in the absence of cholesterol such lipids adopt the gel (L_β) phase at room temperature and therefore such a comparison is not direct. The marked increase in breakthough force on increasing the hydrocarbon chain length to C_{20} could be indicative of a gel phase emerging locally under the AFM tip under the application of load. It cannot however be discounted that this increase is an artefact of mechanical force measurement with a nanoscale probe, whereby the geometry of the AFM tip is liable to deviations between individual tips, whilst the tip itself can also be compromised over the course of an experiment. As the force measurements presented here were conducted with different AFM tips (that originated from an individual batch), the variability in tip geometry must be considered. The measured breakthrough distance is relatively constant for all saturated-PC systems, with values between 3-4 nm, and does not represent the most accurate value of bilayer thickness. However, measurements *via* SAXS are also skewed owing to the inclusion of a hydration layer between stacked bilayers. For the purposes of deriving an estimate of line tension (as outlined in *section 3.3* below), a value of 2.0 nm is taken as the average thickness of a lipid *monolayer*, as a more thorough value was not obtained in the force spectroscopy experiments presented here.

3.3 Height mismatch, domain circularity and line tension

The AFM images obtained are rich in spatial information that can be used to comprehensively map domain morphology for given lipid systems. In contrast to fluorescence microscopy and SAXS, AFM can provide images of phase separation in the plane of the membrane whilst simultaneously measuring the hydrophobic mismatch at the domain edge, resulting in the most powerful individual technique for such experiments.

3.2.1 Height mismatch

As the AFM images represent a topographical map, the height mismatch between distinct domains can be easily extracted either by taking or cross-section through the domain edge, as is given alongside the AFM images shown in *figures 3.4* and *3.5*, or by

plotting a histogram of the measurement in the z direction (i.e. height) for each pixel in the image and extracting the peak-to-peak distance. Extracting height mismatch from all data points in the image gives a robust value of height mismatch, reflecting a complete data set, and is therefore adopted here. The associated error in height mismatch is derived from the full width half maximum of the two respective Gaussians that are fitted to histograms of z data that display two distinct distributions corresponding to the coexisting L_O and L_D phases.

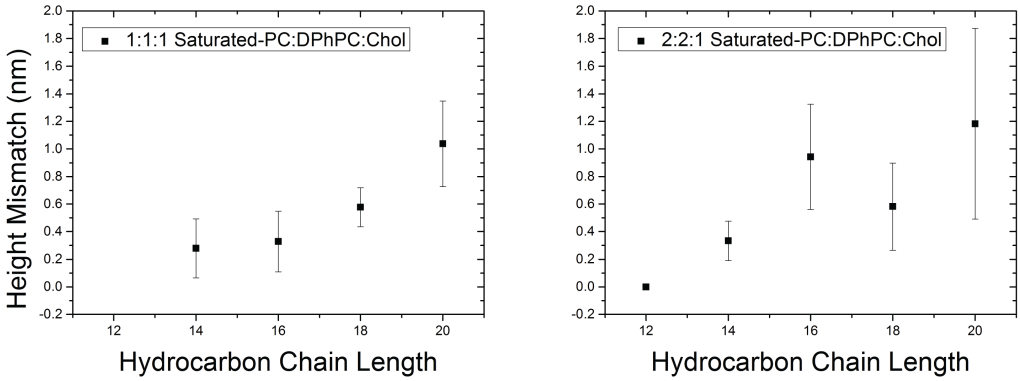

Figure 3.11: Height mismatch vs. hydrocarbon chain length for both 1:1:1 and 2:2:1 mixtures of saturated-PC:DPhPC:Chol.

The height mismatch for both 1:1:1 and 2:2:1 mixtures of saturated-PC:DPhPC:Chol are shown to increase upon increasing the hydrocarbon chain length of saturated-PC, as is shown in *figure 3.11* above. As the measurement of height mismatch is taken from fitting the z values in a topographical map of the model membrane surface to two distinct Gaussians (corresponding to the two distinct heights observed), the error values presented here are propagated from the full-width half-maxima of these Gaussian fits.

3.2.2 Domain circularity

The morphology of the individual domains, as formed *via* nucleation and growth, gives a qualitative indication of the magnitude with which the line tension is acting; a large line tension favors the formation of circular domains that minimizes the length of the domain edge. The domain circularity (i.e. how far the domains deviate from a perfect circle) can therefore be used to identify trends in the manner in which line tension is acting, and how the height mismatch at the domain edge impacts upon this morphology.

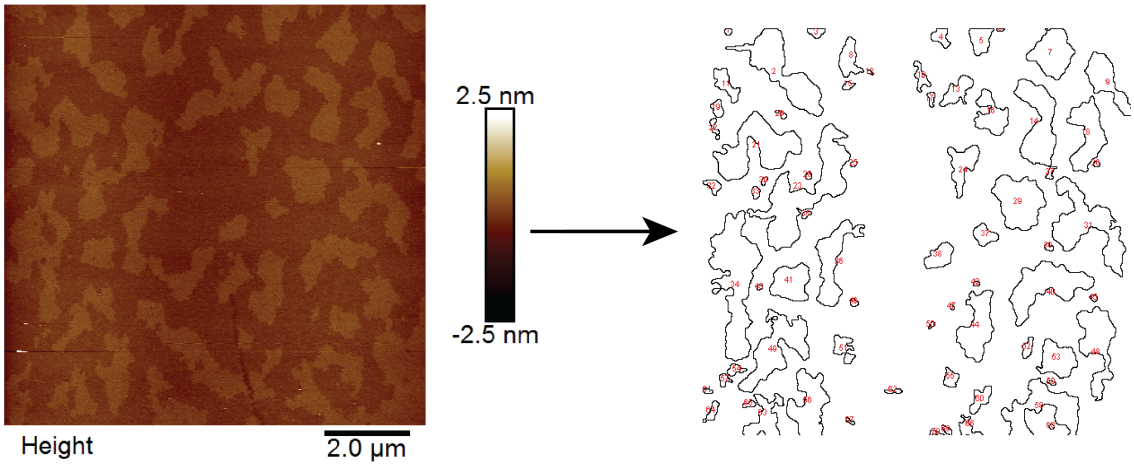

Figure 3.12: Domain circularity is obtained by extracting profiles of the domain edges from AFM images, as shown here for 1:1:1 mixtures of DMPC:DPhPC:Chol (where there is little contrast between domains as the height mismatch is ca. 0.2 nm, and thus represents the most challenging image for image processing as contrast is required to extract the domain edge). The area occupied by the domain and its associated perimeter can then be used to calculate domain circularity. In order to maintain the perimeter of full domains, and discount domains that extend beyond the field of view, care is taken to select domains where the full perimeter is observed with clear contrast against the background.

To extract a value of domain circularity from AFM images, images were initially plane levelled and flattened using proprietary AFM software (Nanoscope Analysis) prior to processing in ImageJ; converting the images to binary allowed for domain edges to be picked (as shown in *figure 3.12*). For mixtures in which there is little contrast between the L_O domains and the L_D matrix (i.e. for DMPC where the height mismatch at the domain edge is ca. 0.2 nm), a smoothing function must be applied prior to converting the image to binary. Domain circularity is then calculated as:

$$Circularity = 4\pi\left(\frac{Area}{Perimeter^2}\right)$$

where a value of 1 is obtained for a perfect circle.

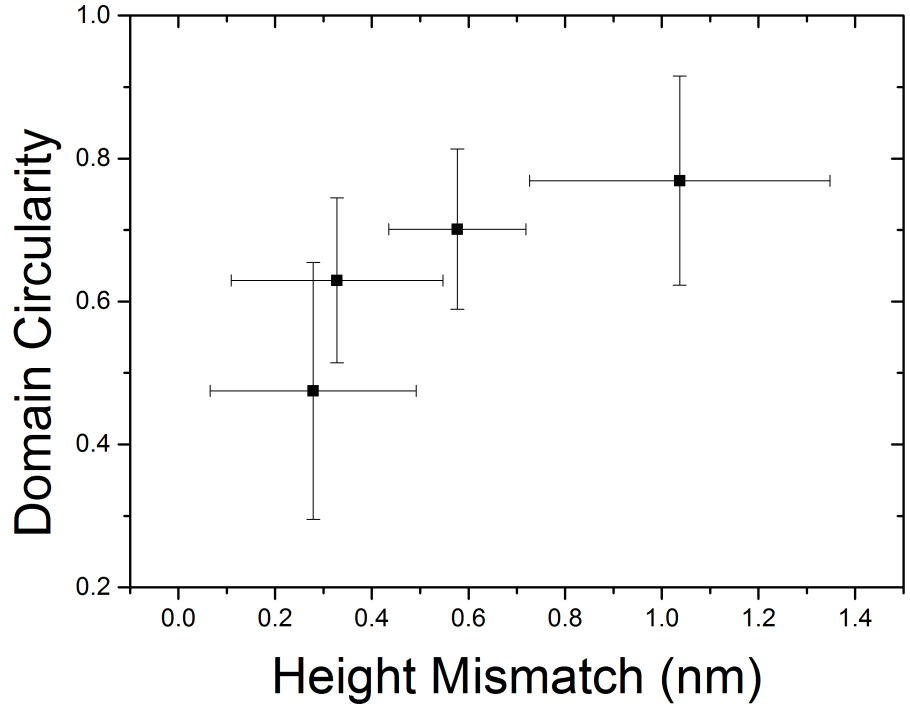

Figure 3.13: Height mismatch vs. domain circularity for 1:1:1 mixtures of saturated-PC:DPhPC:Chol. Circularity is calculated for each distinct domain (n = 20 per saturated-PC system); the average (mean) value is plotted with the standard deviation given as the error.

Plotting the domain circularity against line tension, as shown in *figure 3.13* above, shows that the circularity of individual domains to tends towards 1 upon increasing the height mismatch, with an apparent logarithmic growth. Thus, as domains reach higher values of height mismatch and the system tends towards it's limiting state where domains are perfectly circular, further increases in height mismatch result in incremental further increases in domain circularity.

3.2.3 Line tension

Direct measurement of line tension is possible if dynamic imaging techniques are viable, allowing for its derivation from the analysis of fluctuating domains[90]. As the AFM work presented here does not have the temporal resolution to observe such fluctuations (as frame rates are of the order of minutes), estimates of line tension (γ) can be obtained by inserting values of height mismatch into the equation below, as derived in the theoretical model constructed by Cohen[92] and applied experimentally by Schwille[94].

The line tension, γ, is given as:

$$\gamma = \frac{\sqrt{B_s K_s B_r K_r}}{\sqrt{B_r K_r} + \sqrt{B_s K_s}} \cdot \frac{\delta^2}{h_o^2} - \frac{1}{2} \cdot \frac{(J_s B_s - J_r B_r)^2}{\sqrt{B_r K_r} + \sqrt{B_s K_s}}$$

where r denotes the liquid-ordered ('raft') regions and s denotes the liquid-disordered ('surround') region, δ is the height mismatch at the domain boundary, $h_o = (h_r + h_s)/2$ where h is the monolayer thickness, B is the elastic splay modulus, K is the tilt modulus and J is the spontaneous curvature of the monolayer. As values of the the elastic moduli are not known for the systems studied, approximations are made according to Schwille whereby a 'soft' liquid domain is assumed with $B_r = B_s = 10kT$, $K_r = K_s = 40\ mN/m$ and $J_r = J_s = 0$. The value of monolayer thickness (h_o) can be taken as half the associated bilayer thickness, with values informed from breakthrough distance as measured by AFM (with a value of $h_o \cong 2.0\ nm$, as discussed in *section 3.2*); it must be noted that by taking the breakthrough distance as bilayer thickness, an underestimate is obtained, as during the measurement the bilayer is placed under compression prior to the jump-to-contact. Alternative values of h_o can be obtained from SAXS measurements of equivalent systems (as performed by Nicola McCarthy), with an average value of bilayer thickness taken from the point at which the 3-component mixture becomes miscible ($h_{o(DMPC)} = 3.1\ nm$; $h_{o(DPPC)} = 3.3\ nm$; $h_{o(DSPC)} = 3.4\ nm$); such values derived from SAXS represent an overestimate as the bilayer is in excess water and thus hydration layers are included in the measured d-spacing. The height mismatch at the domain boundary, δ, is obtained from AFM data as presented in *figure 3.11*, with estimates of the line tension, γ, given in *table 3.2* below.

Saturated-PC	Hydrocarbon Chain Length	Height Mismatch (nm)	Domain Circularity	Line Tension (pN)
DMPC	14	0.28 ± 0.21	0.48 ± 0.18	0.40
DPPC	16	0.33 ± 0.22	0.63 ± 0.12	0.55
DSPC	18	0.58 ± 0.14	0.70 ± 0.11	1.71
DAPC	20	1.04 ± 0.31	0.77 ± 0.15	5.50

Table 3.2: Values of height mismatch, domain circularity and the estimated line tension for 1:1:1 mixtures of saturated-PC:DPhPC:Chol.

The estimated line tensions are on the order of pN, and are thus within the same order of magnitude as those reported previously, both from experimental observations of fluctuating domains[90] and from calculations using lipid splay and tilt[92].

3.4 Determining the mixing/demixing temperature by DSC and SAXS

Beyond AFM, thermal analysis by DSC can provide information on the 'mixing/demixing temperature' of the system studied (i.e. the point at which the liquid-liquid domains become miscible, as shown in *figure 3.14*), allowing for the miscibility point of the system to be correlated with the line tension that acts at the domain boundary. Further structural studies at differing temperatures, utilizing SAXS, can differentiate between a single phase and two-phase system[13], and is therefore applied to identify the mixing/demixing temperature in systems that do not yield a signal by DSC. An analogous approach is possible with AFM[10], albeit requiring fine temperature control that was not available *in-house*.

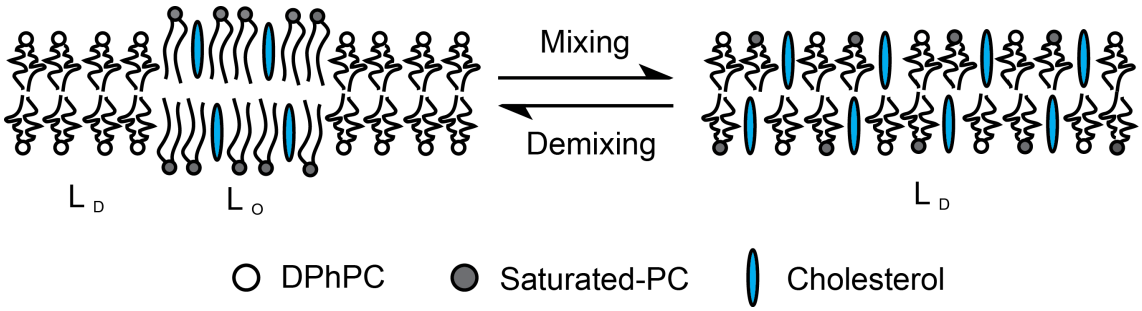

Figure 3.14: Schematic denoting the structural changes upon mixing and demixing of the saturated-PC:DPhPC:Chol system.

3.4.1 DSC as a means of determining demixing temperature

Differential scanning calorimetry can identify a phase transition that has an associated enthalpy, and therefore provides a possible means of determining the mixing/demixing temperature of the three-component lipid system. However, as there are only subtle structural differences between the L_O and L_D phases (as the L_O phase is expected to 'melt' and become miscible with the L_D phase above the demixing temperature), any enthalpy associated with the transition is likely to be small and may lie beneath the detection limits of the DSC. Indeed, no signal was obtained for 1:1:1 mixtures containing DMPC and DPPC, where the height mismatch between domains is small and the structural transformation between coexisting L_O/L_D and single phase L_D is therefore negligible. Lipid systems with a larger degree of higher mismatch yielded a mixing/demixing temperature with the application of relatively high heating and cooling rates of 30 °C/min, as a means of boosting the recorded DSC signal at the expense of resolution in temperature. For 1:1:1 mixtures containing DSPC and DAPC, mixing/demixing temperatures of 48 and 61 °C respectively were recorded (as taken from the centre of the peak rather than peak onset, owing to the breadth of the observed transition that results from the high heating rate).

3.4.2 SAXS as a means of determining demixing temperature

Coexistence between two distinct lamellar phases gives rise to peak splitting in the SAXS patterns obtained from their bulk lipid mixtures[13]; such reflections at distinct values of S (where lower S corresponds to the thicker, L_O bilayer) therefore provide sensitive means of getting a handle on the demixing temperature for systems where thermal analysis fails. As a result, SAXS experiments (performed by Nicola McCarthy; unpublished data) yielded demixing temperatures for 1:1:1 mixtures containing DMPC, DPPC and DSPC of 26, 39 and 48 °C respectively, as shown in figure 3.15.

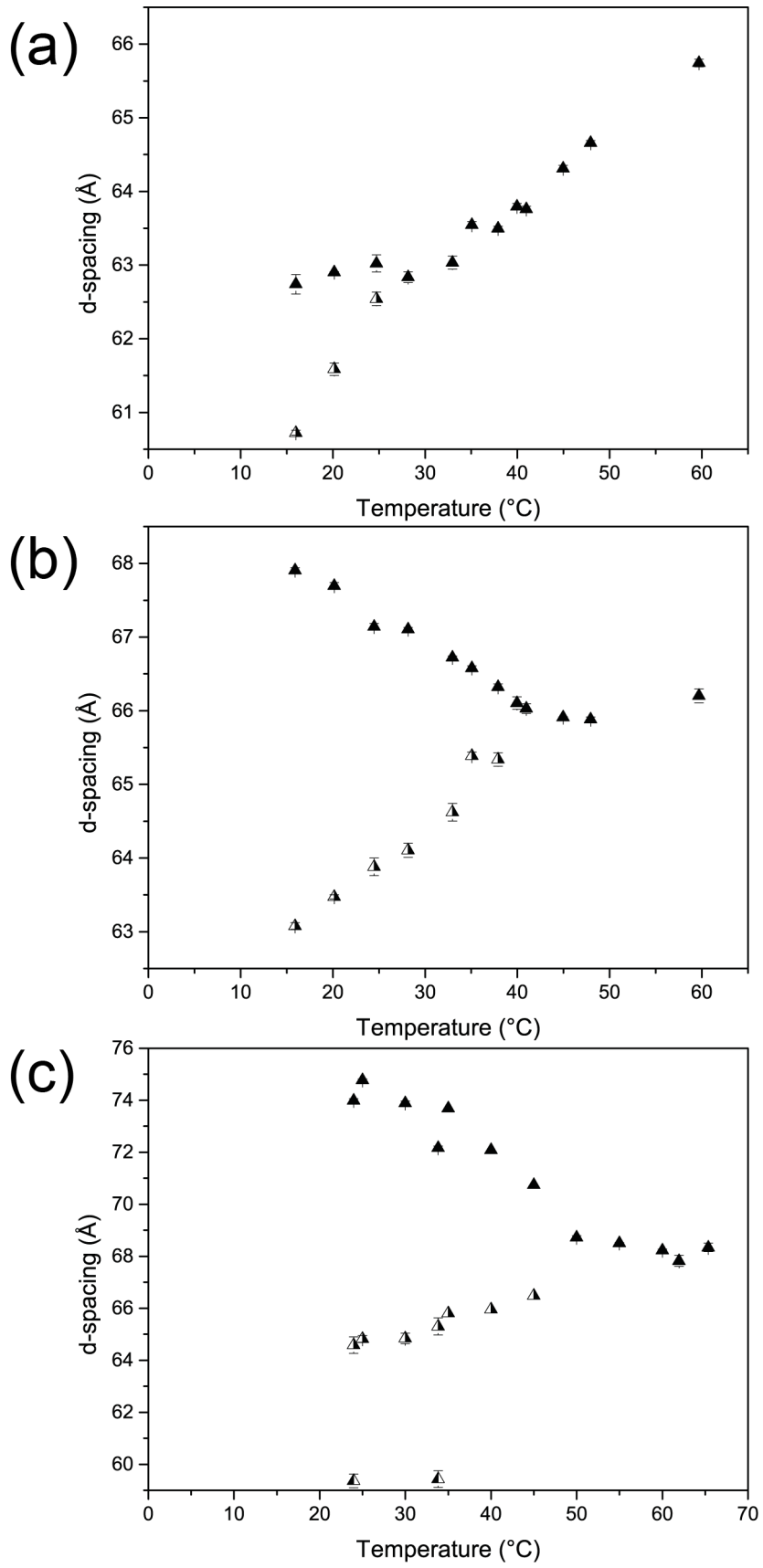

Figure 3.15: SAXS plots of d-spacing vs. temperature for 1:1:1 mixures of saturated-PC:Chol:DPhPC where saturated-PC is (a) DMPC, (b) DPPC and (c) DSPC. The splitting in the d-spacing arises from the coexistence of liquid-ordered and liquid-disordered lamellar phases,

where the magnitude of the splitting can be taken as the height mismatch, in good agreement with the AFM measurements discussed previously. It can be seen that upon increasing temperature, the splitting converges until there is not height mismatch; this can be taken as the mixing/demixing temperature where calorimetric analyses do not yield any insight. *Experiments perforemed and data analysed by Nicola McCarthy.*

3.4.3 Effect of line tension upon demixing temperature

As has previously been reported[94], line tension for a given system as determined at constant (room) temperature, is shown to increase with an increasing demixing temperature, as shown in *table 3.3* below.

Saturated-PC	Line Tension (pN)	Demixing Temperature (°C, DSC)	Demixing Temperature (°C, SAXS)
DMPC (C_{14})	0.40	-	26
DPPC (C_{16})	0.55	-	39
DSPC (C_{18})	1.71	48	48
DAPC (C_{20})	5.50	61	-

Table 3.3: Table showing line tension as derived from AFM measurements of height mismatch, and the demixing temperatures measured by DSC and SAXS for 1:1:1 mixtures of saturated-PC:DPhPC:Chol.

This increase in demixing temperature reflects the associated increasing energetic cost in overcoming the interfacial energy (i.e. line tension) at the domain edge in order to allow for complete mixing of the three-component system. Thus, height mismatch increases line tension, which in turn increases the energetic barrier to the mixing of domains.

3.4 Conclusions and Outlook

AFM imaging of supported lipid bilayers comprised of 1:1:1 and 2:2:1 mixtures of saturated-PC:DPhPC:Chol has shown that phase coexistence occurs throughout all systems studied, with 1:1:1 mixtures yielding the most stable coexisting L_O/L_D domains. Extracting the height mismatch between the distinct domains allowed for an estimate of line tension to be obtained according to the theoretical framework outlined by *Cohen*[92];

it was shown that increasing the height mismatch between domains gave rise to an increase in line tension. In addition, the circularity of domains could be determined as a function of their respective area/perimeter ratio (for 1:1:1 mixtures only), with an increase in height mismatch (and thus line tension) driving the formation of more circular domains. Finally, the mixing/demixing temperature is shown to scale with the derived value line tension, reflecting the increased energetic cost to mixing that an increased line tension imposes.

Despite superficially reflecting the subtle relationships between the factors that act to govern the size and morphologies of membrane microdomains, the body of work presented here is far from complete. A comprehensive survey of compositional space is required for each distinct system (i.e. for each saturated-PC, a compositional phase diagram is required at a given temperature), in order to understand how the relative composition of the phase-separated system shifts with height mismatch. Whilst the height mismatch been the two liquid phases is controlled to an extent by the relative lengths of the hydrocarbon chains, it is also likely affected by how close in phase space the distinct liquid phases are; when the tie-line of the two phase region is short, the two phases are in close proximity and thus the height mismatch will tend towards lower values. As the three-component systems presented here deal with only two distinct compositions (i.e. 1:1:1 and 2:2:1 saturated-PC:DPhPC:Chol), this phenomena is not adequately represented, with emphasis thus placed on the relative lengths of the hydrocarbon chains present.

It is however demonstrated that routine AFM methodology can be applied to gain an interesting preliminary insight into the interplay of height mismatch, line tension and domain morphology, establishing the viability of studying such systems *in-house*, although a comprehensive survey of compositional space is required to draw thorough conclusions. It is anticipated that regulation over lipid composition, and thus height mismatch, may act to control the size, morphology and lifetime of lipid 'rafts' *in vivo*, although the super-resolution methodologies required to corroborate such hypotheses are still somewhat in their infancy[8]. Possibly the most revealing and plausible area for immediate future study would be in the application of fast-scan AFM[81] in tracking the

temporal evolution of domain nucleation, allowing for the critical radius to be determined at previously inaccessible length scales for such model membrane systems, thus demonstrating the minimum size of model raft analogues whilst controlling the degree of height mismatch through the chosen lipid composition.

Chapter 4: Sphingomyelin ripple phase disruption by the addition of ceramide and cholesterol dopants

Sphingomyelins comprise a group of phospholipids containing a sphingosine backbone with an additional hydrocarbon (fatty acid) chain and a phosphocholine headgroup (chemical structure shown in *figure 4.1 (a)*)[109]. They make up a significant proportion of the lipid composition in mammalian cell membranes, with local outer membrane concentrations reaching up to 15 mol %, and are found in particular abundance in the insulating myelin sheath that surrounds nerve cell axons. In addition, sphingomyelin plays a significant role in cell signaling pathways, notably in its hydrolysis by sphingomyelinase to give a ceramide molecule (by the removal of the phosphocholine headgroup), which has been found to be implicated in apoptosis (i.e. programmed cell death)[110,111]. Sphingomyelin is often found to possess a significantly higher degree of saturation in its hydrocarbon chains than other phospholipids, and tends to aggregate with sterols (i.e. cholesterol) in the liquid ordered phase of lipid bilayer membranes[10]. It has therefore been proposed to be an important molecule in the formation of lipid microdomains, often referred to as lipid 'rafts', which are postulated to concentrate membrane proteins and thus compartmentalize and focus their bioactivity[5].

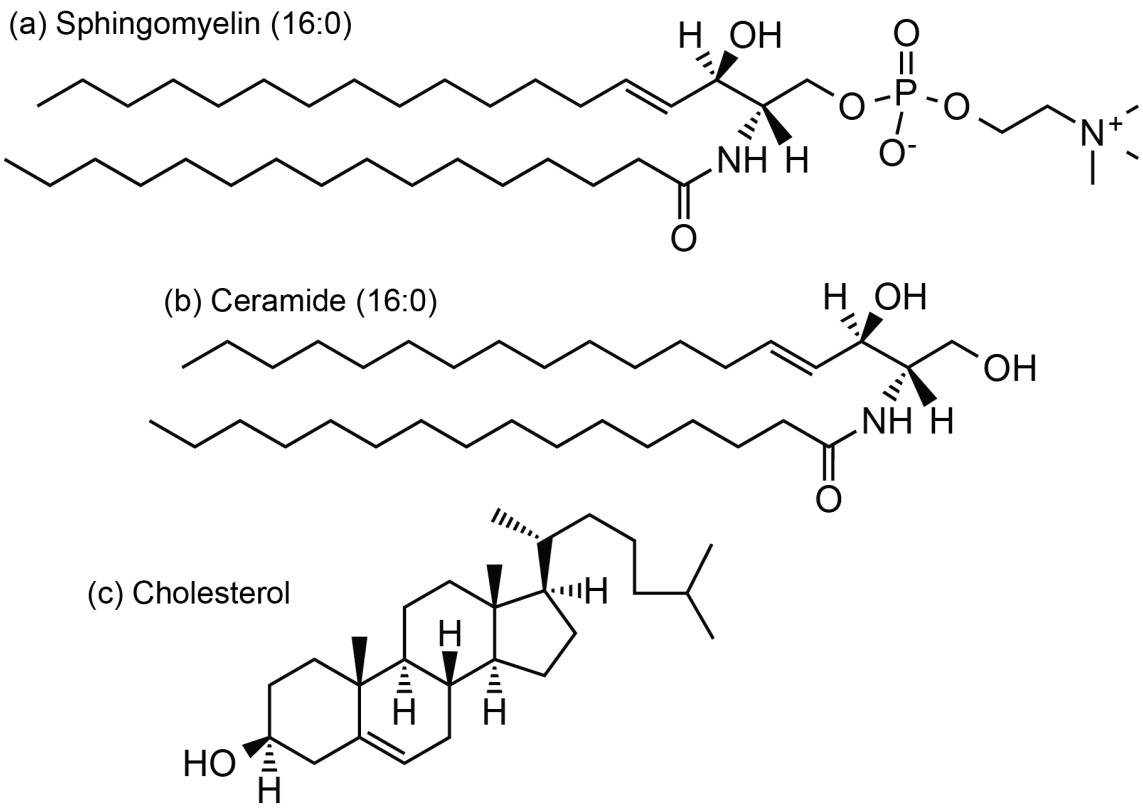

Figure 4.1: Chemical structures of (a) sphingomyelin, (b) ceramide and (c) cholesterol. The sphingomyelins and ceramides used in this work are extracts from egg-yolk, with chemical species (a) and (b) comprising the predominant species (reported by the supplier (Avanti Polar Lipids, Alabaster, Alabama USA) as accounting for 86 mol % of the total lipid extract).

It is interesting to contrast the very different ways in which cholesterol and ceramide respectively affect the phase behavior of sphingomyelin, which in turn is likely to be a key effector in the mechanism of action of both ceramide as an apoptotic signaling molecule[109], and of cholesterol as a promoter of lipid rafts *in vivo*[7]. Owing to the high degree of hydrocarbon saturation of sphingomyelin, they tend to have a gel-to-fluid (L_β-to-L_α) transition that is strikingly close to physiological temperatures (ca. 37 ° C)[112,113]. Ceramide's have an even higher gel-to-fluid transition temperature, as the phosphocholine group (present in sphingomyelin) is absent and therefore the molecule is increased in its hydrophobicity, giving a relative increase in interactions between the hydrocarbon chains and thus it's propensity to reside as a fluid (L_α) lyotropic phase is lowered. It is therefore likely that by doping sphingomyelin with ceramide, a gel (L_β) phase lipid bilayer will be most favored. In contrast, cholesterol disrupts the packing of

the sphingomyelin hydrocarbon chains in the gel phase and gives rise to the liquid-ordered (L_O) phase, in which rapid diffusion of the respective lipid molecules occurs (cf. gel phase), but conformational order of the hydrocarbons chains is retained (whereby they reside in the *trans*-state). It is therefore possible to hypothesize that the physicochemical properties of these distinct classes of molecules (sphingomyelins, ceramides and cholesterol respectively) have a direct impact upon the roles as signaling molecules that they have adopted in vivo.

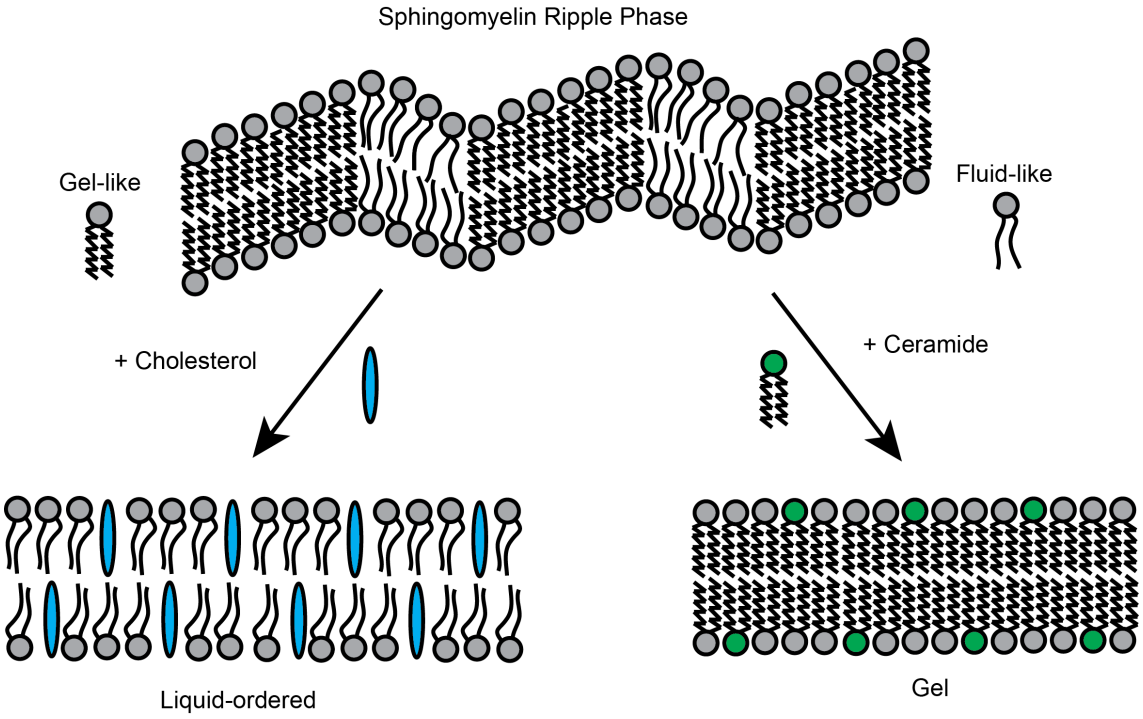

Figure 4.2: Schematic of sphingomyelin ripple phase disruption with the addition of cholesterol and ceramide dopants. Cholesterol drives the formation of the liquid-ordered phase by disrupting the packing of the crystalline hydrocarbon tails, whereas ceramide acts to consolidate the gel phase.

In isolation of any dopants and as an intermediate between the fluid and gel phases, egg-yolk sphingomyelin is found in the ripple phase (P'_β) at temperatures below it's main phase transition (ca. 39 °C). Although the biological significance of this lyotropic phase is not well understood, the local coexistence of ordered and disordered lipid assemblies is thought to play a crucial role in regulating protein function[114]; such coexistence represents a physicochemical property that is intrinsic to the ripple phase. The sawtooth pattern that runs through the plane of lamellar bilayer results from the packing of the

individual lipid molecules; this rippling lies as an intermediate between the molecular packing of the fluid (L_α) lamellar phase and the planar gel (L_β) phase, accommodating both entities. A fluid lipid bilayer results when hydrocarbon chains are 'melted' and thus possess considerable conformational disorder; the bilayer is statistically flat although thermal fluctuations result in undulations within the bilayer[115]. In contrast, the L_β gel phase has near-crystalline molecular packing, in which the hydrocarbon chains are in the *trans*-state but with significant rotational disorder in the plane perpendicular to the bilayer. In the ripple (P'_β) phase, contributions can be found from both the gel (L_β) and fluid (L_α) phases; the lipid molecules in the longer edge of the sawtooth profile reside in a close packed gel-like conformation, whereas the lipid hydrocarbon chains along the shorter edge are more fluid in order to accommodate the periodic rippling of the bilayer. It has been suggested that the P'_β ripple phase indeed represents two structurally related but thermodynamically distinct phases[116]. This P'_β ripple phase has been studied by a plethora of structural techniques including SAXS[117,118], NMR[119] and AFM[120-122], and has been the subject of both computational[114] and theoretical models[123], but studies have largely focused on gaining a full understanding of the structure of the ripple phase, rather than on it's biological significance.

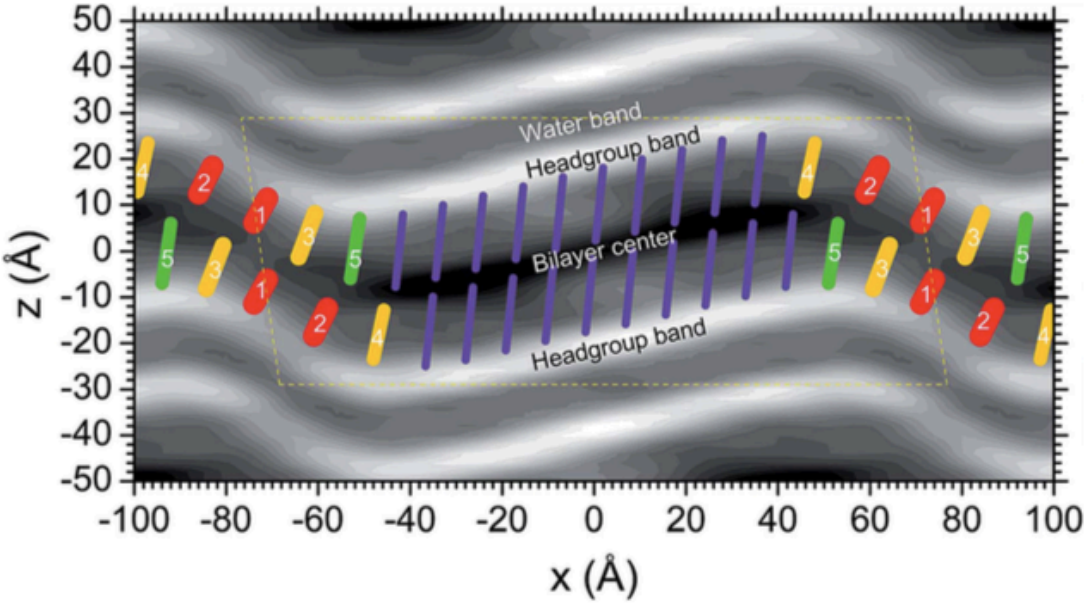

Figure 4.3: Electron density map of the DMPC ripple phase, as calculated from scattering data from an aligned sample that gave rise to 57 Bragg reflections. The high-resolution electron density profile can thus be interpreted as containing contributions from both *gel*- and *fluid*-like molecular packing. Purple lines represent the *gel*-like crystalline packing of the hydrocarbon chains in the longer arm of the ripple; red lines (1) and (2) represent *fluid*-like packing; yellow (3, 4) and green (5) lines represent intermediate chain packing necessary to accommodate the ripple. *Taken from*: K. Akabori *et al.*, *Soft Matter* **11**, 918–926 (2015).

The work presented here aims to gain an insight into the phase behavior of mixtures of extracts of egg-yolk sphingomyelin and egg-yolk ceramide; two related molecular species of significant biological interest. With an understanding of the bulk phase behavior of these mixtures (as determined by DSC and SAXS respectively), it is revealing to probe their structures locally (i.e. by AFM), specifically in observing local disruption to the sphingomyelin ripple (P_β') phase with the addition of ceramide. Such observations are not possible with ensemble (SAXS) techniques as the disruption of the ripple phase likely leads to far fewer repeating lattices that would give rise to reflections, and in addition the dimensions of the ripple period is often pushed beyond the limits of the detector (as determined by the distance of the camera from the sample; to resolve larger structures, smaller angles and thus longer flight tubes are required). The disruption of the sphingomyelin ripple phase by ceramide is contrasted with the effect of the addition

of cholesterol; the *liquid-ordered* (L_o) phase is formed, likely via a very different mechanism of ripple (P'_β) phase disruption than that which tends towards a gel.

4.1 Phase behavior of bulk sphingomyelin:ceramide mixtures

In order to probe the interplay of sphingomyelin with both ceramide and cholesterol, as it is likely to be found at elevated local concentrations in eukaryotic cell membranes during apoptosis and lipid raft formation[109], the phase behavior of model SM:Cer and SM:Chol systems must be understood. Systems containing sphingomyelin and cholesterol have been studied extensively owing to their prevalence as model systems which mimic lipid rafts[9,10,124]. There is however a dearth of information of how sphingomyelin interacts with ceramide, although they are likely to be found in close proximity and at local elevated concentrations *in vivo* when sphingomyelin molecules are cleaved of their phosphocholine headgroup to give ceramide. It is therefore necessary to construct a phase diagram of mixtures of sphingomyelin and ceramide in order to understand how their interplay affects their bulk phase behavior, as it is conceivable that the bulk biophysical properties of these interconnected molecules will have implications for their role as signaling molecules *in vivo*.

The work presented in this chapter is the result of studies of extracts of both egg-yolk sphingomyelin and egg-yolk ceramide. Although this leaves some ambiguity in the molecular composition of their respective mixtures, they have been used extensively in the study of model lipid bilayer membranes, and each respective extract was here found to exist in a single lyotropic phase (in fully hydrated conditions and at room temperature). *Egg-yolk* sphingomyelin and ceramide were chosen (in contrast to extracts from *milk* or *bovine brain*) as they contain a much smaller distribution of individual molecular components; egg-yolk sphingomyelin is largely comprised of sphingomyelins with saturated C_{16} hydrocarbon chains (86 mol % as reported by Avanti Polar Lipids (Alabaster, Alabama USA), as shown in *figure 4.1*), with the corresponding C_{16} ceramide representing the predominant species of the ceramide extract.

4.1.1 Differential scanning calorimetry: identifying phase boundaries at given compositions

In order to construct a phase diagram for mixtures of sphingomyelin and ceramide extracts, it is revealing to perform calorimetry upon the systems under study in order to identify phase boundaries, thus understanding where distinct phase will be observed when resolving the structure of the system across large windows of both temperature and pressure. Differential scanning calorimetry can identify a phase boundary that is accompanied by a change in enthalpy by measuring the heat required to increase the temperature of the sample relative to a reference[125]. In addition, the heat flow required for the phase change allows determination of whether a transition is endo- or exothermic, and thus gives an indication of the (meta)stability of the lyotropic phase. An example DSC from the literature is shown in figure 4.4 below, in which the pre- and main tranition of DPPC can be observed as endothermic processes where the DPPC gel phase is initially disrupted to give the ripple, which then melts (as it passing through the main phase transition) to give a fluid, liquid-disorded phase.

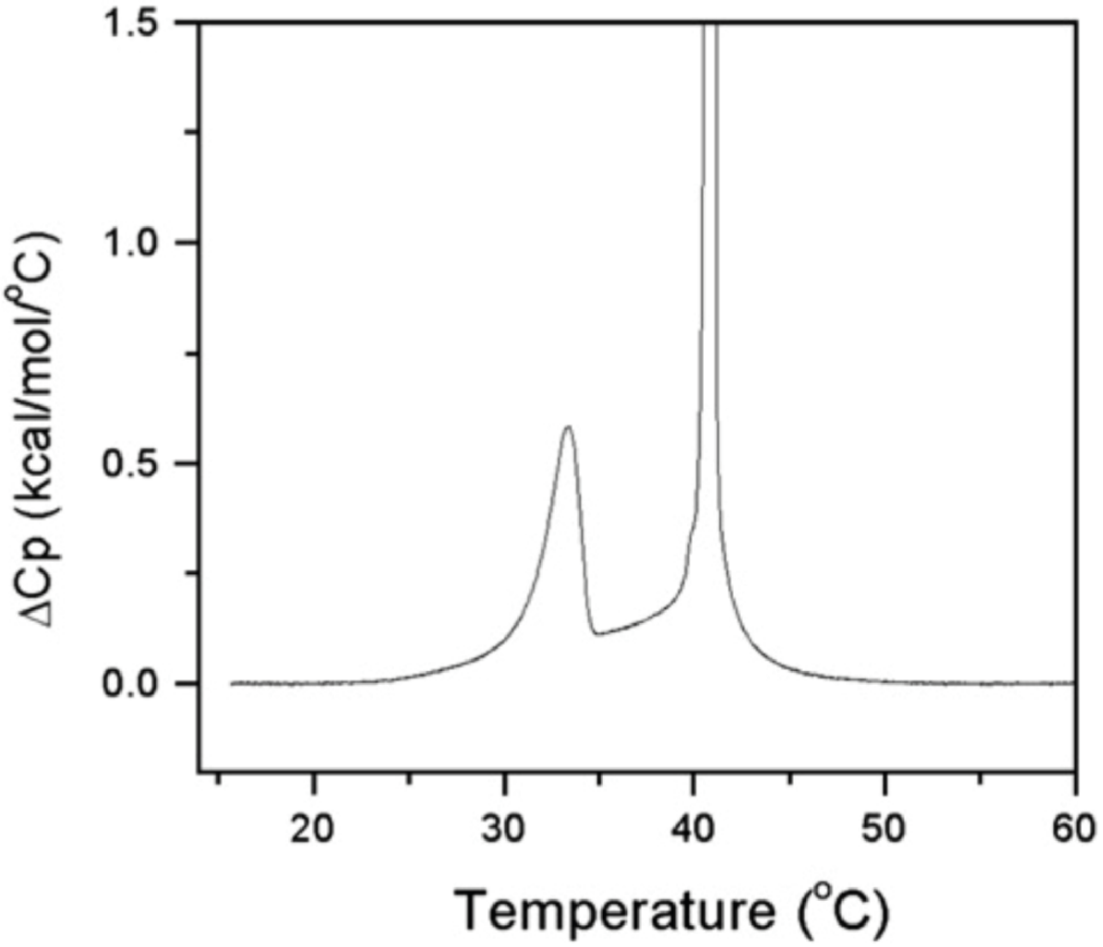

Figure 4.4: Example DSC curve of heat flow (i.e. change in heat capacity) against temperature for hydrated DPPC, with a main phase transition temperature of 41 ºC which corresponds to gel to fluid melting. The pre-transition, which corresponds to the gel-ripple, is observed as a peak at ca. 32 ºC that is much weaker relative to the main transition. *Image taken from:* K.A. Riske *et al.*, *Biochemica et Biophysica Acta* **1788** (2009) 954-963.

The main transition temperatures (i.e. *gel*-to-*fluid*, *P(β')* -to-*L(α)*) for hydrated SM has been reported to be 37-40 °C[126], whilst pure 16:0 ceramide has been shown to exist as a *metastable* gel before transitioning to a stable gel at 50-70 °C, as evidenced by the exothermic transition observed in the DSC curve[127]. The main *gel*-to-*fluid* transition for pure, hydrated 16:0 ceramide does not occur until ca. 90 °C; an extremely high energetic barrier for it to exist in the fluid phase. However, calorimetric data for mixtures of sphingomyelin and ceramide has not been reported, and therefore provides a novel

starting point for this chapter that will aid the subsequent construction of a phase diagram.

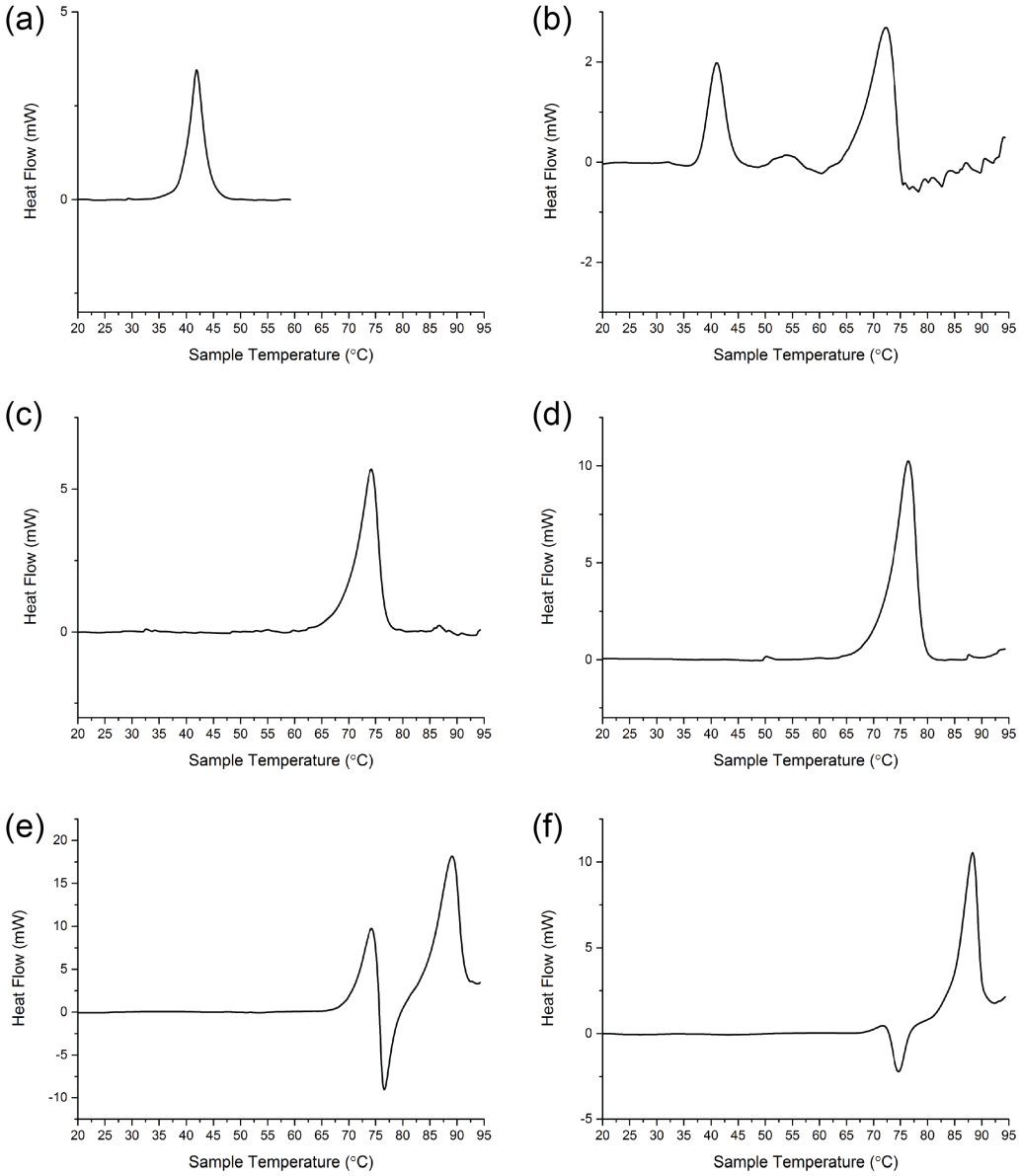

Figure 4.5: DSC traces of sphingomyelin:ceramide mixtures; (a) pure sphingomyelin, (b) 20 mol % ceramide, (c) 40 mol % ceramide, (d) 60 mol % ceramide, (e) 80 mol % ceramide and (f) pure ceramide. All compositions are hydrated with 70 weight % water. Positive heat flow corresponds to an endothermic transition.

Initial DSC traces of the extracts of pure egg-yolk sphingomyelin and egg-yolk ceramide respectively are in good agreement with previous reports of calorimetric data, with pure sphingomyelin displaying a characteristic melting with an onset of ca. 40 °C, corresponding to the *gel* to *fluid* transition. Pure egg-yolk ceramide is also in excellent

agreement with reported DSC data for hydrated 16:0 ceramide[127] (i.e. the predominate species in this extract), in which there is an initial exothermic transition with an onset of ca. 70 °C followed by a second endothermic transition at ca. 85 °C; this distinct inversion in heat flow corresponds to a metastable-to-stable gel transition, followed by the melting of the stable gel to give the fluid lamellar phase (as visible in the DSC traces shown in *figure 4.5*). DSC traces for intermediate compositions of hydrated sphingomyelin:ceramide mixtures display contributions from the the pure extracts. At 20 mol % ceramide, the sphingomyelin gel-to-fluid transition at ca. 40 °C remains, with the emergence of an additional endothermic transition at ca. 65 °C which is attributed to ceramide gel melting that is significantly lowered in the presence of sphingomyelin, and with the absence of a metastable gel state. In combination with SAXS data (discussed below in *section 4.1.2*), this transition corresponds to a gel-fluid phase transition of a ceramide-rich region of the sample. At 40 and 60 mol % ceramide, there is a single endothermic transition at ca. 65 °C, attributed to ceramide gel melting to give a hexagonal phase, with the minor sphingomyelin component acting to inhibit the formation of a metastable gel. At 80 mol % ceramide, the DSC trace largely resembles that of pure ceramide, albeit with a large energy barrier to the formation of the metastable gel. These transitions are tabulated along with literature values for the pure sphingomyelin and ceramide components in table 4.1 below; the transition temperature is given as the onset of the transition (i.e. where the tangent to the maximum gradient meets the x axis), with the full-width half maximum giving an insight into the purity of the sample and the cooperativity of the phase transition for a given heating rate[128].

	Primary Transition			Secondary Transition		
Composition (mol % SM:Cer)	**Onset (°C)**	**FWHM (°C)**	**Phase Transition**	**Onset (°C)**	**FWHM (°C)**	**Phase Transition**
100:0	39.3	3.3	$P'_{\beta} - L_{\alpha}$	-	-	-
80:20	38.6	3.7	$P'_{\boldsymbol{\beta}} - L_{\boldsymbol{\beta}}$	66.3	4.9	$L_{\beta} - L_{\alpha}$
60:40	69.3	4.6	$L_{\beta} - H_{II}$	-	-	-
40:60	71.4	4.7	$L_{\beta} - H_{II}$	-	-	-
20:80	67		Metastable-stable gel	82		$L_{\beta} - L_{\alpha}$
0:100	68.7	2.7	Metastable-stable gel	83.9	4.2	$L_{\beta} - L_{\alpha}$
Egg Sphingomyelin[126]	38.8	-	$P'_{\beta} - L_{\alpha}$	-	-	-
16:0 Ceramide[127]	64.2	-	Metastable-stable gel	90.0	-	$L_{\beta} - L_{\alpha}$

Table 4.1: Summary of DSC data for mixtures of sphingomyelin and ceramide in excess water.

4.1.2 Small-angle X-ray scattering: assigning phases

In order to assign phase(s) to the respective regions of a DSC curve above and below the observed phase transitions, structural methods are required. SAXS has been widely applied in the study of lyotropic lipid systems, in which bulk, hydrated lipid mixtures give rise to powder diffraction patterns owing to the repeating liquid crystal lattices inherent to the lyotropic phase. These diffraction patterns can be indexed to characterize the phase present, and the lattice parameters can be derived with prior knowledge of the x-ray wavelength and the distance of the sample to the detector. SAXS is therefore a powerful tool in determining the lyotropic phase and lattice parameters of these self-assembling lipid systems, and can be routinely applied in high-throughput to map the phase diagram of a multi-component lipid system.

As structural, SAXS studies of both sphingomyelin exacts[119] and pure 16:0 ceramide[127] have been reported, it is anticipated that their mixtures will show structural contributions from their pure components. As a result, at low temperatures, only lamellar phases need to be considered for such systems, which have the characteristic powder diffraction patterns of a series of equally spaced concentric rings, with the ripple

gel phase (P'_β) giving rise to additional reflections, which correspond to the additional repeating lattice present in the ripple phase (i.e. the ripple period), and it's combinations with the interbilayer spacing. In order to differentiate between *fluid* (L_α) and gel (L_β) phases, the wide-angle region of the scattering pattern is required. As smaller repeat spacings are probed at larger angles, the wide angle region reveals information related to the packing of the hydrocarbon chains, with a characteristic sharp peak at 4.2 Å corresponding to the semi-crystalline packing of the gel (L_β) phase. A fluid phase bilayer gives rise to a much more diffuse peak with a slightly larger repeat distance (ca. 4.6 Å; the resultant scattering from disordered hydrocarbon chains, which thus occupy a larger lateral area per molecule). At significantly higher temperatures, an increase in splay of the hydrocarbon chains can be expected which would give rise to more curved lyotropic phases, with the hexagonal (H_{II}) phase being the most likely, as ceramide-doped phospholipid systems have previously been reported to maintain such curved structures[129,130].

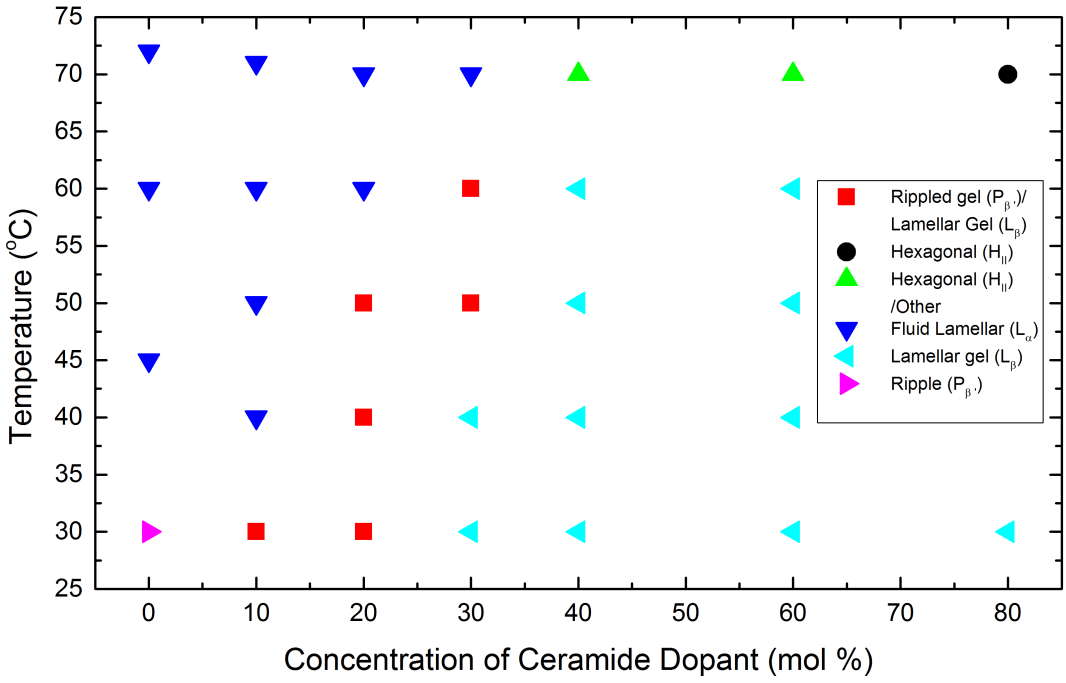

Figure 4.6: Phase diagram of sphingomyelin:ceramide mixtures as a function of temperature.

The temperature-composition phase diagram shown in *figure 4.6* shows a rich variety of lyotropic phases that are adopted by sphingomyelin:ceramide mixtures. Below the main melting transition of sphingomyelin (39.3 °C as measured for this extract), SAXS gives a powder diffraction pattern characteristic of the ripple phase (as shown in *figure 4.6*), with a clear (0 1) peak that corresponds to the ripple period (if the angle γ between the interbilayer spacing, *a*, and the ripple period, *b*, is taken to be equal to 90 °). With low concentrations of the ceramide dopant (10 and 20 mol %), two distinct lamellar phases emerge that are attributed to a sphingomyelin-rich (rippled) gel and a ceramide-rich gel respectively. At increased concentrations of 30 mol % and above, ceramide drives the formation of a single gel phase. On increasing temperature, there is a distinct and cooperative chain melting to give a fluid phase, with a transition temperature that increases with increasing concentrations of ceramide. At low concentrations of ceramide, this chain melting corresponds to a transition to the fluid lamellar (L(α)) phase. At higher concentrations of ceramide (40 mol % and above), there is a direct transition from a single gel (L_β) phase to the 2D hexagonal (H_{II}) phase at ca. 65 °C; the small headgroup area of

ceramide is thought to induce the formation of such curved structures, further compounded by an associated splay in the fluid hydrocarbon chains that occurs at elevated temperatures. SAXS patterns at higher ceramide concentrations and temperatures showed further reflections at lower values of reciprocal spacing (s), labelled on the phase diagram in *figure 4.6* as 'other' but which have preliminarily been assigned to the cubic I_m3_m space group, and could thus constitute either a bicontinuous or discontinuous cubic lyotropic phase, although further verification is needed.

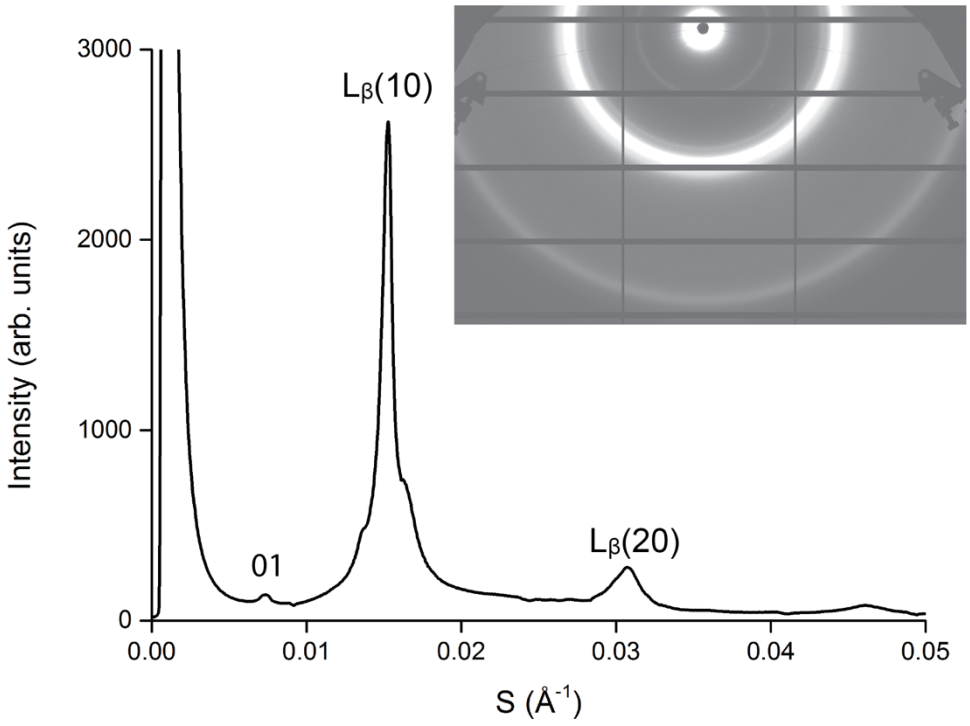

Figure 4.7: SAXS pattern for egg-yolk sphingomyelin hydrated with 70 weight % water, to give the ripple (P'_β) phase. The characteristic 0 1 peak, corresponding to the ripple period, is clearly visible. Further reflections from the ripple lattice cannot be resolved owing to the very strong signal from the 1 0 and 2 0 gel peaks.

With sufficiently resolved scattering patterns from the ripple phase bilayer, it is possible to fully index the powder diffraction pattern that arises from the ripple phase[119]. The ripple has two distinct repeat spacings; the interbilayer distance (a), and the ripple period (b), in which the period of the ripple tends to be greater that the interbilayer spacing. The variable angle (γ) between the two repeats results in an oblique lattice,

which in combination with the repeat spacings a and b gives rise to a large number of reflections in the small-angle region of the diffraction pattern. As the ripple phase is often tilted with respect to the bilayer normal, a, b, and γ cannot be directly extracted directly from the reciprocal space measurements and must be calculated.

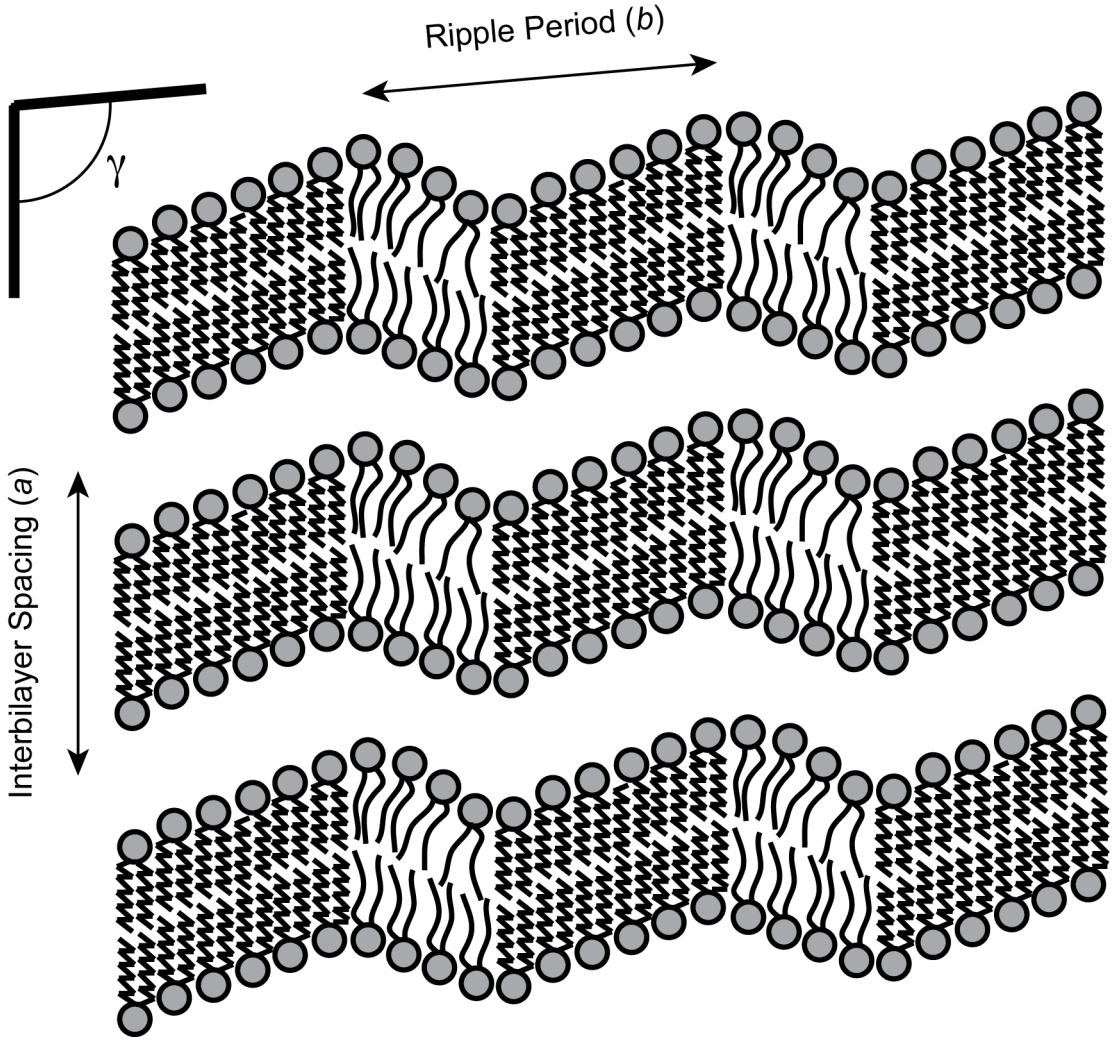

Figure 4.8: Schematic of the ripple phase with lattice parameters for the interbilayer spacing (a) and the ripple period (b), separated by the angle γ.

The lattice parameters for a tilted ripple phase can be calculated as follows. An oblique lattice has a reciprocal lattice given by:

$$S^2 = h^2a^{*2} + k^2b^{*2} + 2hk\ a^{*2}b^* \cos\gamma^*\ (eq.1)$$

Where:

$$a^* = \frac{1}{a \sin\gamma}\ (eq.2)$$

$$b^* = \frac{1}{b \sin \gamma} \ (eq. 3)$$

$$\gamma^* = 180° - \gamma \ (eq. 4)$$

With assignments of the powder diffraction peaks, the above equations can be solved to give the real space lattice parameters *a*, *b* and γ.

For the (0, 1) peak, which corresponds to the ripple period:

$$S^2_{(0,1)} = 0^2 a^{*2} + 1^2 b^{*2} + 2(0)(1) a^* b^* \cos \gamma^*$$

$$S^2_{(0,1)} = b^{*2}$$

For the (1, 0) peak, which corresponds to the interbilayer spacing:

$$S^2_{(1,0)} = 1^2 a^{*2} + 0^2 b^{*2} + 2(1)(0) a^* b^* \cos \gamma^*$$

$$S^2_{(1,0)} = a^{*2}$$

Substituting these values for a^* and b^* into equation (*1*) for the (1, 1) peak allows the equation to be solved to give γ:

$$S^2_{(1,1)} = 1^2 a^{*2} + 1^2 b^{*2} + 2(1)(1) a^* b^* \cos \gamma^*$$

$$\gamma^* = cos^{-1} \left(\frac{S^2_{(1,1)} - a^{*2} - b^{*2}}{2 a^* b^*} \right)$$

$$\gamma = 180° - \gamma^*$$

This value of γ can then be inserted into equations (2) and (3) to give the real space values for lattice parameters *a* and *b* which correspond to the interbilayer spacing and the ripple period respectively. This method has been applied in determining values for *a*, *b* and γ for the DPPC ripple phase[131], with *a* = 7.1 nm, *b* = 13.6 nm and γ = 95 °, where clear (0, 1), (1, 0) and (1, 1) peaks could be resolved at 40 °C (i.e. just below the *gel*-to-*fluid* transition). More recently, it has been shown that the equivalent ripple peaks can be resolved for sphingomyelin extracts[119], but with bovine brain extracts which contain a larger proportion of longer chain and unsaturated sphingomyelins, and only with the

application of hydrostatic pressure. The highest resolution diffraction data for the lyotropic ripple phase has recently been reported for DMPC, where an oriented sample yielded 57 orders of scattering[118]; such high resolution data can then be used to give electron density maps. The powder diffraction pattern from egg-yolk sphingomyelin is of insufficient resolution to distinguish between the individual reflections (see *figure 4.7*), but the (0, 1) and (1, 0) peaks are clearly visible; it is therefore possible to make a first-approximation of real-space measurements of both the interbilayer spacing (*a*), and the ripple period (*b*) with the assumption that the angle γ between these repeats is equal to 90 °. As reports of γ for bovine brain sphingomyelin, DPPC and DMPC are 88-102 °, 95 ° and 98 ° respectively, such an approximation will reasonably yield any trends in the effect of doping the sphingomyelin ripple phase (with both ceramide and cholesterol) on the lattice dimensions of the ripple. With this assumption, the ripple period for egg-yolk sphingomyelin in excess water is calculated as 14.1 nm with an interbilayer spacing of 67 Å.

4.1.3 Pressure effects: consolidating assignments

The application of hydrostatic pressure to soft matter systems has provided a method of probing structural dynamics with milli-second resolution, as pressure acts as a thermodynamic variable that propagates at the speed of sound (c.f. temperature), and has little effect upon the chemical bonds within the system (at moderate pressures of ca. 2 kbar). In the context of the work presented here, pressure is used to map the phase behavior of SM:Cer mixtures with fast equilibration times that quickly reveal the hysteresis in the system, using the SAXS pressure cell available at Diamond Light Source[84]. In addition, hydrostatic pressure provides a useful tool in verifying *gel* vs. *fluid* assignments; as the gel phase is resistant to significant compression upon application of pressure (as the hydrocarbon in the gel phase are already semi-crystalline), it is possible to distinguish a *gel* from a *fluid* phase by how their interbilayer spacing is affected by the application of hydrostatic pressure, with a fluid phase showing a more pronounced increase in d-spacing upon application of pressure[132]. Pressure-temperature phase diagrams are not shown here (as they are not directly relevant in studying ripple phase

disruption), but were used as an aid in constructing the temperature-composition phase diagram shown in *figure 4.6* and can be found in reference[133].

4.2 Sphingomyelin ripple phase disruption

Sphingomyelin extracts have been reported to exist in the ripple phase below their gel-to-fluid transition (ca. 37 °C, dependent on extract[126]), an observation that has been verified here for egg-yolk sphingomyelin. In light of sphingomyelin's often cited role as a *raft-forming* lipid, the intriguing possibility is offered that in addition to it's coexistence with cholesterol in the liquid-ordered (L_o) phase, it could also induce *gel-fluid* phase-separation *in vivo* in the form of the ripple phase. In a similarly elusive manner to *liquid-ordered* lipid rafts, the ripple phase would evade optical detection *in vivo* as the period of the ripple is below the diffraction limit. As sphingomyelin is likely to coexist locally with ceramide and cholesterol molecules, the mechanism by which these molecules act to disrupt the ripple lattice could give an insight into their biophysical basis as signaling molecules. It is clear that the ripple phase is present in model membrane systems, and therefore it's disruption owing to the interplay of the model membrane's molecular constituents can be probed.

4.1.1 SAXS of sphingomyelin:ceramide mixtures (loss of signal)

Previous experiments have shown that it is possible to obtain clear powder diffraction patterns for the ripple phase formed from sphingomyelin extracts, but the origin of the extract has been observed to have a large effect on the resolution of the Bragg peaks, likely due to the differing molecular contributions in each respective extract, with bovine brain and milk sphingomyelin having a much greater prevalence of both longer chain and unsaturated hydrocarbon chains. The extracts of egg-yolk sphingomyelin used here gives the characteristic SAXS pattern of the ripple phase (as shown in *figure 4.7*), albeit with many of the reflections from the ripple phase overwhelmed by the strong 1 0 and 2 0 peaks corresponding to the gel phase. Crucially, the 0 1 reflection from the ripple period is clearly resolved and can therefore be tracked with the addition of a dopant. Despite the relatively large repeat spacing of the ripple period (b = ca. 130 Å, with associated $S < 0.01$ Å^{-1}), synchrotron SAXS can access such large repeat spacings by

utilizing a longer flight tube (i.e. a larger distance, *d*, between the sample and the CCD detector/camera is required as you go towards smaller angles).

With the addition of ceramide to the sphingomyelin ripple lattice, the ripple period is observed to increase from 13.7 nm for pure sphingomyelin to 15.4 nm with 5 mol % ceramide (as extracted from the SAXS patterns displayed in *figure 4.9*). This increase in ripple period is accompanied by a diminishing signal for the 0 1 peak, with additional reflections also broadening out, suggesting that the global phase behavior of the sample is less cooperative. Beyond 5 mol % ceramide, the 0 1 peak (and thus the ripple period) cannot be resolved; the SAXS peaks remain broad at 10 mol % ceramide, and it is likely that there are insufficient ripple repeats to give rise to reflections, with the additional possibility that the ripple period in a heterogeneous sample is not of a single fixed dimension that would thus give a broad SAXS peak. At higher concentrations of ceramide (15 mol % and above), the SAXS peaks sharpen owing to the increasing dominance of the gel (L_β) phase.

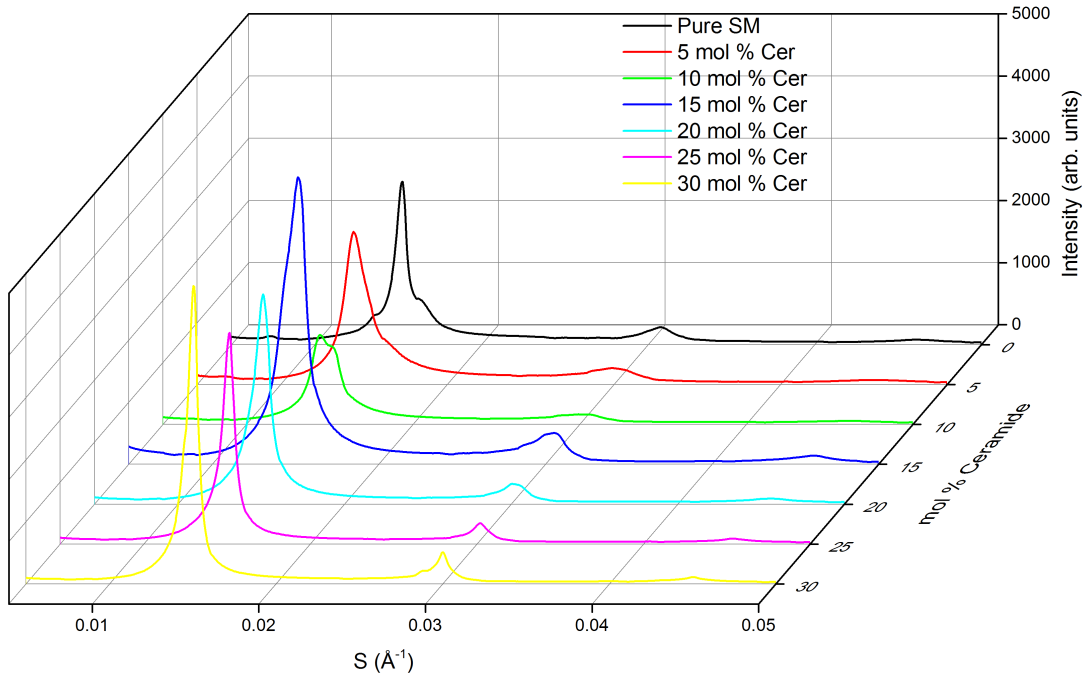

Figure 4.9: SAXS profiles of sphingomyelin with the addition of ceramide. The (0 1) ripple peak is not visible beyond 5 mol % ceramide, whilst there is a clear sharpening of the (1 0) and (2 0) gel peaks.

At 30 mol % ceramide, the ceramide-rich gel (L_{β}') phase gives rise to very strong reflections (see *figure 4.9*), with only a very weak shoulder from the sphingomyelin-rich (rippled) gel remaining. With a ratio of less than 1:2 molecules of ceramide:sphingomyelin globally, this observation demonstrates the tendency of ceramide to dominate resulting phase behavior and induce the formation of a gel phase that has melting transition far above physiological temperatures (> 60 °C as shown in both DSC and SAXS data given in *figures 4.5* and *4.6* respectively). It is therefore a possibility that the dramatic effect that relatively low concentrations of ceramide have on the biophysical properties of the membrane provide a biophysical mechanism through which ceramide can act as a signaling molecule.

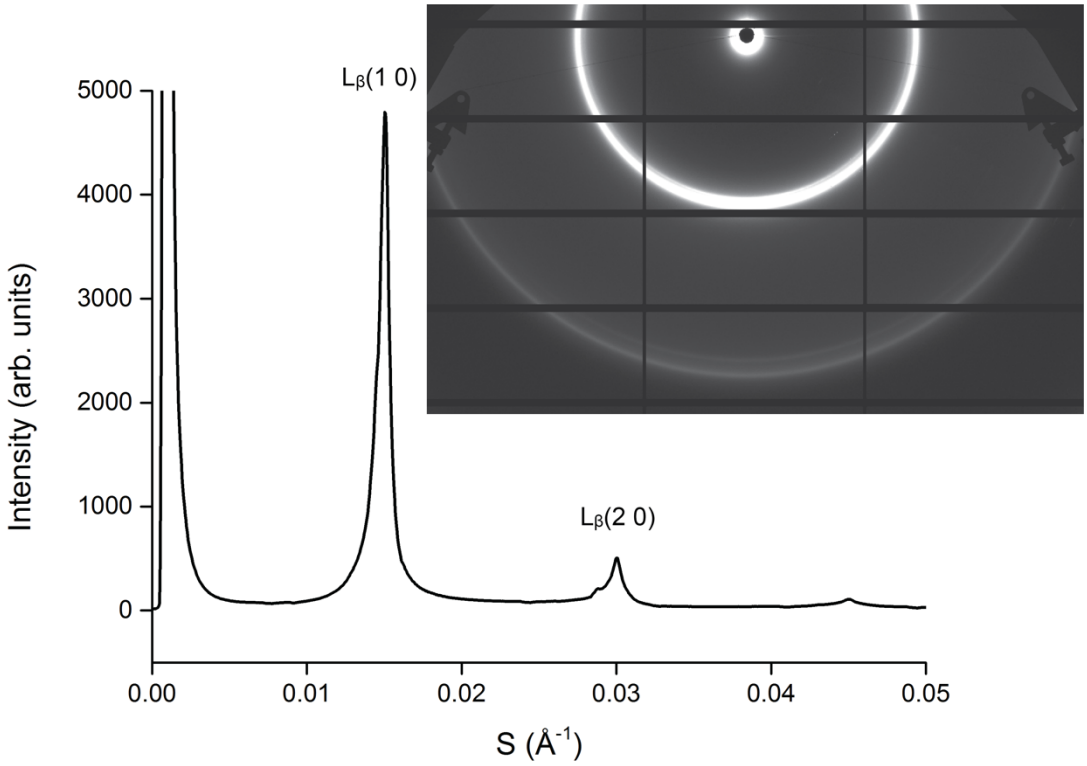

Figure 4.10: SAXS pattern for egg-yolk sphingomyelin doped with 30 mol % ceramide in excess water.

Despite the rapid loss of SAXS signal from the 0 1 ripple period peak with increasing concentrations of ceramide (as can be seen in the diffraction pattern shown in *figure 4.10*), it is anticipated that the ripple phase persists locally at concentrations beyond what can

be detected by SAXS; this is suggested by the gradual sharpening of the ceramide-rich gel (L_β) peaks on increasing the amount of ceramide dopant. In addition, the melting transition of the rippled gel (P'_β), as detected by DSC (shown in *figure 4.5*), is present up to concentrations of 20 mol % ceramide. As a result, other structural methods are required that can probe the model membrane locally as means of resolving the sphingomyelin ripple and detecting its disruption with the addition of a ceramide dopant.

4.1.2 AFM of sphingomyelin:ceramide mixtures as a means of resolving local membrane ripples

In contrast to SAXS (an ensemble technique by which the powder diffraction patterns result from reflections from a large number of repeating lattices), AFM provides a local view into the structure of model lipid bilayers, with the restriction that only topographic view of the surface can be observed. As a result, local structural features are revealed that often may be lost in ensemble techniques. As previously discussed, it is expected that the ripple phase is maintained beyond that observed by SAXS, and AFM is therefore used to locally probe how the disruption and loss of the ripple lattice occurs.

To preserve the ripple lattice in a supported lipid bilayer (i.e. so it is not constrained or 'flattened-out' by the supporting surface), previous AFM experiments have reported that secondary 'floating' supported lipid bilayers are necessary[134]. Imaging in tapping mode, where the AFM tip intermittently contacts the surface, allows for imaging of such secondary bilayers without sweeping them away with the AFM tip. In addition, if a larger secondary bilayer can be engineered, it will likely be more securely anchored in place owing to the increasing bilayer-bilayer van der Waals interactions, thus further enhancing the feasibility of imaging such delicate structures by AFM that are not covalently bound to the substrate. Such a secondary (and tertiary) supported lipid bilayer, composed of pure sphingomyelin, can be observed in figure 4.11 below.

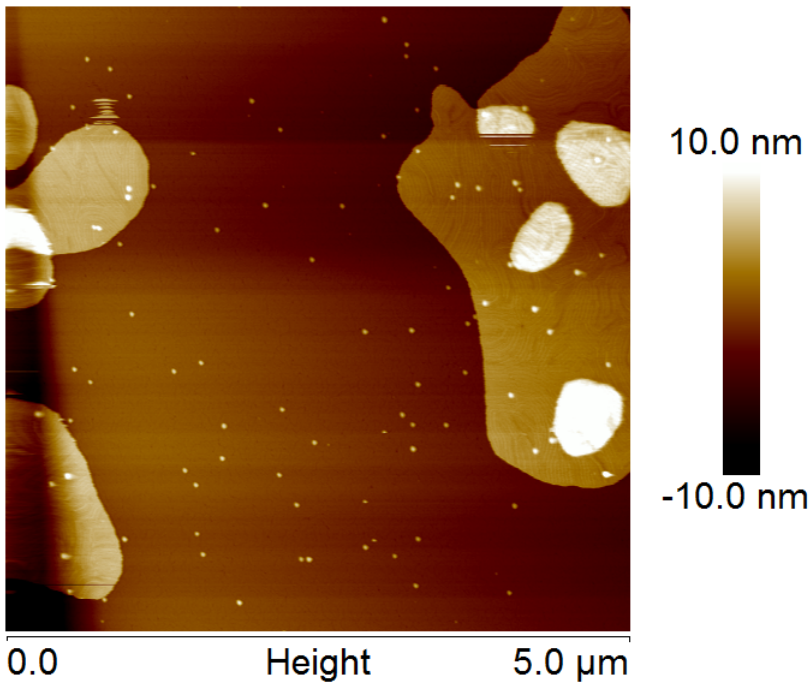

Figure 4.11: AFM image of a pure sphingomyelin 'floating' lipid bilayer. Three distinct levels can be observed corresponding to primary, secondary and tertiary bilayers above the supporting mica substrate. Characteristic ripple patterns can be observed on the secondary and tertiary bilayers, where they are not constrained by the solid support. The observed light dots are excess vesicles that have settled upon the surface during the prolonged incubation required for the formation of 'floating' bilayers.

It was found here that by allowing the supported bilayers time (ca. 4 h) to equilibrate in the presence of excess vesicles, and after incubation above the main transition temperature, a secondary supported lipid bilayer that conserved characteristic membrane ripples was formed. In quantifying the ripple period, the dimensions of the ripple lattice relative to that of the AFM probe must be considered; the nominal AFM tip radii of ca. 10 nm is of the same order of magnitude as the ripple period. Where the ripple period is at a minimum (i.e. for pure sphingomyelin, $b = 14$ *nm*, *figure 4.12*), an AFM tip with a low aspect ratio (i.e. a blunt tip) is unable to fully penetrate into the ripple and will thus give false (deflated) values for the ripple amplitude. Lateral measurements of the ripple period can be considered to be accurate, as a blunt tip will act to broaden the ripple but the peak-to-peak distance will remain the same. Finally, previous AFM studies of phosphocholine (PC) bilayers have demonstrated that two distinct ripple structures can be formed depending upon their thermal history[134]; a stable ripple (denoted $\Lambda/2$ where Λ is the ripple period) is formed upon heating above the

pretransition that has an asymmetric profile, whereas a metastable ripple (denoted Λ) is formed upon cooling from the fluid (L_α), with a periodicity that is approximately double that of the stable ripple and has a symmetric profile. The symmetric profile of the metastable ripple has a much greater (> factor of 5) ripple amplitude relative to the stable ripple, and is thus easily distinguishable by AFM.

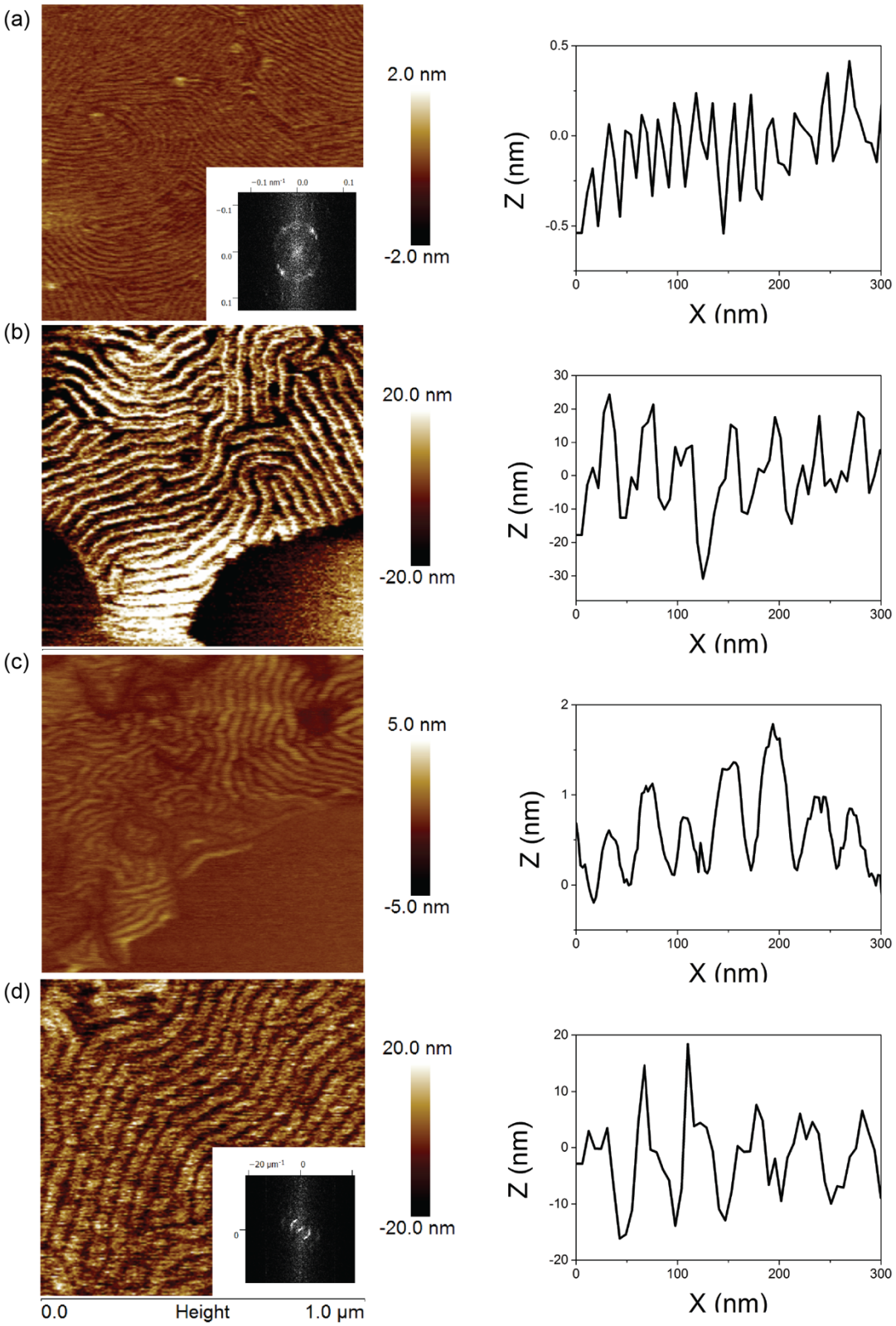

Figure 4.12: AFM height images of secondary supported lipid bilayers of sphingomyelin doped with (a) 0 mol % , (b) 15 mol %, (c) 20 mol % and (d) 25 mol % ceramide respectively. The characteristic ripple can be clearly observed in all images, with a notable increase in ripple period from ca. 17 nm for pure sphingomyelin shown in (a), to ca. 42 nm when doped with 20 mol %

ceramide shown in (c). Cross-sections through the ripple lattice are given for each composition along with insets showing the FFT for (a) and (d).

Images of the sphingomyelin ripple phase (as shown in *figure 4.12*) show a clear increase in the ripple period with increasing concentrations of ceramide, from ca. 17 nm for pure sphingomyelin (*figure 4.12* (*a*)) to ca. 42 nm when doped with 20 mol % ceramide (*figure 4.12* (*d*)). It must be noted that two distinct ripple amplitudes are observed, on the order of nm's (as seen in images *4.12 (a) and (c)*) and tens of nm's (images *4.12 (b) and (d)*), thus corresponding to the stable ($\Lambda/2$) and metastable ripple (Λ) ripple structures respectively. Despite the presence of two distinct ripple phases in the systems studied (that vary in their ripple periodicity by a factor of two), a clear trend can be observed in increasing periodicity upon increasing the concentration of ceramide dopant, which is further corroborated by the SAXS data discussed previously and shown in *figure 4.9*.

The ripple period can be quantified by either taking topographic cross-sections through the ripple lattice and measuring the peak-to-peak distance, or by taking the fast Fourier transform (FFT) of the image. The FFT produces an image in reciprocal space in which the intensity corresponds to frequency of that given image feature. For regular, repeating patterns (e.g. the topography of the ripple phase as visualized by AFM), spots arise in the FFT for which the intermediate distance in reciprocal space corresponds to the spacing of the image features in real space. This method of taking the FFT to extract values for the ripple period from AFM images can be readily applied when the images are of a single plane, with consistent contrast in the image between the peaks and troughs of the ripple. The ripple period(s) as determined by both SAXS and by AFM (from topographic cross-sections and FFT's respectively) for mixtures of sphingomyelin and ceramide are given in *table 4.2*. This combined data demonstrates how AFM can access local rippled structures that would be lost in ensemble SAXS experiments, and in addition it probes complimentary length scales from nm to μm and can thus quantify the ripple periodicity.

SM:Cer Composition (mol %)	Ripple Period (nm) - SAXS	Ripple Period (nm) – AFM topographic cross-section	Ripple Period (nm) – AFM FFT
100:0	13.7	ca. 19	18.7
95:5	15.4	-	-
85:15 (2Λ)	-	42	-
80:20	-	ca. 34	38.0
75:25 (2Λ)	-	52	-

Table 4.2: Ripple period for mixtures of sphingomyelin:ceramide as determined by SAXS and AFM respectively.

From the measurements of the ripple period of sphingomyelin:ceramide mixtures presented in table 4.2, it is clear that ceramide has a dramatic effect as it disrupts the ripple phase and drives the formation of a gel (L(β)). In light of proposed models for the ripple, in which it can be considered to effectively be composed of two distinct phases with contributions from both the *fluid* and *gel* to give the characteristic ripple, a likely mechanism of disruption of the rippled bilayer is by ceramide molecules adding to the *gel*-like region of the ripple and thus lengthening the ripple period. As pure egg-yolk ceramide is found exist in the *gel* (L_β) phase (as shown in the DSC trace given in *figure 4.5*), it can be expected to favor coexistence with the *gel*-like regions of the sphingomyelin ripple. A possible means of verifying this proposed mechanism of disruption is by contrasting the behavior of ceramide as a dopant with that of cholesterol; cholesterol drives the formation of liquid-ordered (L_O) phases and would thus disrupt the ripple phase by 'melting' it's *gel*-like regions, degrading the ripple without an accompanied elongation of it's periodicity.

4.3 Effect of cholesterol on the sphingomyelin ripple phase

Cholesterol is considered implicit to the formation of lipid rafts as it induces formation of the liquid-ordered phase in phospholipid and sphingolipid systems. The interplay of cholesterol with sphingomyelin has received considerable attention through the study of model membrane systems that mimic lipid rafts, in which sphingomyelin:cholesterol domains are formed amongst a phospholipid matrix[9]. Studies of binary

sphingomyelin:cholesterol systems are lacking[135], and the mechanism by which the sphingomyelin ripple phase is disrupted to give a liquid-ordered bilayer has not previously been a subject of biophysical investigation despite it's possible biological significance. In the context of this work, it provides an opportunity to contrast the effect of cholesterol as a dopant on the ripple phase with that of ceramide, which drive the formation of the liquid-ordered (L_O) and gel phases (L_β) respectively.

4.3.1 SAXS of sphingomyelin:cholesterol mixtures

Most recent SAXS studies of binary sphingomyelin:cholesterol mixtures have focused on the molecular complex that sphingomyelin forms with cholesterol, for which a ratio of 1.8:1 molecules of sphingomyelin:cholesterol (i.e. 36 mol % cholesterol) has been reported[124] as the point at which the binary sphingomyelin:cholesterol mixture gives rise to a single liquid-ordered phase. However, at lower concentrations of cholesterol, it is anticipated that the the ripple phase is conserved as the mixture tends towards the liquid-ordered phase. Indeed, at 30 mol % cholesterol (i.e. just below the single phase region), a clear splitting can be observed in the SAXS patterns owing to the coexistence of liquid-ordered (major component) and gel (minor component) regions, although reflections characteristic of the ripple phase are absent (*as shown in figure 4.13*).

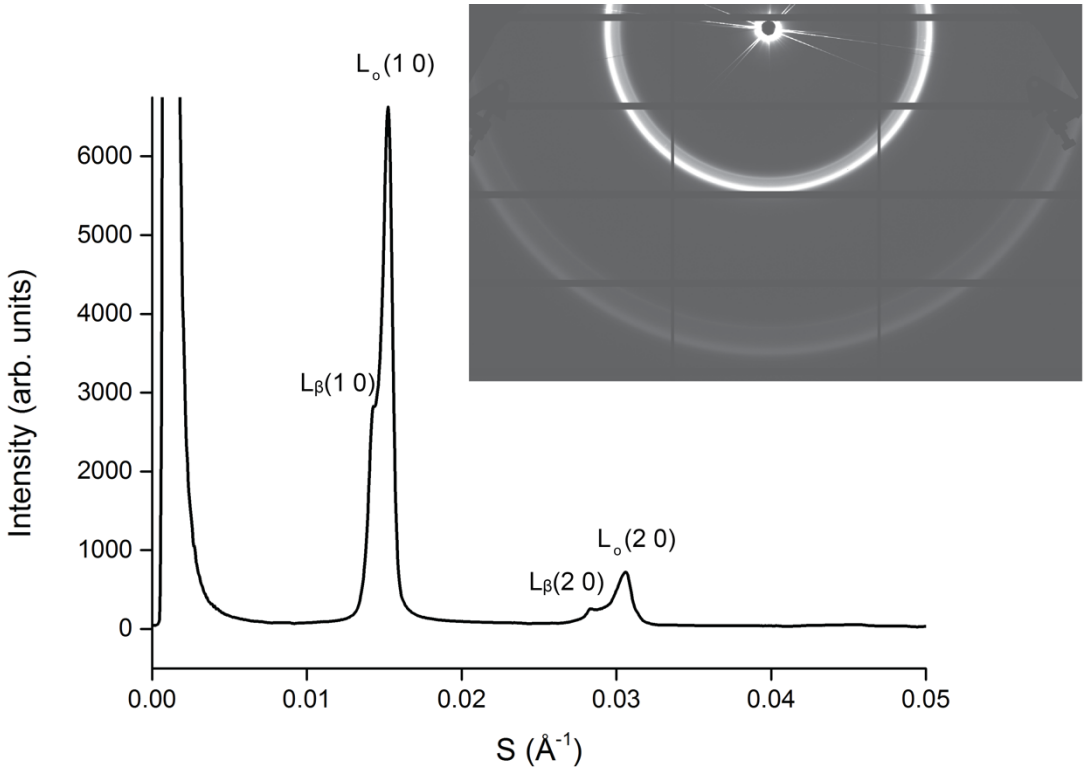

Figure 4.13: SAXS pattern for egg-yolk sphingomyelin doped with 30 mol % cholesterol in excess water. Clear splitting is observed owing to the coexistence of liquid-ordered ($\boldsymbol{L_O}$) and gel ($\boldsymbol{L_\beta}$) phases, with the thicker gel phase giving 1st and 2nd order reflections at low values of s.

At lower concentrations, characteristic reflections from the ripple phase are visible, and are enhanced by the presence of cholesterol. It is therefore possible to track the 0 1 peak (i.e. the ripple period) up to concentrations of 10 mol %, beyond what is attainable with equivalent concentrations of ceramide as a dopant (as shown in *figure 4.14*). The presence of cholesterol also leads to an increase in the ripple period, from 13.7 nm for pure sphingomyelin to 15.0 nm with 10 mol % cholesterol, but this increase is subtler than with that of ceramide as a dopant, for which the ripple period increases to 15.4 nm with only half the equivalent concentration of ceramide (5 mol %). This observation is consistent with the gradual 'melting' of the *gel*-like regions of the ripple upon the addition of cholesterol, with only a relatively small increase in ripple period. Between these two distinct regions (of pure sphingomyelin, for which there coexistence between a rippled (P'_β) and a flat (L_β) gel, and the SM:chol single phase liquid-ordered (L_O) region respectively), there are differing contributions from each of these distinct phases as the

mixture approaches the single phase liquid-ordered (L_o) region. The reflection from the flat L_β gel phase is diminished at concentrations of 10 mol % cholesterol, suggesting that cholesterol concurrently partitions to and 'melts' this L_β gel component in addition to its uptake by the ripple (P'_β) phase. Above concentrations of 10 mol % cholesterol, the liquid-ordered (L_o) phase becomes increasingly dominant, and it is not possible to resolve the 0 1 peak of the ripple (P'_β) phase. However, a clear trend in ripple period can be extracted from the SAXS data for which the periodicity increases by ca. 1 Å / mol % of cholesterol dopant.

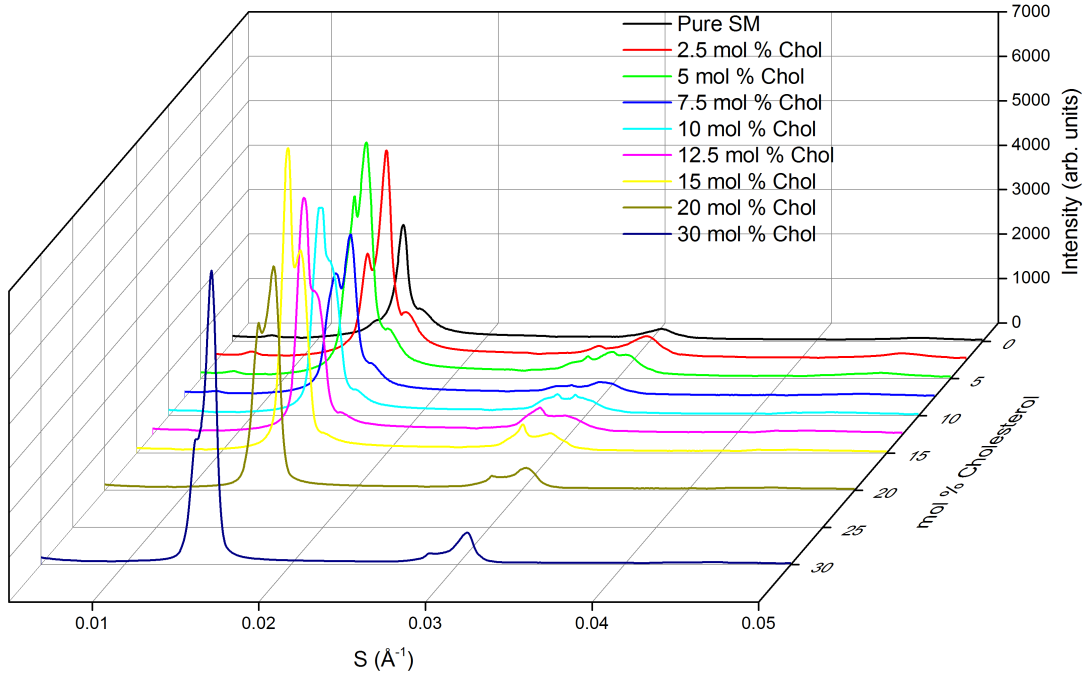

Figure 4.14: SAXS profiles of sphingomyelin with the addition of cholesterol. The 0 1 ripple peak at s = ca. 0.005 Å^{-1} is lost on increasing the concentration of cholesterol, with the emergence of sharp 1st and 2nd order peaks arising from the liquid-ordered phase.

As with mixtures of sphingomyelin and ceramide, AFM can be similarly applied to sphingomyelin:cholesterol systems in order to gain a local view of the phase behavior of the system. However, consistently higher resolution images are required in order to extract the ripple periodicity, as the ripple period(s) extracted from the SAXS data given in *figure 4.14* show a very gradual increase; a periodicity of ca. 14 nm must therefore be

routinely resolved in order to see such a trend by AFM. Images with such resolution have been attained for pure sphingomyelin (see *figure 4.12 (a)*), but to systematically attain such resolution of soft systems is non-trivial. At higher concentrations of cholesterol, coexistence of the liquid-ordered (L_o) and gel (L_β) phase would be expected to give rise to gel domains within a liquid-ordered matrix, where such domains can be visualized by AFM provided a height mismatch exists between the two.

4.3.2 AFM of sphingomyelin:cholesterol mixtures

Sphingomyelin:cholesterol domains, within a *liquid-disordered* (L_α) phospholipid matrix, have formed the basis of many AFM studies of phase separation in model membrane systems, although binary mixtures of sphingomyelin and cholesterol are often neglected as they do not represent a model that could more closely mimic the 'lipid-rafts' of cell membrane. However, the molecular interactions between sphingomyelin and cholesterol that collectively lead to liquid-ordered (L_o) domains are clearly important, and it is therefore of interest to study sphingomyelin ripple phase disruption by cholesterol with AFM.

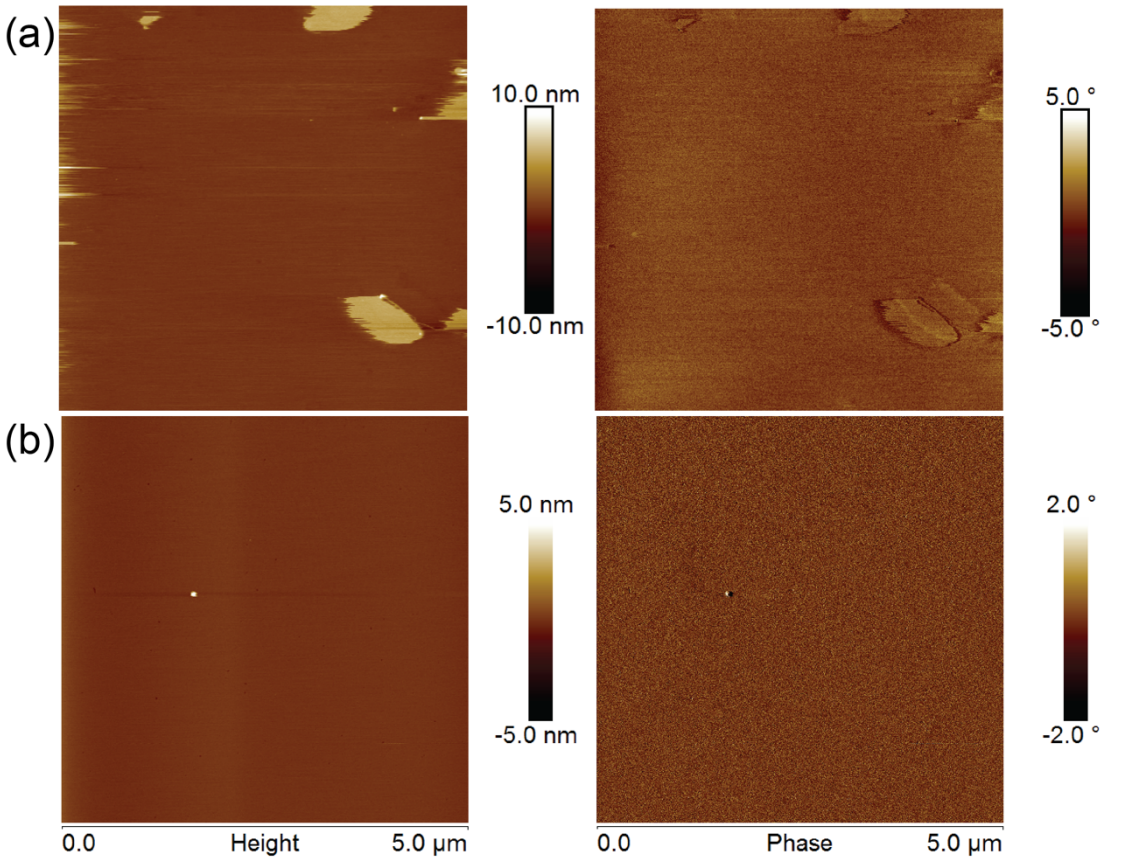

Figure 4.15: AFM height and phase images of (a) 90:10 mol % sphingomyelin:cholesterol and (b) 85:15 mol % sphingomyelin:cholesterol. Image (a) shows a planar supported bilayer upon which secondary bilayers are 'floating'; the streaking in the image is characteristic of a mobile domain which is being pushing around by the AFM tip. Image (b) shows a single planar supported bilayer; the small white dot is an excess vesicle adsorbed to the surface, and the phase image does not show any contrast that would suggest phase separation.

For the systems visualized by AFM, it was not possible to observe any rippling within the cholesterol doped bilayers. At 10 mol % cholesterol, *image 4.15 (a)* shows that floating bilayers were formed, with islands that are ca. 5 nm above the primary supported bilayer surface (i.e. consistent with the width of a secondary lipid bilayer). In addition, streaking appears in the image that is characteristic of a mobile entity, such as an area of bilayer that is only weakly bound to the underlying substrate. Any rippling within these floating bilayers was not detected, but it is not possible to say whether this is due to these secondary bilayers residing in the liquid-ordered (L_o) phase, or because the AFM tips used provided insufficient resolution to resolve the ripple. At 15 mol % cholesterol, single supported bilayers are formed with no indication of either the ripple phase or of

lateral phase separation, despite SAXS data revealing that there is phase coexistence for such compositions (as shown in *figure 4.14*). As a result, measurements of the sphingomyelin ripple period and its disruption by a cholesterol dopant must be taken from the ensemble SAXS patterns shown in *figure 4.14*, and cannot be consolidated or extended with local AFM imaging. The increased stability of secondary supported sphingomyelin lipid bilayers doped with ceramide, relative to those doped with cholesterol, is likely due to the differing chemistries of their respective headgroup entities. Cholesterol, with a single hydroxyl group, can only donate a hydrogen bond, whereas ceramide can both accept and donate a hydrogen bond via it's carbonyl and amine and hydroxyl groups respectively. This can plausibly act to increase the strength of interaction between opposing lamellar layers and thus stabilizes a secondary supported bilayer.

4.3.3 Cholesterol vs. ceramide as a dopant in the sphingomyelin ripple phase

The clear difference in the effect on ripple periodicity with increasing amounts of dopant (as depicted in *figure 4.16*) suggests that the disruption of the ripple phase occurs via a different mechanism for cholesterol and ceramide respectively. Cholesterol gives rise to a very gradual increase in ripple period of ca. 1 Å/mol % dopant, with a complete disappearance of the the ripple phase beyond concentrations of 10 mol % (as far as can be detected by both SAXS and AFM). Conversely, the addition of ceramide as a dopant leads to an increase of ca. 5 Å/mol % in ripple periodicity, with AFM images showing that the ripple phase persists locally at concentrations up to 20 mol %, for the which the ripple period is over 40 nm; a 3-fold increase on that of pure sphingomyelin.

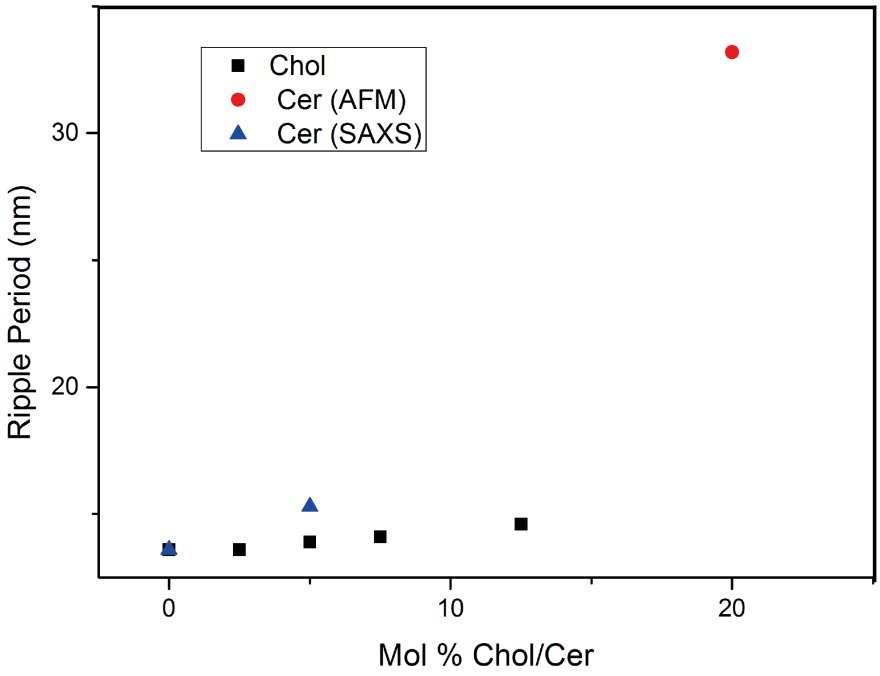

Figure 4.16: Effect of concentration of cholesterol and ceramide dopant respectively on the ripple period (Λ) as extracted from both SAXS and AFM data. AFM provides data beyond that attainable with SAXS, owing to the larger lattice parameters and loss of signal from the ripple as disruption to the repeating occurs upon the addition of ceramide. The differing effects on the ripple period on doping sphingomyelin with ceramide and cholesterol respectively suggest different mechanisms of ripple disruption; cholesterol is proposed to 'melt' the gel-like regions of the ripple whereas ceramide is proposed to add to them.

These differing behaviors in the mechanism of ripple phase disruption result from the physicochemical properties of the respective dopants and their molecular interactions with sphingomyelin in the ripple phase. It is proposed that cholesterol acts to 'melt' the gel region of the ripple as it drives the formation of the liquid-ordered (L_o) phase; this is accompanied by only a slight increase in periodicity before the ripple is lost. In contrast, ceramide is proposed to add to the gel regions of the ripple, and thus extending it's periodicity, as it drives the formation of the gel (L_β) phase. These contrasting mechanisms of ripple phase disruption are outlined in the schematic in *figure 4.17*.

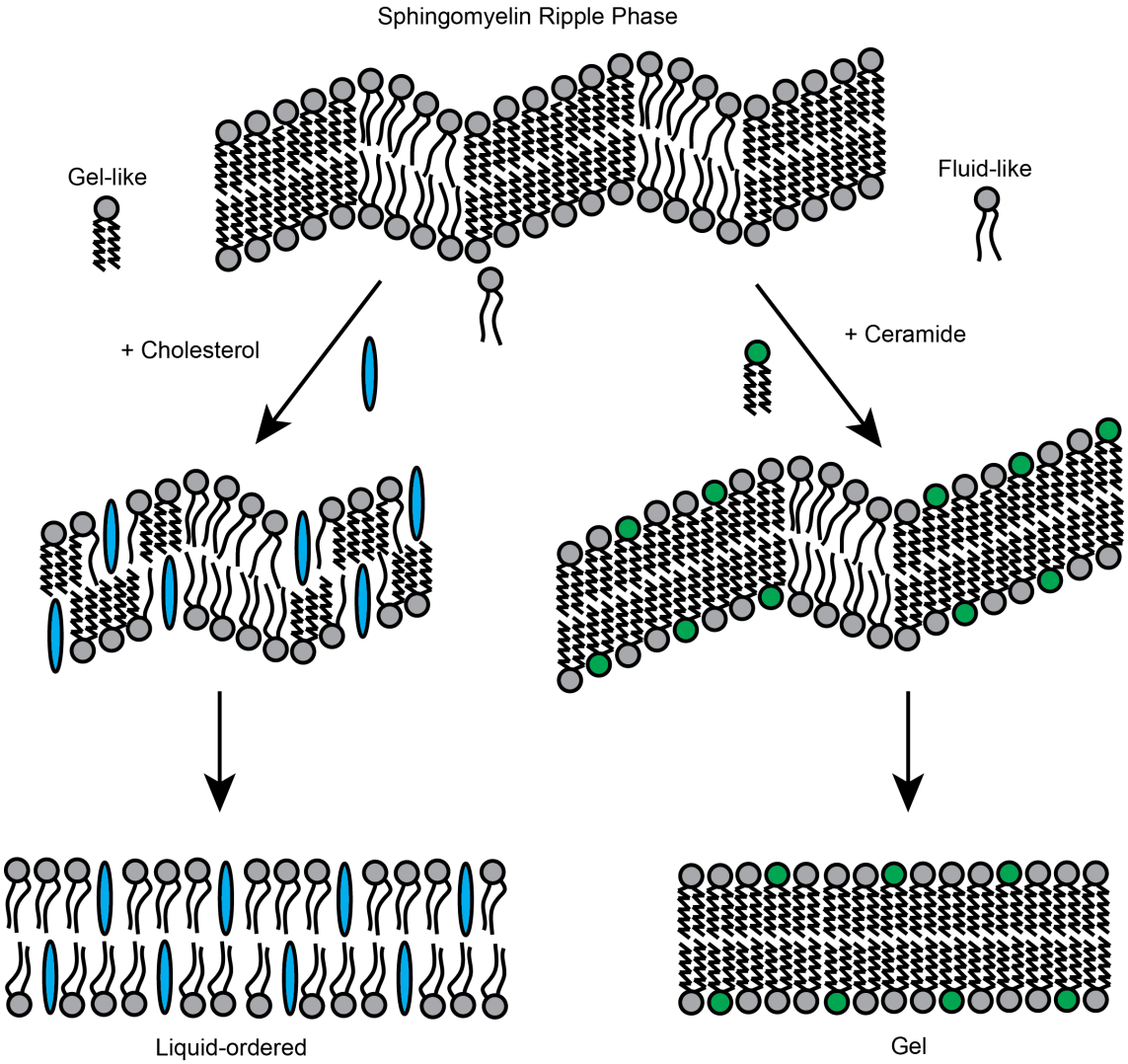

Figure 4.17: Schematic of proposed mechanisms of disruption. Cholesterol 'melts' the gel-like regions of the ripple as it drives the formation of the liquid-ordered phase with little increase in ripple periodicity. Ceramide adds the the *gel-like* region of the sphingomyelin ripple, resulting in an associated increase in ripple periodicity.

4.4 Conclusions

Disruption of the sphingomyelin ripple phase, with a demonstrable increase in the ripple period, is shown here to have a significant dependence of the nature of the dopant. It is proposed that a dopant that drives the formation of the gel (L_β) phase (i.e. ceramide in this instance) extends the ripple periodicity by adding to the gel-like regions of the ripple. In contrast, a dopant that drives the formation of the liquid-ordered (L_o) phase (i.e. cholesterol) does so by 'melting' these gel-like regions, without a significant increase in the ripple period. As ceramide and cholesterol play important biological roles *in vivo*,

as a signaling molecule in apoptosis and as an integral component of lipid rafts respectively, their physicochemical properties are often cited to underpin their mechanism of action. The work presented here shows how they interact specifically with sphingomyelin, whereby ceramide acts to promote sphingomyelin's propensity to reside in the gel phase, which in a biological context would inhibit the function of membrane components by freezing them in place. In contrast, cholesterol promotes compartmentalisation *via* liquid-liquid phase separation within the membrane, thus focusing bioactivity; on a local level, it is shown here that this can be achieved by 'melting' the gel regions of the sphingomyelin ripple phase.

To further consolidate this proposed mechanism of disruption it is likely that stronger SAXS reflections would be obtained for an aligned ripple structure (which could be engineered either by shear or by depositing a bulk lipid film upon a given surface); this could provide a means of resolving the ripple period at dopant concentrations beyond what is reported here, and could in turn give an insight into the packing of the hydrocarbon chains as revealed by the wide-angle region of the scattering pattern. Similarly, advanced AFM methodologies (e.g. peak force tapping, in which the force between the tip and the sample is finely controlled) could yield more routine high-resolution images of these delicate 'floating' bilayer structures. The AFM studies presented here would be greatly enhanced by temperature control, facilitating control over whether the stable ($\Lambda/2$) or metastable (Λ) ripple is formed. Overall, both real-space (i.e. AFM) and reciprocal space (i.e. SAXS) methodologies are likely required in order to gain the most complete picture of sphingomyelin ripple phase disruption, as is demonstrated in this study.

Chapter 5: Imaging the surface structure of inverse lipid phases

Liquid crystalline meso-phases can form spontaneously when amphiphilic lipids are mixed with water under suitable conditions, and give rise to a plethora of curved nanostructures in which contact between water and the lipid hydrocarbon tail is avoided and the packing of the individual lipid molecules is optimised[34]. These assemblies are vital in nature and have found applications in a wide range of areas from material templating[136] for high surface area catalysts to vehicles for drug delivery and membrane protein crystallization[137]. While their bulk structure has been investigated extensively (often by small angle X-ray scattering[39]), their surface structure has received little attention[138]. A knowledge of the surface structure is important in many applications because the way self-assembled lipid structures terminate determines how they interface with their surrounding environment. Specifically, significant questions remain as to whether the water channels of bicontinuous cubic phases are open to the bulk. In addition, dislocations, defects and grain boundaries cannot be observed in bulk measurements that are averaged over many randomly oriented domains, but are likely to impact upon their technological applications. The 'soft' nature of these lyotropic lipid phases makes high resolution AFM technically challenging[138,139], and is further hindered by the unknown alignment of the structure on the substrate, although GI-SAXS would allow for full 3D characterization of the thin lipid film[6].

Inverse lipid phases result when there is an interfacial curvature towards the aqueous region[1], and fall into two main categories; bicontinuous cubic and inverse micellar. The bicontinuous cubic phases[140] (space groups Pn3m, Im3m and Ia3d) are comprised of a complex nanostructure in which a lipid bilayer is draped over an infinitely periodic minimal surface, resulting in two interconnecting water channels which never meet. The inverse micellar cubic phases[34,141] are formed of close packing of micelles with a water core, of which the Fd3m space group is the most ubiquitous[29]. In addition, a micellar 3D hexagonal phase has been identified with space group $P6_3/mmc$[35], and the most studied 2D hexagonal phase[32] is formed with point group p6mm. The unit cells of these

structures are shown in *figure 5.1* below; it is possible to envisage the plethora of Millar planes through which the inverse structure terminates and which can be imaged AFM. (N.B. – *The accompanying simulated projections*[142] *of the 1 1 0 and 1 1 1 face of the* P_n3_m *inverse phase are given in figure 5.5*) .

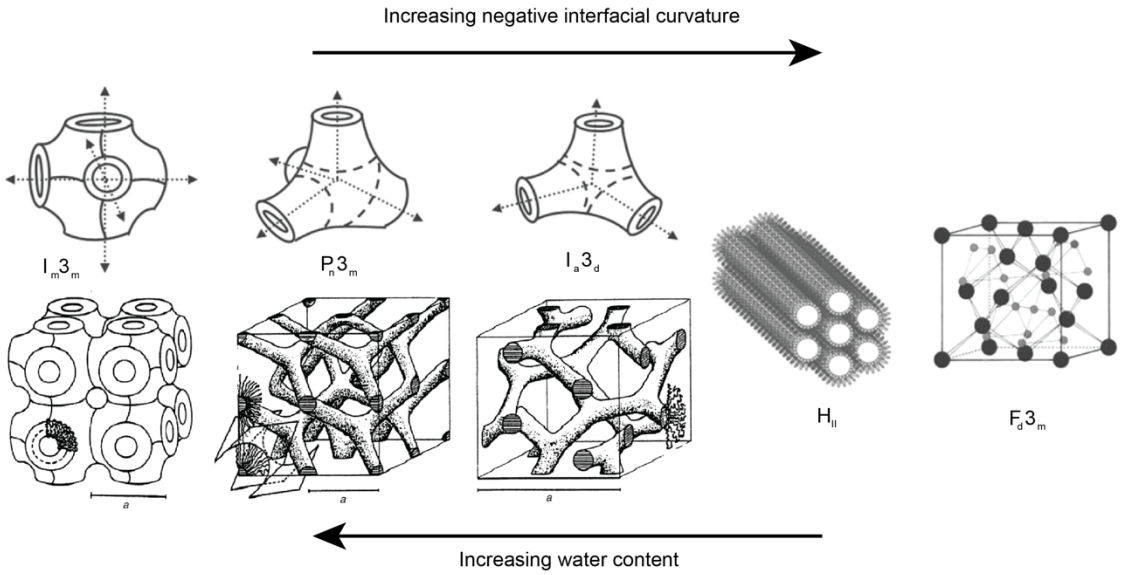

Figure 5.1: Schematic showing examples of the inverse lipid phases for which an understanding of their terminating interfacial structure is lacking. Increasing negative interfacial curvature is generally accompanied by a decrease in the volume of water that can be accommodated. *Figure adapted from:* J.M. Seddon *et* al, Physical Chemistry Chemical Physics 2, 4485–4493 (2000); C.V. Kulkarni *et al*., Phys Chem Chem Phys 13, 3004–3021 (2011).

Despite extensive studies of their bulk structure and properties (largely by SAXS), very little is known about their surface structure owing to the lack of techniques that can access nm resolution of a soft sample in an aqueous environment and at physiological temperatures. Most recently, efforts have been made to visualize the surface structure of 'cubosomes' using cryo-electron tomography[143], albeit in the presence of an amphiphillic block copolymer that is thought to stabilise the cubosome interface. AFM is the obvious choice for such surface studies, and previous work has shown that resolving the surface structure of inverse lipid phases is possible[4] (Fig.1) but a bottleneck remains as to how the lipid film is aligned on the surface. The feasibility of obtaining Bragg peaks from GI-SAXS of similar samples has been demonstrated[6], potentially allowing for interpretation of AFM images to be unambiguously interpreted with a prior knowledge of the

alignment of the inverse cubic phase. Recently, a synchrotron beamline combining *in situ* AFM capabilities with GI-SAXS came online at the European Synchrotron Radiation Facility[144]. The resolving power of SAXS coupled with the spatial capabilities of AFM could therefore provide an opportunity to simultaneously resolve both the bulk and surface structures of hydrated inverse lipid films *in-situ*. With this future direction in mind, this chapter reports on the formation of surface supported inverse lipid films, with AFM providing an initial view of surface structures of a range of inverse lipid phases (as determined by the lipid composition of the hydrated film). The resolving power of AFM in imaging such systems is verified with the bicontinuous cubic phase of monoolein.

5.1 Imaging the surface structure of moloolein in excess water

Monoolein is the most ubiquitous of the (synthetic) bicontinuous cubic phase forming lipids, having been the subject of both fundamental research into its phase behavior (largely by SAXS[30]) and of its biotechnological applications (membrane protein crystallization[137], drug delivery systems[145] etc.). As structural studies of the phases adopted by monoolein have largely focused on the bulk using ensemble techniques (i.e. SAXS), the interface which terminates the bicontinuous cubic structure as it meets the bulk aqueous phase has been neglected, . Understanding the structure of this specific monoolein-water interface is essential to gaining an informed view of, for example, how the growth of *in cubo* membrane protein crystals propagates (as monoolein is often utilized as the lipid matrix in membrane protein crytallisation), and how content is released from *cubosome* drug delivery systems. This interface, and the way in which the cubic structure terminates at the surface, will dictate whether one, both or neither of the water channels are open to the bulk. Such knowledge would therefore provide a platform for informed engineering of such drug delivery systems. An initial AFM study of monoolein films has proven the viability of imaging these delicate structures[138], albeit with a dearth of imaging data (the images given correspond to a single crystal plane (111), and contain ambiguity as to whether the water channels are 'capped' or open to the bulk). To build upon these studies, they must first be reproduced.

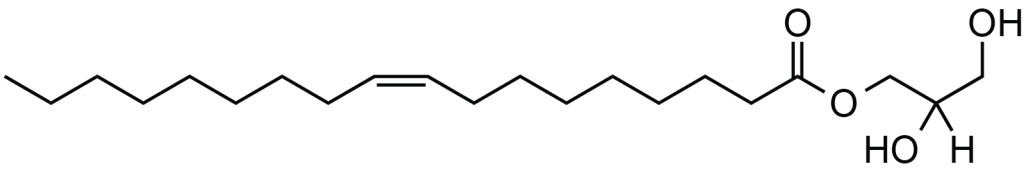

Figure 5.2: Chemical structure of monoolein (1-oleoyl-rac-glycerol).

Despite its relatively simple chemical structure in which a single monounsaturasted c-18 hydrocarbon chain is attached to a glycerol headgroup *via* an ester linkage, monoolein is rich in its lyotropic phase behavior which must be considered. As initial AFM experiments are conducted at room temperature with little control over their level of hydration (i.e. the thin film in air is taken as being dehydrated; the lipid film as imaged in the AFM liquid cell is taken as being in excess water), the thin film is placed in the P_n3_m region of the monoolein phase diagram[30]. A knowledge of the faces of this P_n3_m bicontinuous cubic structure are therefore essential in interpreting imaging data, as shown in *figure 5.5*.

5.1.1 HOPG as a supporting surface

As AFM imaging of inverse lipid films is a relatively unexplored area, it is essential to have a view of the underlying substrate so as to be able to distinguish between areas occupied by the lipid film and areas of exposed HOPG, thus gaining a knowledge of when it is futile to pursue imaging at smaller length scales (as high resolution images of HOPG are not required and are not the focus of this research). In addition, the surface structure adopts a hexagonal lattice both for HOPG (i.e. graphite) and for the (111) face of monoolein, albeit with a lattice parameter that is over an order of magnitude higher for the 111 face of the monoolein P_n3_m cubic phase, and therefore care must be taken to avoid false assignment of the phase of inverse lipid film. Imaging HOPG as a control under water therefore allows for simple discrimination between the lipid film and its underlying substrate.

Highly oriented pyrolitic graphite (HOPG) allows for the simple preparation of an atomically smooth and hydrophobic substrate, by which the uppermost layer(s) can be peeled away to expose a clean surface that is ideally suited to AFM imaging. In the case of imaging inverse lipid films, the use of a hydrophobic surface is important (c.f. mica);

after the deposition of the lipid film and subsequent hydration to give the inverse phase, it would be energetically unfavorable for the film to be displaced into the aqueous bulk as a hydrophobic surface would have to be exposed to water. Thus, by controlling the surface chemistry of the underlying surface (i.e. by ensuring that it is hydrophobic), it is possible to effectively anchor the deposited film in place when exposed to an aqueous environment, with HOPG providing a simple means of meeting these criteria.

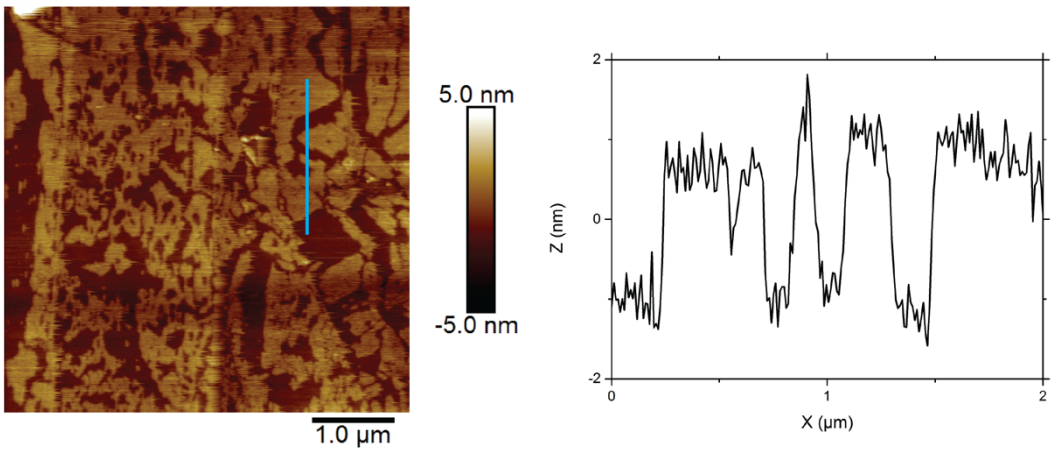

Figure 5.3: Tapping mode AFM image of the supporting substrate, HOPG, in water. The blue line through the image corresponds to the cross-section through this plane, shown on the right.

Images of HOPG were acquired in tapping mode under water (as shown in *figure 5.3*). As expected, discrete graphite layers can be observed that are ca. 1 nm thick, with the images showing sufficient features to be distinguishable from those upon which a lipid film has been deposited. The morphology is however atypical to what would be expected from HOPG, suggesting that contamination may have been present when imaging the bare HOPG substrate *in water*. It is plausible that an adsorbed contaminant lipid monolayer could give rise to the image features observed.

5.1.2 The (110) and (111) faces of MO by AFM

As the preferential alignment of the cubic phase upon a hydrophobic substrate is unknown, and in addition to the number of Miller planes through which the structure can be cleaved to expose the surface, it is difficult to predict an expected surface structure. From examining the SAXS data from bulk, hydrated monoolein samples, it can be envisaged that the peaks with the highest relative intensities (which correspond to reflections from their respective Miller plane) represent areas of higher electron

density, and could therefore likely correspond to the planes that support the surface structure. By taking sections through these planes, the expected surface structure(s) can be visualized prior to AFM imaging.

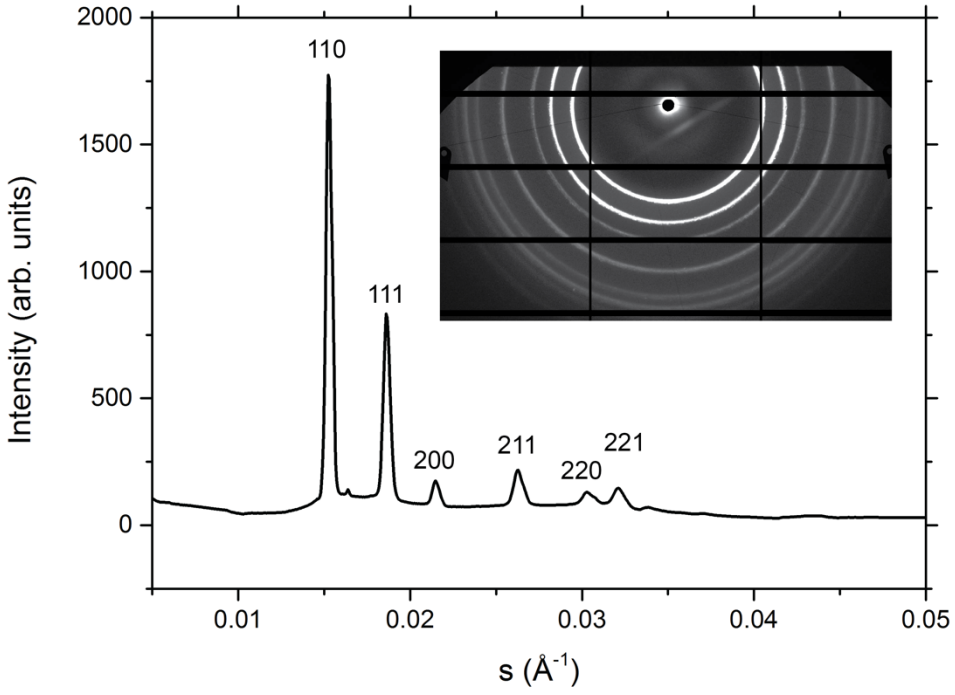

Figure 5.4: SAXS powder diffraction pattern of the $\boldsymbol{P_n3_m}$ bicontinuous cubic phase formed by monoolein in excess water.

The relative intensities of the 110 and 111 reflections from the powder diffraction patterns for monoolein in excess water (as shown in *figure 5.4* above) are far greater than those for subsequent allowed Miller indices, and we can therefore reasonably expect the surface to terminate along this plane at a greater frequency than for the subsequent reflections. Simulations of these planes through the lipid cubic phases have been reported in the literature, for which they are used as an aid in interpreting images acquired during electron microscopy of the endoplasmic reticulum[142] (as shown in *figure 5.5*). It is therefore possible to use these simulated images to inform the interpretation of equivalent AFM data sets.

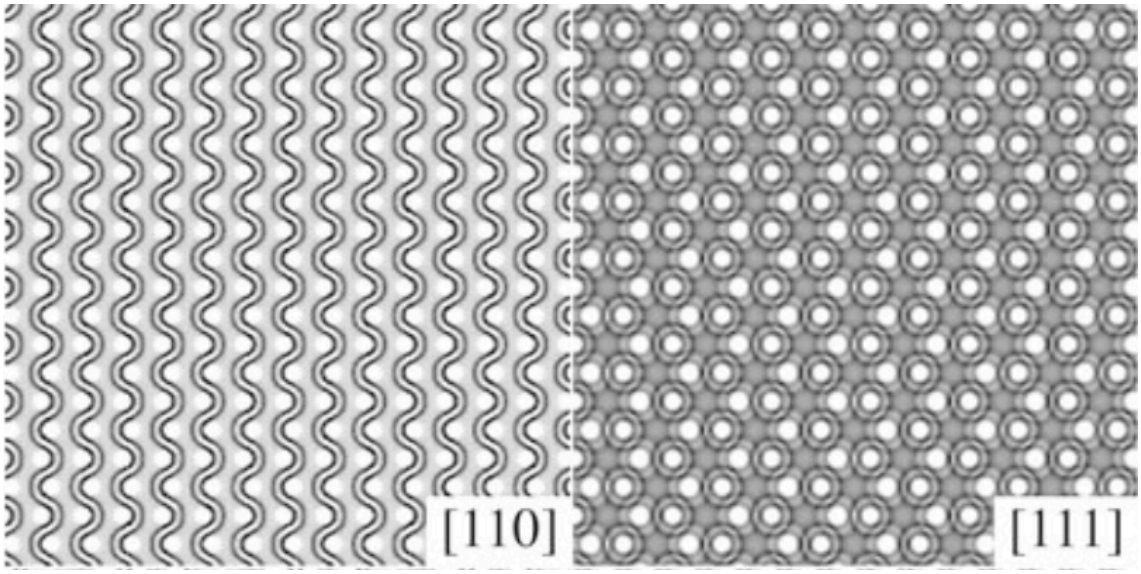

Figure 5.5: Simulated 2D projections of the 110 and 111 faces of the $\boldsymbol{P_n3_m}$ bicontinuous cubic phase, which correspond to the two most intense Bragg peaks in the scattering patterns for the bulk, hydrated monoolein. *Figure adapted from*: Z.A Almsherq *et al*.,. J. Cell Biol. 173, 839–844 (2006).

In order to form an interface of the monoolein bicontinuous cubic phase with the bulk water, a thin lipid film (ca. 500 nm thick) is deposited on the clean HOPG substrate by spin coating, with the emergence of Newton fringes that are characteristic of a sub-micron surface layer. Subsequent hydration of the film leads to the formation of the cubic phase as water channels penetrate into the bulk of the lipid layer. The interfacial cubic lattice can then be imaged with AFM provided that: (i) the tip is sufficiently sharp to resolve the cubic structure with a lattice parameter, *a*, of 9.7 nm, and (ii) the AFM can be operated with (low) tip-sample forces such that the delicate sample is not destroyed by the imaging process. AFM probes with a nominal tip radius of < 10 nm are available commercially (with trial-and-error leading to successful imaging with a sufficiently sharp probe), and tapping-mode AFM allows for the soft lyrotropic structure to be imaged in an aqueous environment (*n.b.* more sensitive AFM techniques are possible; operating in frequency modulation[146] and force feedback[79] modes, albeit not available *in-house*).

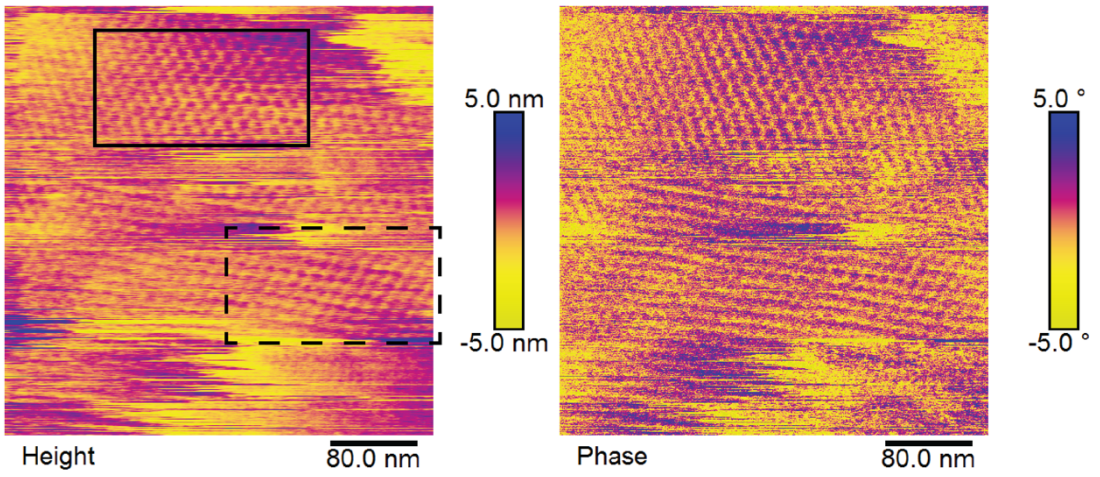

Figure 5.6: Tapping-mode height and phase images of hydrated monoolein on HOPG. Two distinct surface structures can be observed; the area highlighted in the solid line shows a hexagonal rhombic lattice that corresponds to the 111 plane, whereas the area highlighted in the dashed line shows an oblique lattice characteristic of the 110 plane.

The AFM images shown in *figure 5.6* confirm the feasibility of imaging the surface structure of the P_n3_m bicontinuous cubic phase in hydrated monoolein. Two distinct regions can be observed in the height (and corresponding phase) image(s) shown; a hexagonal (rhombic) lattice can be observed which corresponds to the 111 plane, as is shown in the simulated 2d projections shown in *figure 5.5*. This hexagonal lattice coexists with an oblique lattice that correlates to the 110 plane (i.e. the planes with the most intense Bragg peaks in bulk scattering experiments are observed in the terminating surface structure). The height image shows a protruding hexagonal lattice for the 111 plane, suggesting that this outermost network of water channels is 'capped' and thus separate from the bulk. The 110 plane can be similarly interpreted, with a protruding oblique lattice. To further characterize the surface structure, the lattice parameter, a, can be extracted from both the real space image, and from the fast-Fourier transform, provided that high resolution images can be acquired. For the images presented here, resolution is insufficient to extract a meaningful lattice parameter, but it is clear that it is of the order of 10 nm and in crude agreement with SAXS measurements[147].

It must be noted that such interpretations must be verified, likely using complimentary techniques such as SAXS. Introducing contrast between the two distinct water channels with the presence of heavy ions would allow for discrimination by SAXS; if both

channels are open to the bulk, the presence of heavy ions will introduce no contrast between the distinct water channels and the scattering pattern will remain unchanged, whereas if one channel is open there will be uptake of heavy ions, thus changing the symmetry of the system and the resulting scattering pattern. Nanomechanical mapping[79] may provide further evidence in evaluating whether the water channels are open to the bulk, with open channels appearing 'softer' than their capped counterparts.

5.1.2 OTS treated glass as a supporting surface

HOPG provides a hydrophobic substrate with areas that are atomically smooth locally, but the presence of multiple graphite layers results in a surface that contains steps between layers that are easily visible on the sub-micron scale (as shown in *figure 5.3*). This results in a surface with a distribution of distinct heights (albeit with angstrom surface roughness locally). It is therefore a possibility that the lipid film that is deposited on the supporting HOPG substrate is less well defined owing to the heterogenous interface between the film and the underlying surface. An alternative method of forming a smooth hydrophobic substrate is to render a smooth hydrophilic substrate (such as glass or mica) hydrophobic with the deposition of surface monolayer; silanization of a glass substrate with octadecyltrichlorosilane results in such a surface that is commonly used to meet this criteria[148]. The resulting surface can by easily cleaned prior to deposition of a lipid film by sonication in isopropyl alcohol (as shown in *figure 5.7*); AFM imaging under water reveals a substrate that has a r.m.s. roughness on the order of 1 nm, with local clusters that protrude ca. 3 nm above the surface. To verify the hydrophobicity of the OTS-treated glass, a drop of water placed on the surface has a contact angle > 90 ° (as observed; image not recorded); in contrast, there is significant wetting of an untreated glass surface, with a contact angle significantly less than 90 °.

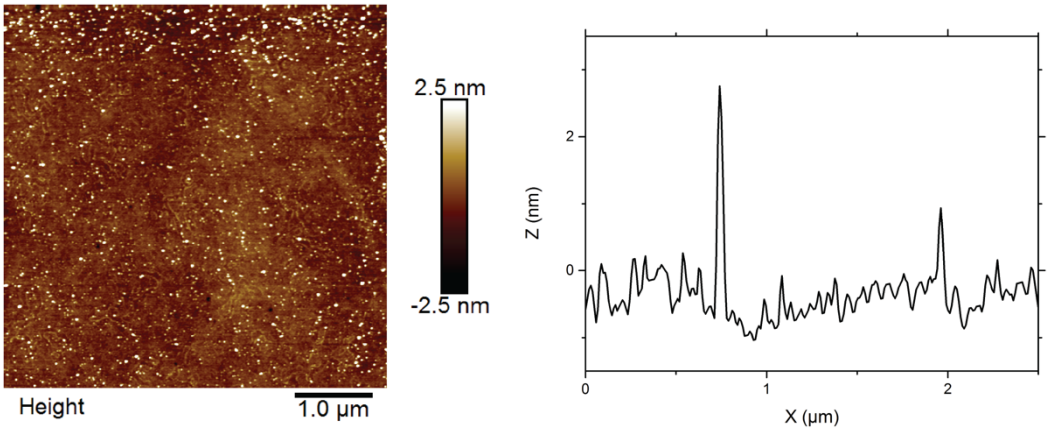

Figure 5.7: OTS treated glass to give a hydrophobic substrate; cleaned by sonication in isopropyl alcohol prior to imaging by AFM under water.

Upon depositing and hydrating thin films of monoolein on OTS treated glass, AFM of these lipid films did not yield any images characteristic of the monoolein lattice (as shown in *figure 5.8*). The textured surface suggests that the deposited lipid film remains anchored to the OTS-treated glass after hydration, but a repeating lattice is not observed and it is not thought that this is due to an insufficiently sharp tip; this specific experiment was repeated multiple times (n = 3) with fresh probes and images taken at random points on the surface. It is possible that the film was not allowed to reach full hydration in order to yield the bicontintinuous cubic phase, but this remains unlikely as this did not occur when using the same protocols but with HOPG as a substrate. Similarly, spin coating of the lipid film should in principle be a robust step in forming a supported bicontinuous cubic phase, provided the film is thick enough to accommodate multiple unit cells (and the emergence of Newton fringes indicate that it is). In summary, further work is required in establishing OTS treated glass as a suitable substrate *in-house*.

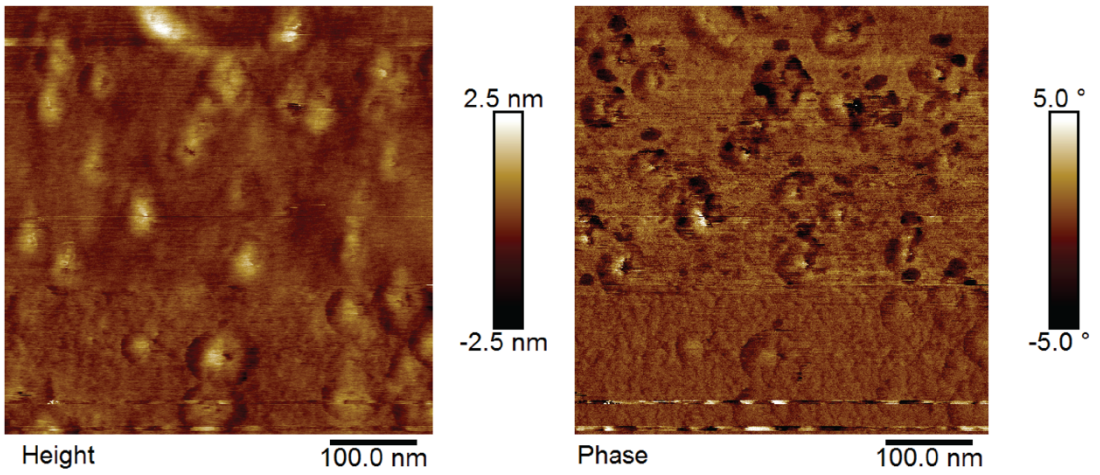

Figure 5.8: Height and phase images of thin films of monoolein deposited on OTS treated glass. Despite the presence of surface features that indicate the successful deposition of a thin lipid film, a characteristic cubic lattice cannot be observed.

5.2 Increasing the lattice parameter as a means of visualizing lipid cubic phases by AFM

In order to routinely image the surface of such soft matter structures with visualization of the terminating lattice (with a lattice parameter in the order of 10 nm), high-resolution liquid AFM is required. To increase the relative success rate of these imaging procedures, advanced AFM methodologies can be utilized such a peak-force tapping[79], in which fine control of the forces between the AFM tip and the sample can be achieved, allowing damage to the sample and the dulling of the tip to be averted. In addition, ultra-sharp AFM tips are available commercially with nominal tip radii of < 10 nm, with state-of-the-art carbon nanotube probes remaining an enticing option[149], although it remains to be seen whether an ultra-sharp tip would in fact be detrimental in imaging bicontinuous cubic structures by puncturing the membrane surface. Conversely, engineering the lipid cubic phases towards higher lattice parameters (i.e. by swelling the structure with an increased aqueous volume), would allow for the terminating structure to be resolved without the requirement for such high-resolution AFM; open questions of whether the water channels remain open to the bulk, and by which lattice plane the structure preferentially aligns, would remain valid albeit with larger lattice parameters.

Increasing the viability of AFM experiments does not represent the main motivation behind engineering swollen cubic phases, as such structures have important and timely

applications in the crystallization of large membrane proteins[137], but could provide a means of collecting images of their surface structure (which would in turn inform our ability to control the crystallization of these phases). In addition, the large lattice parameters of these swollen cubic phases (ca. 400 Å) are inaccessible to *in-house* scattering experiments as long flight tubes (of ca. 6 m) are required; AFM experiments are ideally suited to these length scales and could therefore open up such studies without the need for external (synchrotron) facilities.

5.2.1 Electrostatic swelling of lipid cubic phases

Theoretical predictions have reported that thermal fluctuations of the order of kT would act to destroy a bicontinuous cubic structure with a lattice parameter greater than 300 Å[150]. Doping the lipid lattice that supports the cupid phase with cholesterol will likely stiffen the cubic structure with the induction of a *pseudo* liquid-ordered (L_o) phase within the plane of the bilayer membrane, thus suppressing any fluctuations that would threaten the integrity of the cubic structure. In addition, the presence of cholesterol will act to stiffen the membrane, and could thus be beneficial to AFM visualization by supporting higher tip-sample forces during the imaging process. The introduction of a secondary lipid dopant that harbors a charged headgroup would lead to electrostatic repulsions, and result in swollen structure with an increased lattice parameter that is stabilized by the presence of cholesterol. By surveying an area of compositional space of mixtures of monoolein doped with both cholesterol and a phospholipid containing a charged lipid headgroup (DOPG and DOPS respectively), it is possible to identify compositions in which the lattice parameters are swollen far beyond the 300 Å predicted[39].

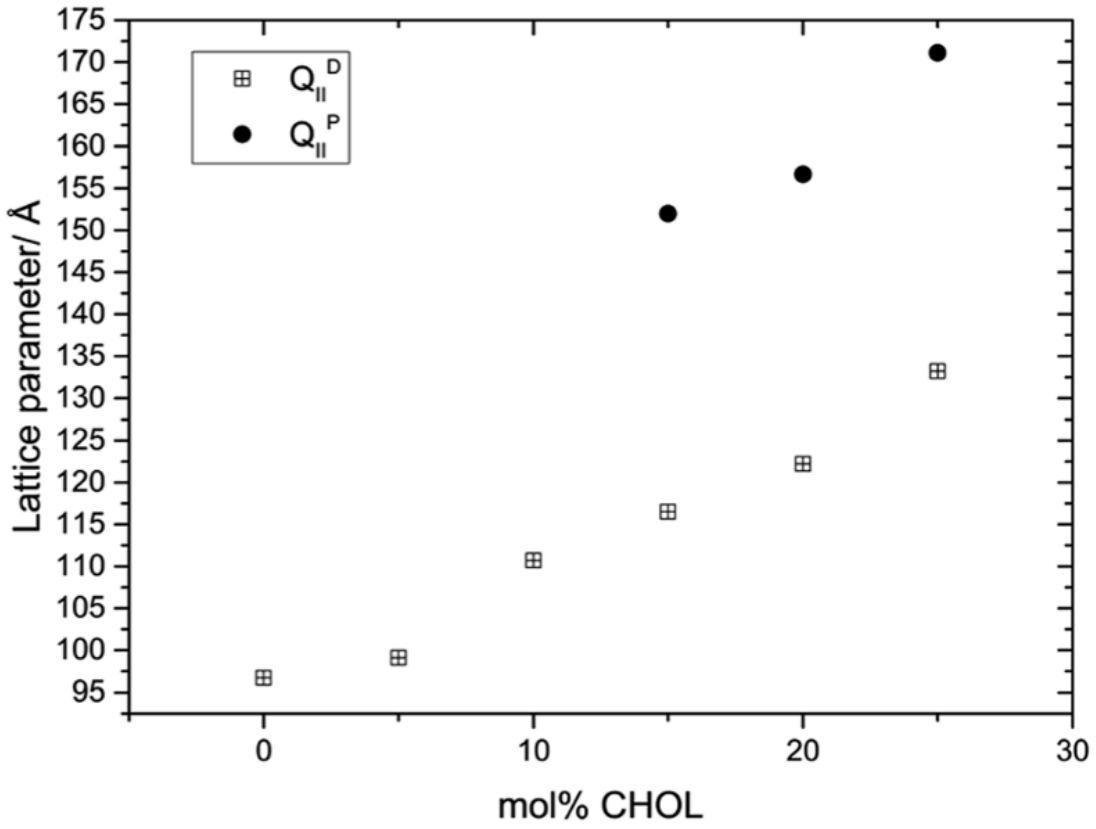

Figure 5.9: Effect on lattice parameter upon doping monoolein with cholesterol (at 35 °C and in excess water). The presence of cholesterol leads to a modest increase in the lattice parameter, up to concentrations of 28 mol % (at which point cholesterol reaches saturation in the monoolein matrix, with the excess cholesterol forming crystals with a distinct scattering peak at 34 Å). *Figure adapted from*: A.I.I. Tyler et al. *Soft Matter* **11**, 3279–3286 (2015).

The effect of cholesterol on the phase behavior and lattice parameter of monoolein has been previously studied[151], and is here shown at elevated temperatures of 35 °C in *figure 5.9*. Cholesterol is shown to result in modest swelling of the P_n3_m cubic phase (denoted as Q_{II}^{D}; diamond), as the incorporated rigid sterol interacts with the hydrocarbon chains of monoolein molecules and lowers the lateral pressure within the plane of the hydrocarbon chains (by inhibiting *trans-gauche* isomerization)[152], thus reducing the spontaneous curvature within the monolayer and resulting in a propensity of the structure to swell. At increasing concentrations of cholesterol, phase coexistence between the P_n3_m and I_m3_m bicontinuous cubic phases occurs. Such phase coexistence could hinder the interpretation of AFM experiments based of these systems, and

therefore both the temperature and cholesterol concentration must be tuned to remain within the single phase region.

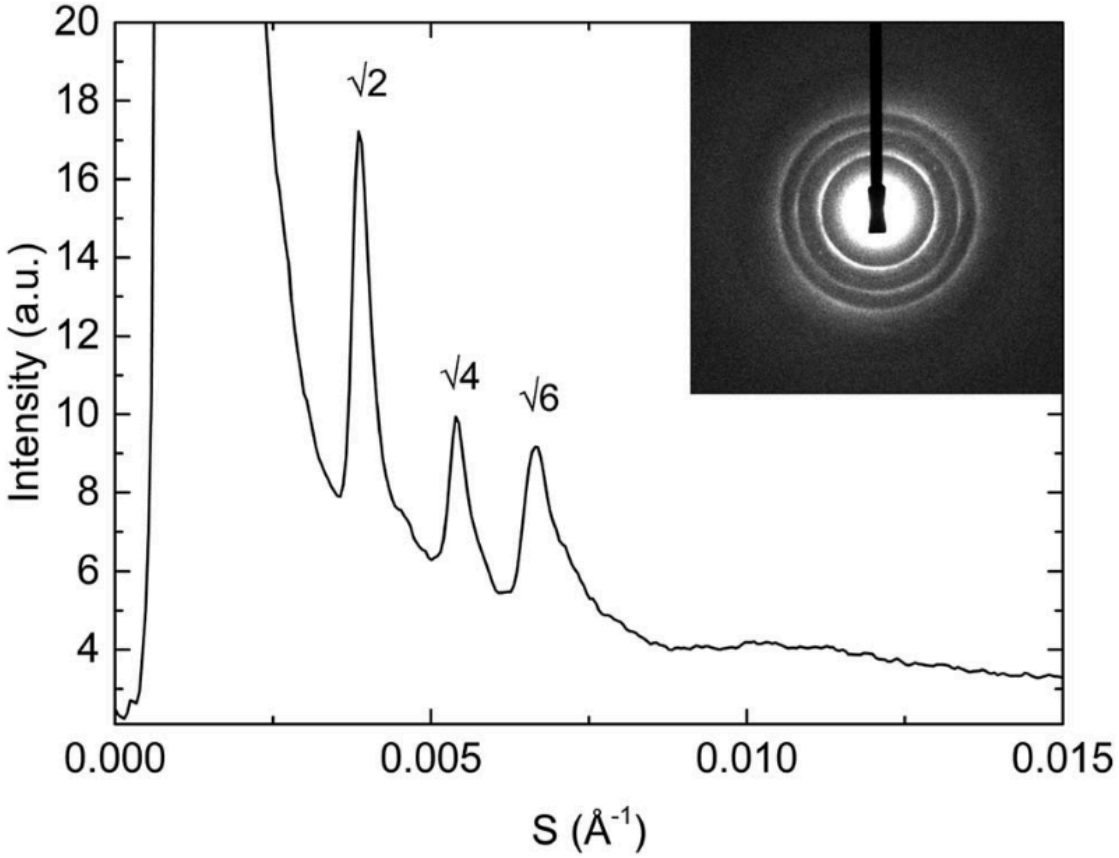

Figure 5.10: SAXS pattern for the $\boldsymbol{P_n3_m}$ bicontinuous cubic phase formed from a mixture of monoolein:cholesterol:DOPG (80:15:5 mol %) in excess water. The cubic structure is swollen as the peaks are pushed towards smaller values of *s*, with the disappearance of higher order reflections indicating the presence of significant thermal fluctuations within the structure. *Figure adapted from*: A.I.I. Tyler et al. *Soft Matter* **11**, 3279–3286 (2015).

By doping the monoolein:cholesterol mixture with trace amounts of a phospholipid containing a charged headgroup (in this case DOPG, as shown in *figure 5.10*), the bicontinuous cubic structure can be swollen to lattice parameters in excess of 400 Å[39]. Such repeat distances are routinely resolved by AFM, although it remains a possibility that such a soft structure (with an internal aqueous volume far in excess of 50 %) requires very low applied forces (between the AFM tip and the sample) in order to preserve the integrity of the cubic phase during the imaging process; such fine control over tip-sample forces cannot be attained *in-house*.

5.2.2 AFM imaging of swollen bicontinuous cubic phases

A first step in imaging bicontininuous cubic phases with an increased lattice parameter is to engineer thin lipid films of MO:Chol. The presence of cholesterol leads to modest swelling of the MO lattice parameter (from 97 Å for the P_n3_m cubic phase of MO, to 133 Å at 25 mol % cholesterol), and is further expected to stiffen the membrane. As has been previously noted, the presence of cholesterol results in coexistence of both the P_n3_m and I_m3_m bicontinuous cubic phases (as detected by SAXS at concentrations of ≥ 23 mol % chol at 20 °C)[151]. As the AFM is operated at room temperature, MO:Chol films of 80:20 mol % were prepared in order to stay within the P_n3_m region of the phase diagram, ensuring that only a single bicontinuous cubic phase need be considered when interpreting the resulting images.

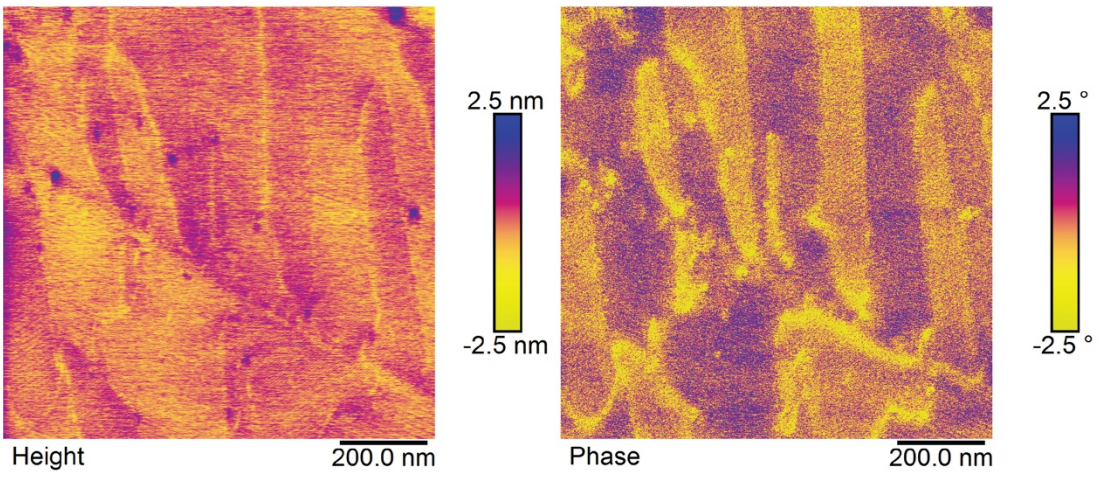

Figure 5.11: Height and phase images of hydrated thin films of MO:Chol (80:20 mol %) on HOPG over an area of 1 μm^2. The images show that lipid films have been successfully deposited, with dark spots in the height data corresponding to defects ('holes') by which the AFM tip can penetrate into the bulk film. The contrast between the distinct grains in the phase image could suggest that two distinct faces of the cubic structure are present at the lipid-water interface.

Initial larger-scale (1 μm^2) imaging (as shown in *figure 5.11*) of the thin lipid films of mixtures of monoolein:cholesterol (80:20 mol %) revealed distinct grains in the cubic structure, with grain boundaries clearly visible and significant contrast in the phase images. Such contrast in the phase images could be indicative of two distinct lattice planes coexisting as the terminating surface structure, as phase contrast (in tapping-

mode AFM) arises through differing interactions between the oscillating tip and the sample surface (resulting from difference in adhesion, stiffness etc.). In addition to distinct grains, defects can be observed as 'holes' in the height data, highlighting areas in which there is a void in the bicontinuous cubic lattice. Both of these (crystal) features cannot be observed by ensemble scatting techniques, and thus represent a novel view of bicontinuous cubic lipid phases.

At the sub-micron length scales occupied by the lyotropic cubic lattice, the repeating structure shown in *figure 5.12* were observed, with FFT's of the image revealing a rectangular lattice, although the face through the P_n3_m cubic phase for which these images correspond to has not been assigned. As the images obtained for monoolein films doped with cholesterol are routinely of high resolution (relative to AFM of pure monooelin as shown in *figure 5.6*), it is likely that the effect of cholesterol to stiffen the membrane is conducive to the AFM imaging process, making the sample more resistant to deformation (and destruction) by the AFM probe. It is clear that these experiments will be greatly enhanced by an understanding of how to engineer the thin films with prior knowledge of their alignment, with the presence of cholesterol likely forming the most robust thin films for study by AFM.

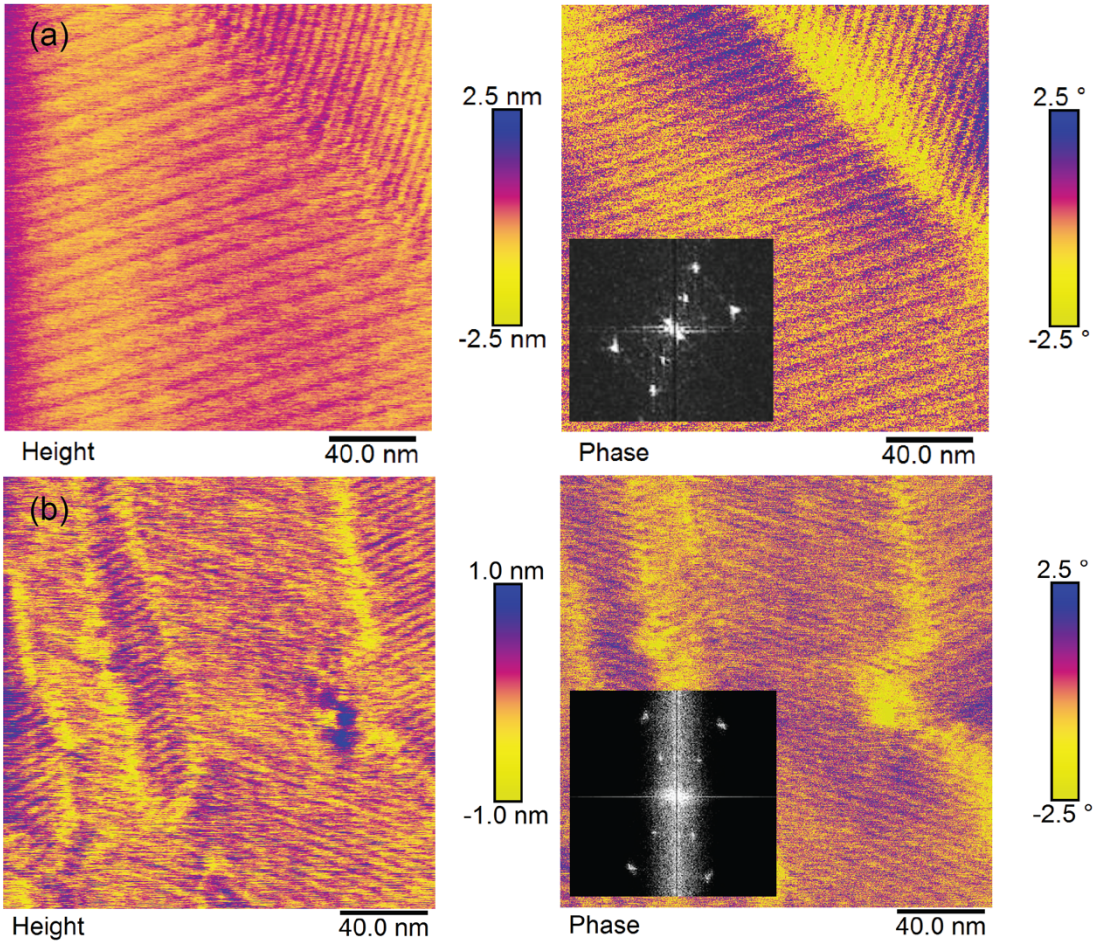

Figure 5.12: Height and phase images of two distinct areas of the MO:Chol (80:20 mol %) interface with distinct spacing. Insets shows the fast Fourier transform of the corresponding image, for which two rectangular lattices are observed.

Incorporating a third component (i.e. a charged lipid) into the lipid film was not successful. Extending this AFM methodology of imaging inverse lipid films to 3-component lipid systems presents further experimental challenges; for the lipid films to present the phase behavior as their equivalent bulk mixtures, the samples must be homogenous with cholesterol and charged phospholipid dopants dispersed evenly through the cubic monoolein matrix. Even in bulk samples, this has been difficult to achieve and has required extensive vortexing and numerous thermal cycles. It is feasible that homogenous thin films of 3-component (swollen) cubic phases can be engineered through both shear of the film between two solid interfaces, and of thermal cycles of the lipid film across a phase boundary, and thus remains a direction for further research.

5.3 Other inverse lipid phases

In addition to the bicontinuous cubic phases adopted by monoolein systems (P_n3_m and I_m3_m), further lipid inverse phases exist for which a knowledge of their interfacial structure is absent. The I_a3_d bicontinuous cubic phase, built of trigonal units of water channels and which contains the lowest volume of water, is usually only found in lyotropic systems that have not reached full hydration, rendering AFM unsuitable as the lipid films required for visualization exist in excess water. However, reports that a synthetic glycolipid adopts a bicontinuous cubic phase with the I_a3_d space group in excess water provides a means of circumventing this bottleneck[28].

Inverse micellar (discontinuous) cubic phases, in which there is close-packing of spherical micelles with a water core, represent another group of lyotropic phases that contain a high degree of negative interfacial curvature (whereby the interface curves towards the aqueous region and away from the hydrocarbon tails), and for which their terminating surface structure has not been studied. A notable example is formed from 1:2 mixtures DOPC:DOG, which adopts inverse micellar packing with the F_d3_m spacegroup in excess water[29]. An interface with the aqueous bulk in which the exposed hydrocarbon chains of the inverse micelles are in direct contact with water is energetically unfavourable, and it is therefore likely that the surface of inverse micellar phases are terminated with an adsorbed lipid monolayer, resulting in an interface between hydrophilic lipid headgroups and the bulk.

Finally, the 2D hexagonal phase (spacegroup P_6mm) is formed in many lipid systems which favor an intermediate negative interfacial curvature, in which the lipid molecules are packed into cylindrical micelles. The 2D hexagonal phase is the most common of the inverse lipid phases adopted by biologically relevant lipids[32], and is often found to exist at elevated temperatures for many phospholipid systems as the increased chain splay that results from thermal motion favours geometries that accommodate higher degrees of curvature. A phospholipid system adopting the 2D hexagonal phase in excess water and at room temperature (i.e. suitable for the AFM experiments proposed here) is

formed of 3:2 mixtures of DOPC:oleic acid[153]. Data was not collected for this system, but is included here for completeness, and will form the subject of future studies.

5.3.1 An I_a3_d bicontinuous cubic phase adopted by a synthetic glycolipid in excess water

As the synthetic glycolipid used here (β-glc-$C_{10}C_6$, see *figure 5.13* for chemical structure) is not a commercially available and well characterised lipid, verification of the reported phase behavior is required.

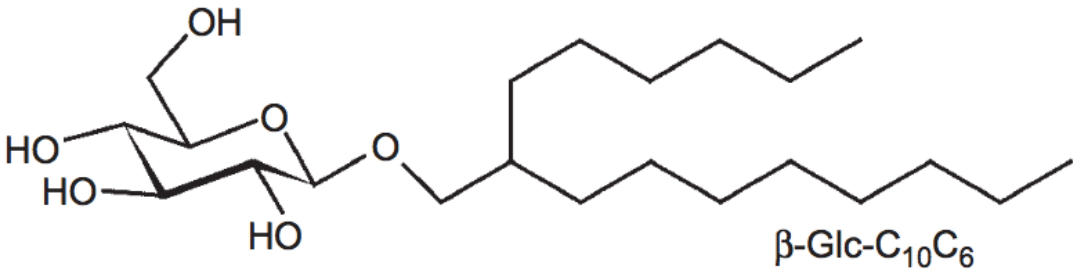

Figure 5.13: Chemical structure of the β-glc-$C_{10}C_6$ glycolipid which forms the $\boldsymbol{I_a3_d}$ bicontinuous cubic phase in excess water.

The surprising observation that the I_a3_d bicontinuous cubic was adopted in excess water left the possibility that a dehydrated sample could have caused an erroneous observation; as a precaution, glycolipid samples hydrated to both 70 and 95 wt. % water were prepared with vigorous mixing and allowed more than 24 h. at room temperature to equilibrate with their aqueous surroundings before SAXS measurements. It was confirmed that the glycolipid does indeed adopt the I_a3_d cubic phase, as observed by the characteristic diffraction pattern shown in *figure 5.14*. It was noted that the hydrated lipid had a waxy appearance (cf. hydrated monoolein, that has a similar appearance to that of a hydrogel) with a clear boundary against the aqueous bulk, although this could be expected as the I_a3_d structure absorbs the least amount of water (per volume of lipid) as compared to the P_n3_m and I_m3_m bicontinuous cubic phases. This β-glc-$C_{10}C_6$ glycolipid species therefore provides a viable means of imaging the I_a3_d surface structure, as a thin film in excess water.

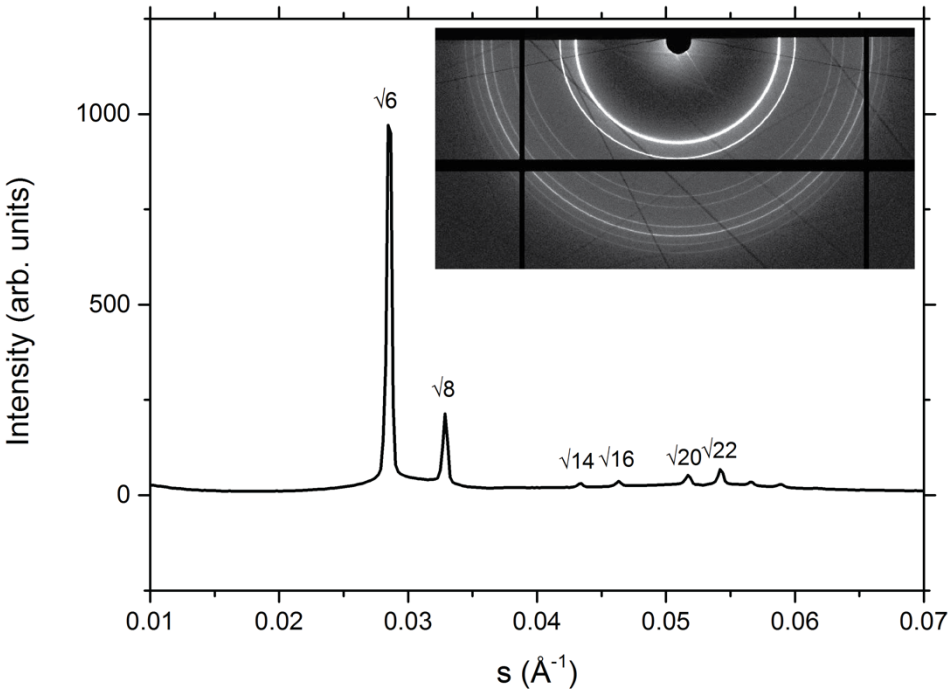

Figure 5.14: SAXS pattern for the $\boldsymbol{I_a3_d}$ bicontinuous cubic phase formed by the synthetic β-glyc-$C_{10}C_6$ glycolipid in excess water.

Thin lipid films of the β-glyc-$C_{10}C_6$ glycolipid were deposited on HOPG, and after hydration yielded the AFM images shown in *figure 5.15*. A lipid film has clearly been formed as boundaries between distinct grains can be clearly observed on the μm scale, both in the height and phase images presented. Resolution of the scale of the cubic lattice was not obtained, and it is not possible to determine from these images alone if it is simply a case of insufficient resolution, or if the deposited film failed to formed the bicontinuous cubic phase after hydration. Clearly, an understanding of this system would also be greatly enhanced by GISAXS data[144].

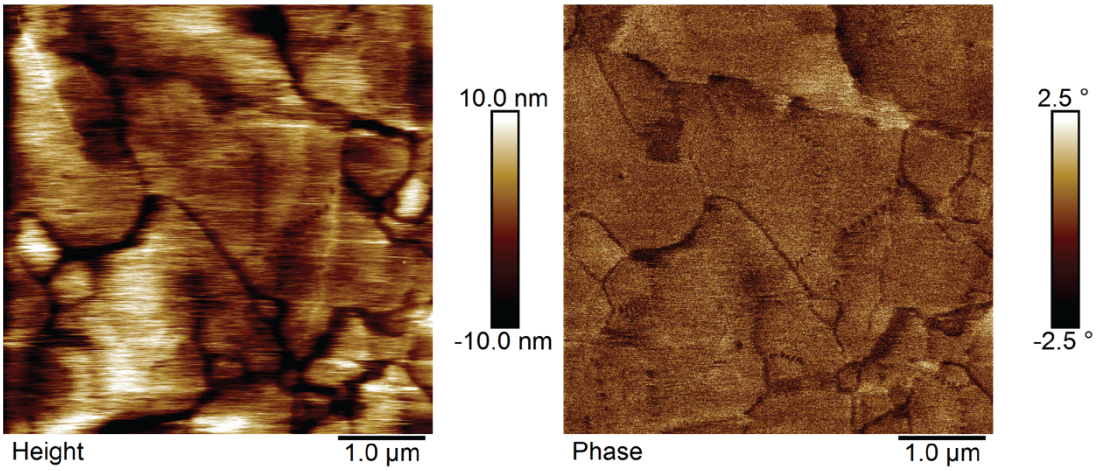

Figure 5.15: Height and phase images of the hydrated thin films of the synthetic glycolipid on HOPG. Grain boundaries can be clearly observed but resolution on the the scale of the cubic lattice was not obtained.

5.3.2 Inverse micellar

The hydrated F_d3_m inverse micellar cubic phase can be induced to form in phospholipid systems in the presence of an excess of unsaturated diacylglycerol (e.g. 1:2 DOPC:DOG)[29], introducing extremely high negative interfacial curvature to the system. As such, micelles with defined packing and distinct lattice parameters can be formed in excess water, opening up avenues as vehicles for drug delivery if the bulk (hydrated) lipid mixture can be dispersed as 'micellarsomes'. Knowledge of the surface structure is therefore essential in understanding how to disperse such structures and to engineer how their content can be released. A previous study of thin films of the F_d3_m inverse micellar phase demonstrated that deposition by spin coating to give these supported complex structures is possible (as evidenced with resultant surface X-ray scattering patterns), but only very low resolution AFM data was reported (scan width = 50 µm), giving no insight into the structure of the terminating cubic lattice[139].

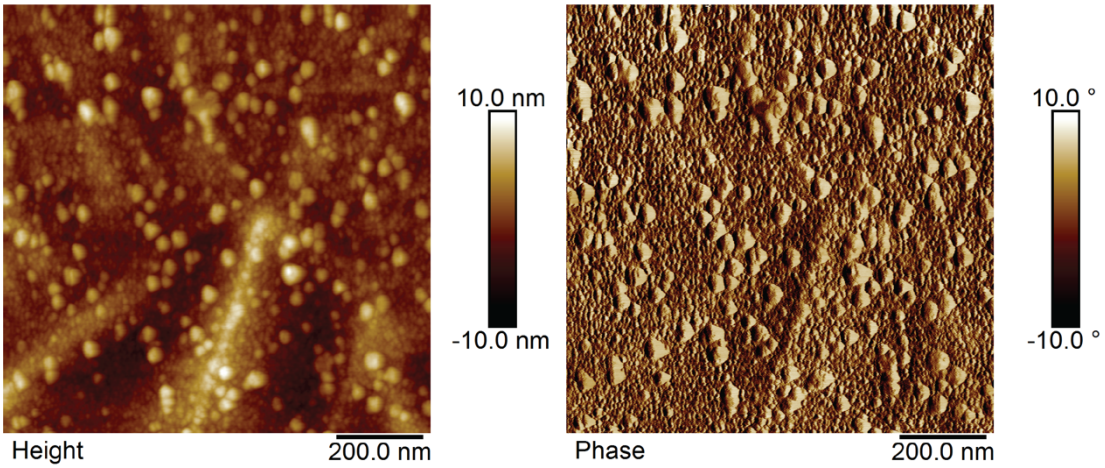

Figure 5.16: : Height and phase images of hydrated thin films of DOPC:DOG (33:67 mol %) on OTS treated glass.

Deposition of thin films of DOPC:DOG (33:67 mol %) on OTS treated glass (as reported by Nylander[139]) and subsequent hydration resulted in the images shown in *figure 5.16*. Dispersed circular grains can be observed that are sub-100 nm in size, but a clear plane cannot be discriminated from the surrounding film, and the size and polydispersity suggests that these are individual grains of the F_d3_m micellar crystal rather than the individually packed micelles. In addition, the diffuse phase boundary between the coexisting $L_C/H_{II} \rightarrow F_d3_m$ is at 27 °C for this 1:2 DOPC:DOG mixture, and therefore the deposited film will be very close to this boundary during imaging within the AFM (operated at RT). Temperature control would verify these observations, both by setting the temperature deeply within the F_d3_m region of the phase diagram, and by provided the ability to anneal the thin film *in situ* .

5.4 Conclusions and Outlook

The experiments discussed in this chapter outline the systems (and methodologies towards their formation as hydrated thin films) for which their surface lattice can be resolved by AFM, giving an insight into their terminating interfacial structure along with the visualization of defects and grain boundaries (which are not observable by ensemble techniques). Visualization of the P_n3_m bicontinuous cubic lattice was reproduced from earlier reports[138], and extended to incorporate cholesterol in an attempt to both increase the lattice dimensions whilst stiffening the structure, thus increasing the viability of

routinely collecting the high-resolution AFM images required. Images were obtained showing grain boundaries between distinct planes, and a rectangular lattice was observed at smaller length scales, albeit without an assignment to a given crystal plane. Further image analysis could be applied in extracting the FTT which can be assigned to a given crystal plane, although this was not the focus of the research presented here. In addition, cholesterol is often used as a dopant in *in meso* crystallization of membrane proteins[151], and its effect on the surface structure of monoolein is therefore of interest. The observation of such domain boundaries and defects could therefore inform the crystallization of membrane proteins *in cubo*.

It is demonstrated how this methodology can be extended to other inverse phases, with the deposition of lipid systems that form I_a3_d bicontinuous cubic and F_d3_m inverse micellar phases respectively. For both systems, the bulk (μm) surface can be visualized and distinct grains can be observed, although resolution on the scale of the crystal lattice was not obtained. Standard protocols in the formation of these films are required, with additional structural techniques (i.e. GISAXS) likely providing essential information on the alignment of the lipid film, that will greatly enhance the interpretation of AFM data.

A method to simultaneously study both the surface and the bulk of such structures would give unprecedented insight into how these structures terminate at the interface. Recently, a synchrotron beamline at the ESRF with combined AFM and GI-SAXS has come online[144], allowing the surface structure of the inverse lipid phases to be unambiguously identified for the first time. Beamtime is scheduled for the experiments outlined here for July 2016, and therefore unfortunately cannot inform the interpretation of these results. It is anticipated that it will be possible to resolve the surface structure of inverse lipid phases using AFM with simultaneous GI-SAXS measurements, providing unprecedented 3D information on the alignment of the lipid film. A standard protocol for forming inverse lipid films can developed, with a view to comprehensively surveying the surface structure of phases. A detailed understanding of the surface structure, including defects, dislocations and grains boundaries, will be highly important in engineering inverse phases for applications ranging from high surface area

catalysts and tuneable photonic crystals and *in meso* crystalisation of large membrane proteins.

Chapter 6: Membrane perforation by intermedilysin

Self-assembly of pore-forming protein toxins upon the cell membrane result in large, transmembrane channels through which ions, small molecules and larger macromolecules can flow (by passive transport), facilitating lysis and causing eventual cell death[154]. This represents a major mechanism of both attack by pathogenic bacteria (for example with the intermedilysin (ILY) toxin which is secreted by intermedius steptococus[155]), and of defense by the human immune system (e.g. by the complement system through the self-assembly of the membrane attack complex). This process of membrane binding is followed by a significant structural rearrangement to overcome the energy barrier associated with forming a membrane pore, lending itself to biophysical investigation in which AFM can provide a powerful tool in imaging such intricate surface processes.

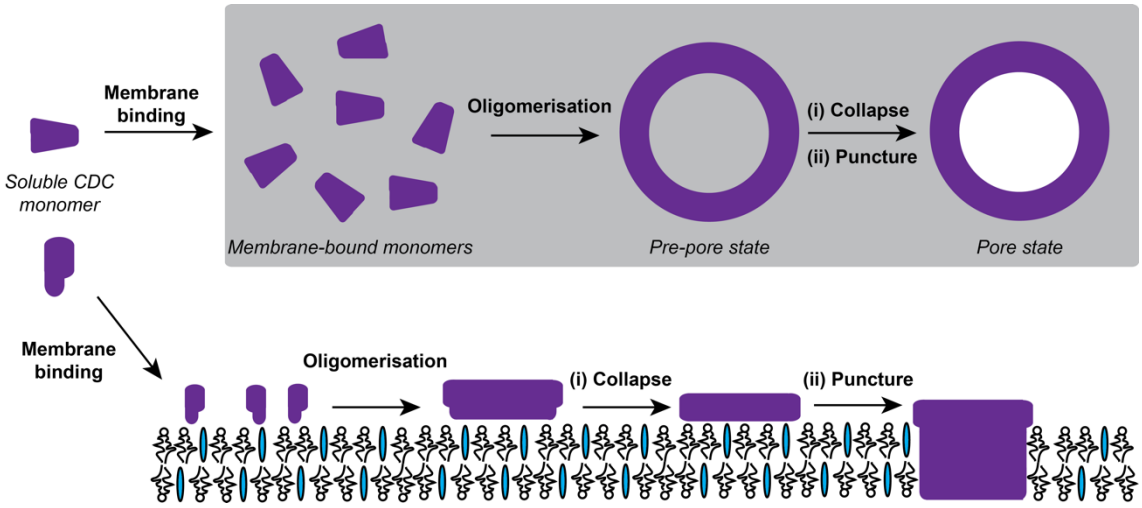

Figure 6.1: Schematic showing the pathway to transmembrane pore formation by the MACPF/CDC family. The collapse and puncture of the lipid bilayer membrane is a concerted process for the majority of CDC's.

Amongst pore forming protein toxins (PFT's), there are two distinct families, denoted α- and β-, in which the transmembrane pore is stabilized by an α-helix and a β-sheet respectively. Within this family of β-PFT's, intermedilyin belongs to the membrane attack complex/perforin/cholesterol-dependent cytolysin (MACPF/CDC) subclass where the topology associated with pore formation is highly conserved for all members.

The CDC's exist as soluble monomers that are comprised of four domains which dictate membrane binding, oligomerization and insertion to give a transmembrane pore. Generally, they bind to membranes with a high cholesterol content (> 25 mol %)[156] via the hydrophobic loops present in domain 4[157], as shown in *figure 6.1*. Oligmerisation of these membrane-bound monomers leads to the formation of the pre-pore state[158,159] *via* interactions between β strands in domain 3 of neighboring monomers. The oligomeric prepore then undergoes a dramatic structural rearrangement to overcome the barrier (i.e. line tension) to transmembrane pore formation in the absence of any external energy source. A collapse in domain 2 (with a corresponding height difference of ca. 5 nm) acts to bring the two transmembrane helices (TMH's) of domain 3 to the membrane[159]. A synchronized transition to β-hairpins occurs, puncturing the membrane with the formation of a large, amphipathic β-barrel pore[160].

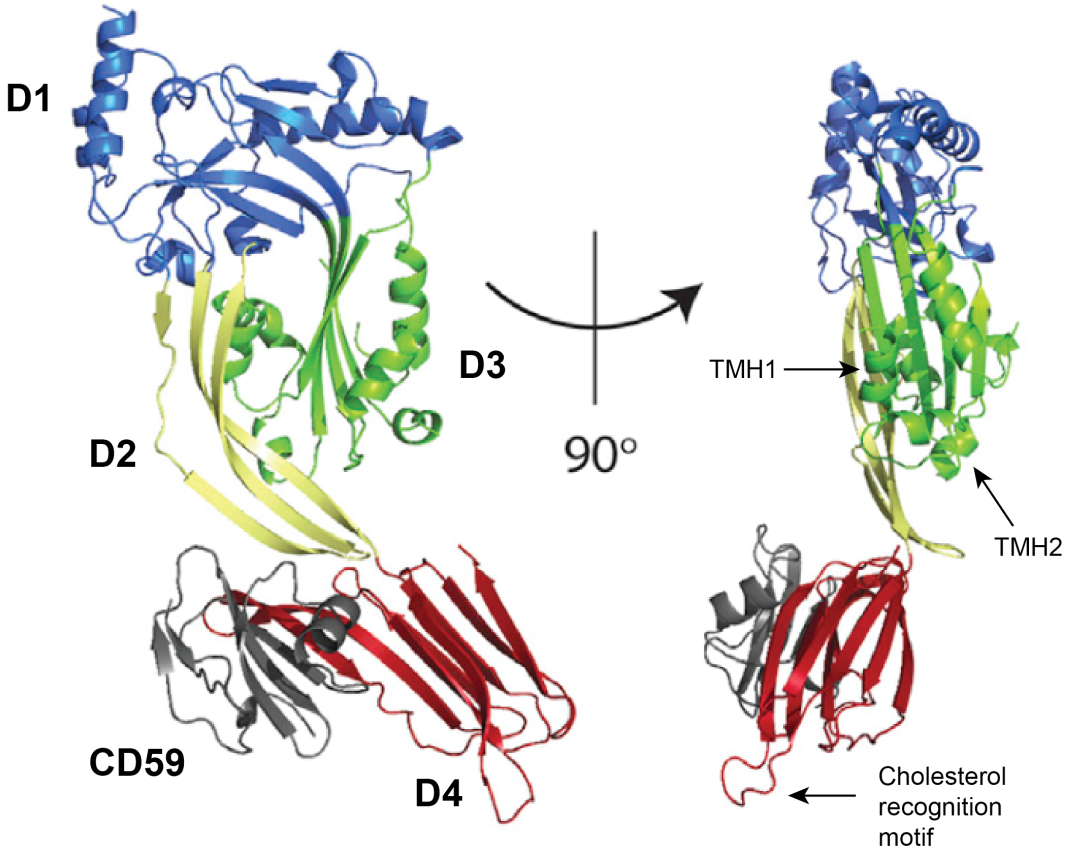

Figure 6.2: Structure of intermedilysin (ILY) bound to the human CD59 receptor. ILY is formed of four domains which are conserved across the MACPF/CDC family. Figure taken from: S. Johnson *et al.*, *Cell Reports* 3, 1369–1377 (2013).

In contrast to other CDC's, intermedilysin binds to the membrane *via* the complement CD59 receptor, and not directly to cholesterol. ILY is itself secreted as a soluble monomer which hijacks the GPI-anchored CD59 that is found on the membrane surface of nearly all (circulating) human cells[161] (n.b. - CD59 is itself an immune receptor that inhibits the formation of the membrane attack complex on the host's cells). The CD59 molecule is bound to ILY as oligomerisation to the pre-pore state occurs, and is released upon conversion to a transmembrane pore[162]. As a result, two distinct molecular species must be considered, thus increasing the complexity of the model system required for AFM visualization of this pore forming process.

AFM studies of the pathway to pore formation of cholesterol dependent cytolysins have been rapidly gaining pace as AFM methodologies have been tailored towards achieving high temporal resolution of soft, biological samples. As somewhat of an intermediate between the high-spatial resolution that can now be achieved with cryo-EM (since the advent of direct electron detectors and advanced particle analysis methods[163]) and the high-temporal resolution offered by fluorescence methodologies (e.g. FCS), AFM is the ideal tool in studying the self-assembly of these oligiomeric pores upon defined model membrane surfaces in near-physiological conditions. Pioneering studies applied AFM to directly demonstrate the vertical collapse of perfringolysin towards the membrane, where time-lapse visualization after the addition of DTT to a disulfide-locked (pre-pore) mutants showed a height difference of ca. 4 nm between the pre-pore and pore states. More recently, AFM has been applied in complementing the static view of suilysin (provided by cryo-EM) with image sequences in which pre-pore state is mobile on the membrane surface prior to collapse and subsequent pore formation[164]. AFM has been further applied in studying the effect of the membrane lipid composition upon the mechanism of pore formation by listeriolysin[165], in which higher concentrations of cholesterol were shown to drive the formation of complete pores (as opposed to the 'arc's' observed at lower concentrations), and of lysenin[166], where it was inferred that reorganization of phase-separated (SM:Chol:DOPC) membrane occurred using high-speed AFM . Most recently, the compressive force applied by the AFM probe to induce

the collapse of perfringolysin oligomers has been correlated with the intramolecular forces that drive pore formation[167].

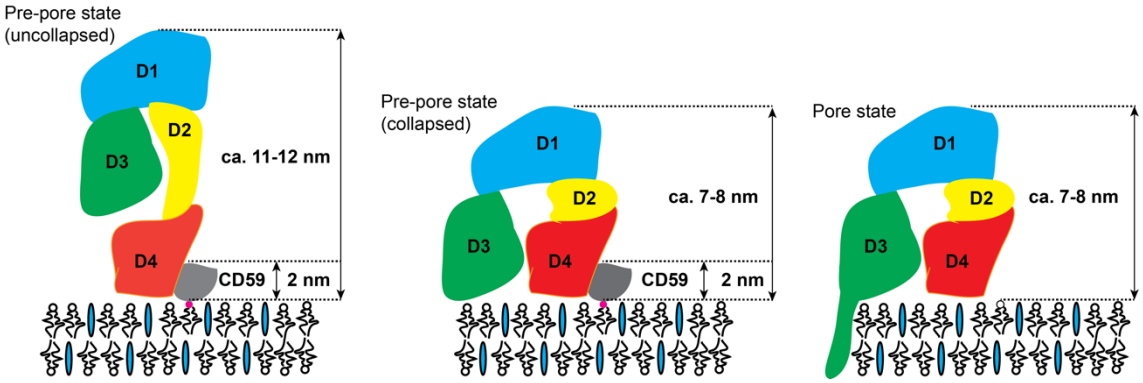

Figure 6.3: Schematic showing the relative heights of the ILY oligomer at distinct points in the pathway to pore formation, that can each be imaged by AFM.

The work presented in this chapter attempts to unravel the mechanism of membrane perforation by intermedilysin in model systems in which the lipid composition and ILY mutants can be tuned in order to deconvolute the roles of the molecular species involved. The use of the supported lipid bilayers allows for the height of the ILY oligomer to measured relative to the membrane background, thus providing direct means of determining whether the oligomer has undergone a collapse towards the membrane, and therefore informs our understanding of the pathway of pore formation.

6.1 Tuning the lipid composition of supported model membranes to induce self-assembly of protein pores

Previous biophysical studies have successfully reconstituted intermedilysin pores into model phospholipid membranes, most recently using a calcein-based lysis assay of small unilamellar vesicles (as evidenced by calcein release from loaded vesicles upon formation of a functional ILY transmembrane pore), for which the lipid composition was reported as 3:2:3:2 DOPS:DOPC:DOPE:Chol[168]. Each lipid present in the minimal model system is proposed to play a distinct role in its mimicry of the the native cell membrane. DOPS is required as it binds the CD59 protein receptor, which has been engineered for this purpose as a GPI-anchor analogue. DOPC provides the fluid phospholipid matrix in which other lipid species can reside. DOPE introduces a degree of curvature elastic stress into a planar lipid bilayer, thus favoring events that are disruptive towards the

membrane such as pore formation, with its propensity to form hexagonal phases likely stabilizing the membrane lipid fractions ejected during pore formation into the bulk[32]. Cholesterol has an ordering effect upon the phospholipid membrane with the induction of the liquid-ordered phase, and is required for pore formation to run to completion for these *cholesterol-dependent* cytolysins. In order to facilitate AFM imaging of ILY pores, the reported lipid compositions must be transferred to supported lipid bilayer membranes, and further tuned in order to optimize the pore-forming process.

6.1.1 PS:PC:PE:Chol (3:2:3:2)

The 3:2:3:2 DOPS:DOPC:DOPE:Chol lipid composition that has previously been successful in reconstituting the functional ILY pores to model membranes was transferred to a supported lipid bilayer format[74], in which domains were observed at a height of ca. 0.5 nm above the surrounding lipid matrix. This is likely due to the ordering effect of cholesterol upon the phospholipids present[169], as they all harbor unsaturated, oleoyl hydrocarbon chains, albeit the relatively low proportion of cholesterol (20 mol %) results in a sparse distribution of domains across the lipid bilayer. Interestingly, upon addition of CD59/ILY^{WT} (50:50 mol %), aggregation of protein molecules is seen to occur upon the domains and not upon the surrounding lipid matrix (as shown in *figure 6.4* below), with minor streaking suggesting that mobile protein molecules are being pushed across the membrane surface by the AFM tip.

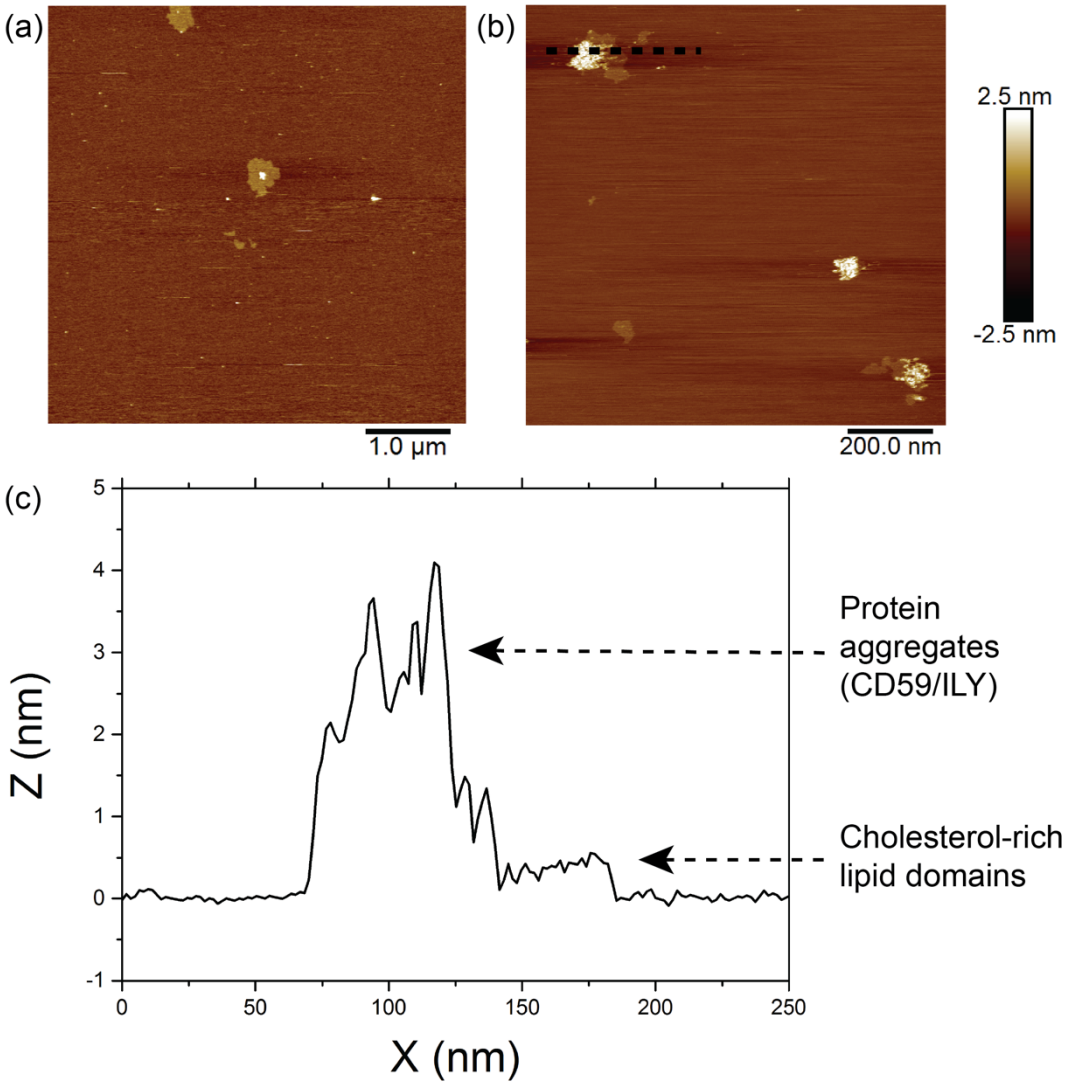

Figure 6.4: Tapping-mode AFM images of supported lipid bilayers composed of DOPS:DOPC:DOPE:Chol (3:2:3:2) incubated in the presence of ILY/CD59 (1:1).

The strong preference for CD59/ILY aggregation upon the observed domains suggests an affinity for cholesterol-rich regions of the model membrane. As the CD59 receptor has been engineered to bind phosphoserine headgroups[170] (i.e. DOPS), this suggest that either: (*i*) DOPS and cholesterol are found to coexist locally with such domains, or (*ii*) cholesterol still plays an active role in membrane binding. The corresponding height of these protein aggregates is of the order of 3 nm above the supporting membrane surface; this height data is most consistent with the presence of the CD59 receptor (128 a.a.; ca. 20 kDa), although the disordered nature of these aggregates makes any interpretation problematic. In addition, the confinement provided by the domain boundary may lead to significant crowding that inhibits oligomerisation of any bound ILY.

6.1.2 PC:Chol:PS (5:4:1)

In order to increase the size of the cholesterol-rich domains observed in 3:2:3:2 mixtures of DOPS:DOPC:DOPE:Chol, thus increasing the available area for CD59/ILY binding, DOPE was discarded and the relative concentration of cholesterol increased with a 5:4:1 mixture of DOPC:Chol:PS. This had the effect of rendering the whole lipid bilayer liquid-ordered (L_O), with cholesterol and DOPS equally dispersed throughout the DOPC lipid matrix, as a single phase lipid bilayer was observed without any indication of domain formation. Incubation of the supported lipid bilayers in the presence of CD59/ILY^{WT} (1:1) led to significant binding to the model membrane surface, and subsequent clustering as shown in *figure 6.5* below. The spots (i.e. single molecules) and clusters observed in image *6.5 (a)* have a corresponding height of ca. 2 nm with increased definition over the aggregates observed previously. It is therefore proposed that such areas represent bound CD59, with clustering increasing the viability of AFM imaging owing to the 'jamming' effect between particles[171]. Higher features can be observed as bright spots that indicate the presence of ILY, but the sparse distribution of these image features inhibit any further structural insight.

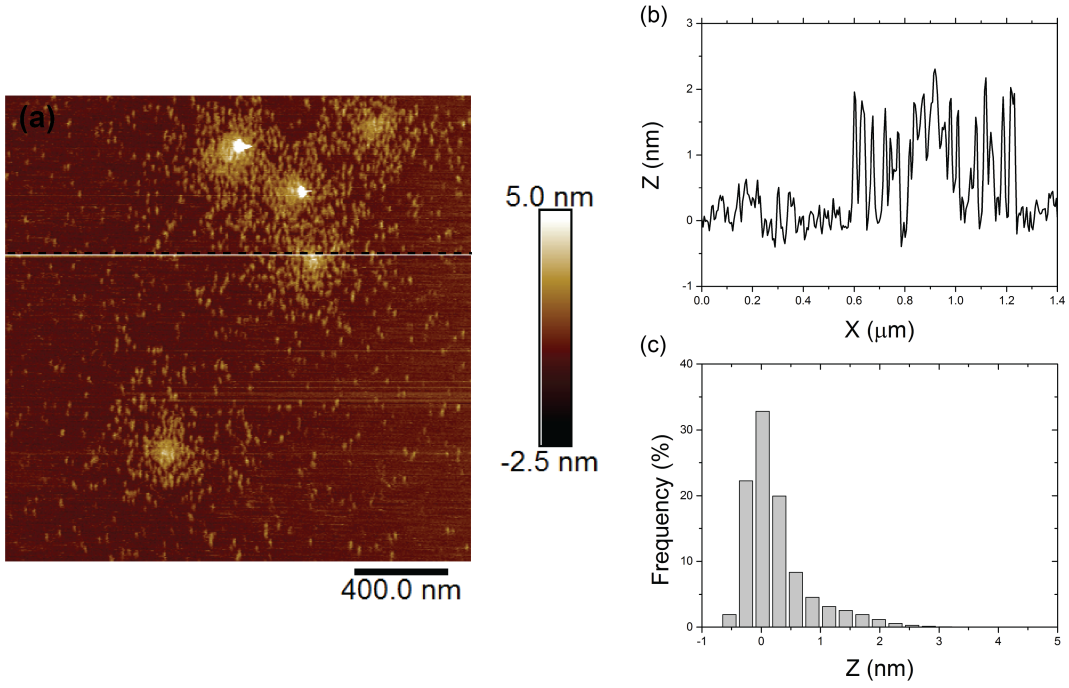

Figure 6.5: (a) AFM image displaying single molecules of the CD59 receptor bound to a supported lipid bilayer composed of DOPC:Chol:DOPS (5:4:1). The corresponding (b) cross-section and (c)

z data (as taken from each pixel in the image) shows the CD59 molecules to occupy a height ca. 2 nm above the membrane surface, consistent with that expected for a 18-20 kDa protein[162].

In order to drive pore formation *via* the oligomerisation of bound ILY monomers, the supported bilayers were incubated at 37 °C for 1 h in the presence of CD59/ILY (1:1). This prolonged incubation period was far in excess of that required to form pores upon corresponding lipid monolayers (as required in the sample preparation for visualization by cryo-EM[168]); it is plausible that diffusion upon a supported lipid bilayer (as CD59/ILY is directly bound to the DOPS lipid) is inhibited relative to that of an interfacial monolayer, thus decreasing the rate of oligomerisation. Such prolonged incubation readily yielded pore formation as can be seen in *figure 6.6* below.

At low surface coverage of CD59/ILY (as shown in *figure 6.6 (a)*), fully-formed ILY pores can be observed as rings in the image with a height of ca. 7 nm above the lipid membrane surface (as extracted from the histogram of *z* data). It can be reasonably assumed that these images represent the final, transmembrane state as the oligmeric structures are immobile on the membrane surface (i.e. they can be visualised by AFM without 'streaking' in the images characteristic of the mobile, pre-pre state[164]). Cross sections through the pores do not show any penetration below the level of the membrane, owing to the similar size of the probe (ca. 10 nm diameter at the tip apex) relative to the internal diameter of the ILY pore (25-30 nm[161]). The membrane surface is semi-saturated with molecules of the CD59 receptor, most likely released from the ILY oligomer after pore formation as clustering of the CD59 molecules is observed around the oligomeric pores. The lipid membrane surface can be observed as the darkest regions in the image, thus the height from the membrane surface to the tip of the pore can be measured, revealing whether the collapse from the pre-pore state has occurred. As seen in the *z* data presented in *6.6 (a)*, there is a broad distribution spanning ca. 0-2 nm which accounts for both areas of the membrane surface and of membrane-bound CD59 that has been released from the ILY oligomer upon formation of a transmembrane pore. A second distribution (centered at ca. 7 nm relative to the exposed membrane) corresponds to the collapsed state of the ILY pore (in agreement with previous observations of collapsed CDC pores[159]). In summary, the observation of dispersed but immobile ILY oligomers,

with a height of 7 nm above the membrane surface, represent the transmembrane pore state of ILY.

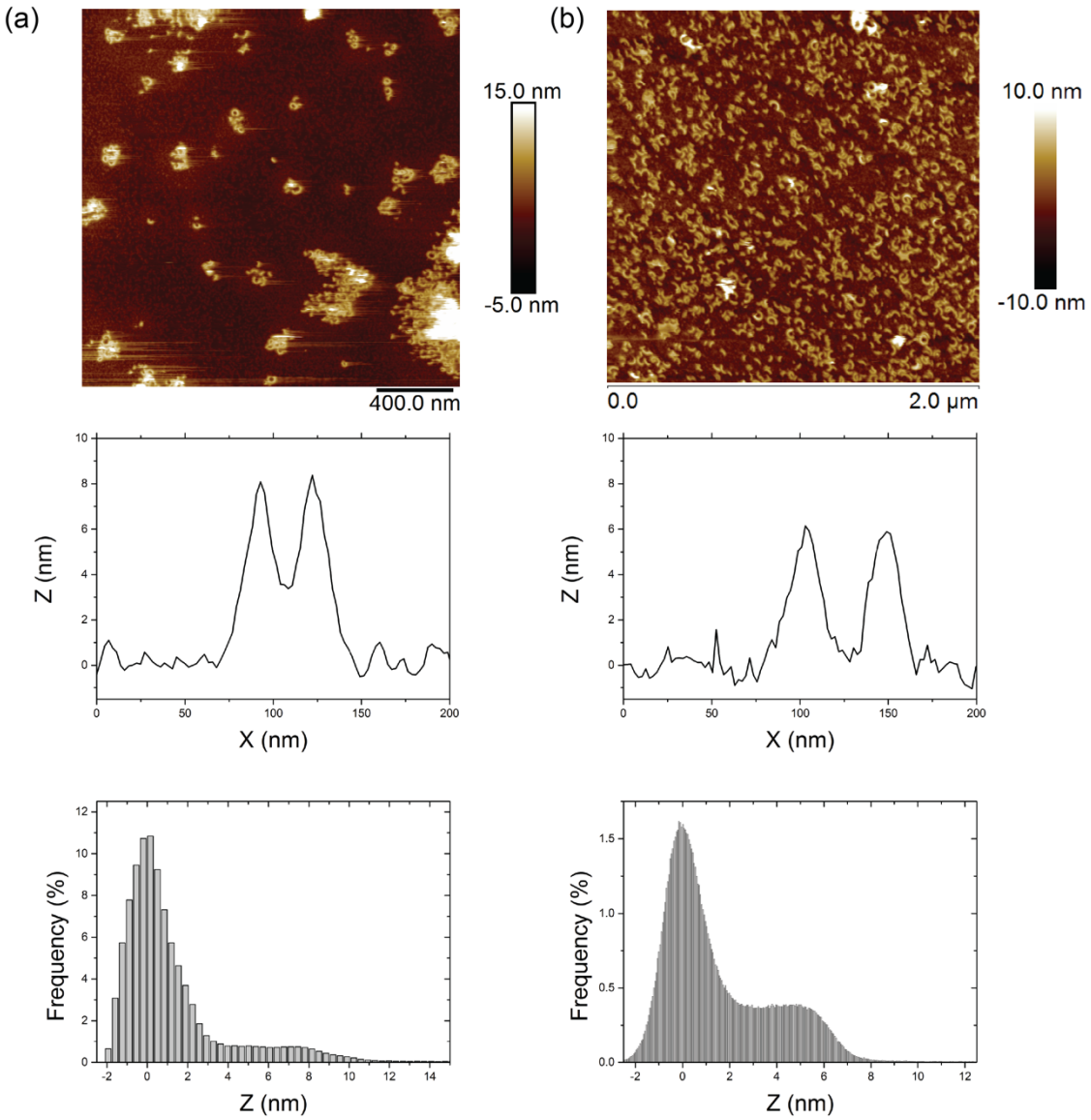

Figure 6.6: AFM images (and corresponding cross-sections and height histograms) of supported lipid bilayers composed of DOPC:Chol:DOPS (5:4:1) incubated in the presence of CD59/ILY^{WT} incubated at 37 °C for 1 h, to give (a) low surface coverage (with exposure of the bare lipid bilayer background) and (b) high surface coverage (where the background is saturated with CD59). At low surface coverage (a) , the ILY^{WT} pore is shown to occupy a height of ca. 7-8 nm above the exposed lipid bilayer surface. At high surface coverage (b), ILY^{WT} is ca. 5-6 nm above the background. The difference in height of ILY observed between high and low surface coverage is consistent with the height expected for a monolayer of CD59 (ca. 2 nm) that is present at high coverage.

At high surface coverage of CD59/ILY, as shown in *figure 6.6 (b)*, ILY oligomers are dispersed across the surface, albeit with significantly more arc shaped oligomers (that have been reported to form stable pores in membranes[172]) than complete rings, possibly due to the crowding upon the membrane surface preventing free diffusion that would facilitate complete oligomerisation. In addition, the background is saturated with molecules of the CD59 receptor, and thus the height the ILY oligomers can only be measured relative to a CD59 monolayer and not directly to the lipid bilayer membrane. The histogram of *z* data shows the ILY oligomers to occupy a height of ca. 5 nm relative to the CD59 monolayer, thus further demonstrating the ILY oligomers to be in the collapsed state, with the offset of 2 nm relative to the low coverage system shown in *6.6 (a)* consistent with the size of the CD59 molecule (as shown in *figure 6.5*).

6.2 Oligomerisation of intermedilysin in the absence of cholesterol

The mechanistic pathway of pore formation by the cholesterol-dependent cytolysins implicates cholesterol as a requirement for the formation of a transmembrane β-barrell pore[173]. However, in contrast to other CDC's, cholesterol is not the primary membrane receptor for ILY, which instead highjacks CD59 prior to pore formation[161]. As a member of the CDC family, ILY does require cholesterol in order to exhibit cytolytic activity, and therefore provides an interesting model system in which to study the mechanistic role of cholesterol as a membrane receptor (where here the role of the receptor is provided by CD59) vs. that of a promoter of the insertion transmembrane β-barrell. By measuring the height of the ILY oligomers in the absence of membrane cholesterol, it is possible to elucidate whether they are in the collapsed or uncollapsed (pre-pore) state, thus determining the point in the mechanistic pathway at which cholesterol is required for pore formation to progress.

Prior to insertion (to form a transmembrane pore), ILY oligomers are mobile upon the model membrane surface and are thus susceptible to being moved around the surface by the AFM probe during image acquisition. As a result, bound but mobile oligomers cannot be directly visualized but give rise to characteristic streaks in the image[164], as the oligomer is transiently attached to the AFM probe as it moves across the surface.

Previous AFM reports of the uncollapsed, pre-pore state (*via* a disulfide-locked mutant) show very high surface coverage[159], suggesting that AFM imaging is only possible for these mobile entities when the oligomers are 'jammed'[171] in place (i.e. without insertion into the membrane). Consistent with these previous observations of CDC's, AFM imaging of ILY in the absence of cholesterol (i.e. inhibiting formation of a transmembrane pore) was only successful where high surface coverage of the ILY oligomers occurred concurrently, as shown in *figure 6.7* below.

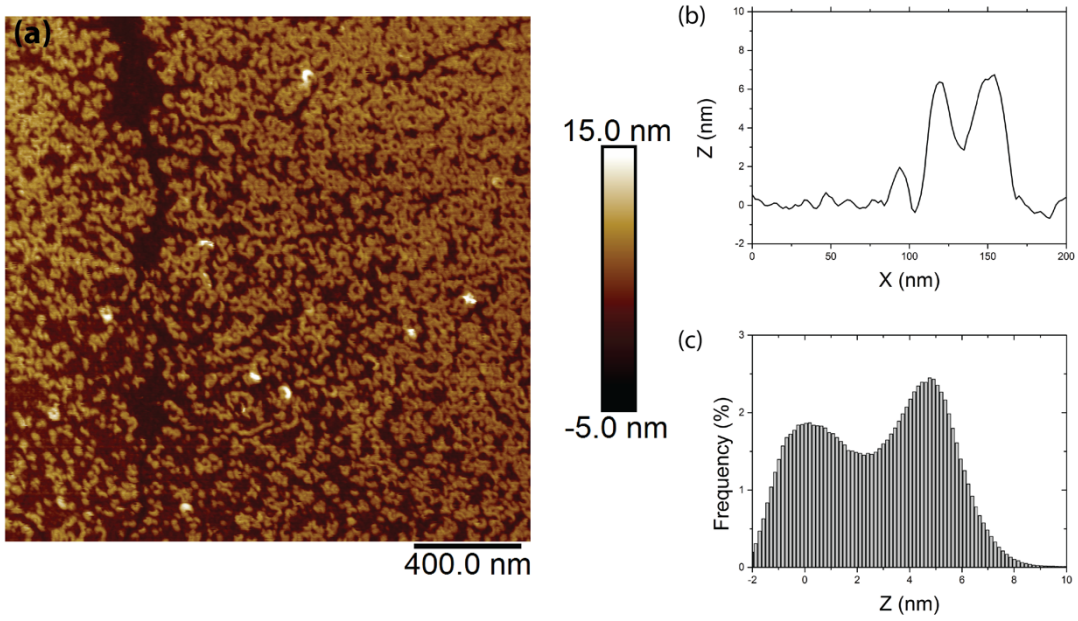

Figure 6.7: (a) AFM image showing the oligomerisation and collapse of ILY^{WT} in the absence of cholesterol, upon supported lipid bilayers composed of DOPC:DOPS (9:1). The cross-section and histogram of *z* data in (b) and (c) respectively show ILY^{WT} to occupy a height of ca. 5 nm above the background that is saturated with molecules of CD59, and is thus taken to be in the collapsed state in the absence of cholesterol.

The densely packed ILY oligomers shown in *figure 6.7* are shown to occupy a height of ca. 5 nm above the observable background that is taken to be saturated with molecules of CD59 (as observed for the systems containing cholesterol shown in *figure 6.5*), as can be seen in the histogram of *z* data. This observation implies that collapse from the pre-pore state occurs in the absence of membrane cholesterol, with collapse thus representing a distinct step in the mechanism of pore formation by intermedilysin. As the representative image in *figure 6.7* shows a single population (i.e. a single height)

occupied by the ILY oligomers, the pathway of pore formation (in the absence of cholesterol) can be considered to have reached its end point with collapse to the membrane. Temporal resolution of this process by AFM, in order to image a dual population of collapsed and uncollapsed states, presents a significant challenge as any uncollapsed state is inherently mobile upon the membrane surface, unless it is jammed in place by neighbouring oligomers. The clustering and jamming of such oligomers requires time to occur *via* diffusion, at which point a significant proportion of the oligomers have collapsed towards the membrane.

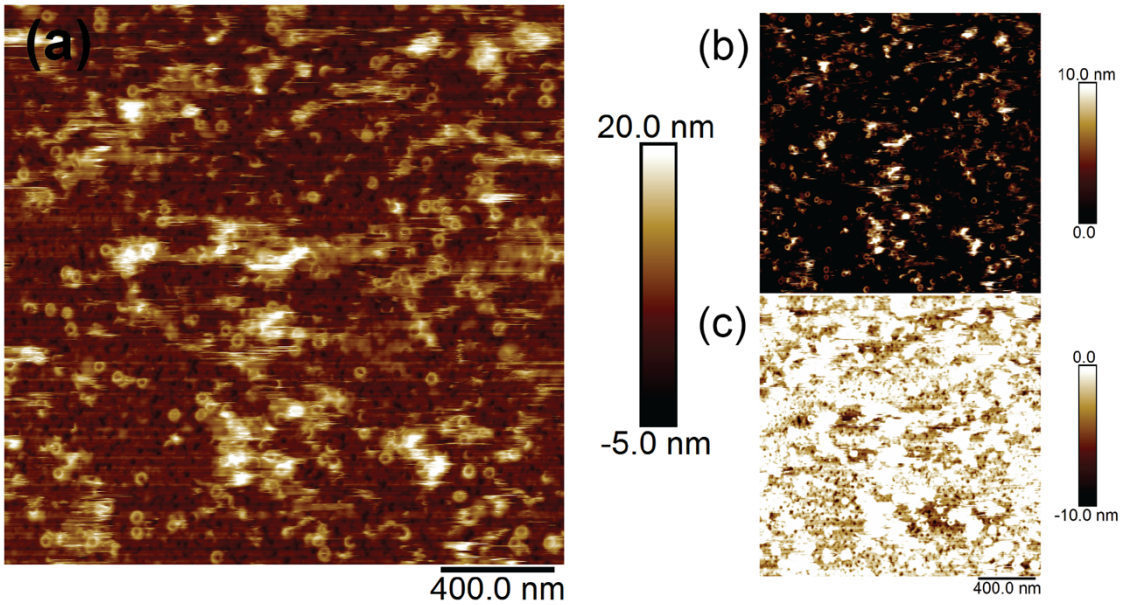

Figure 6.8: (a) AFM image of ILY^{WT} oligomers in the absence of cholesterol, in which a dual population of collapse and uncollapsed states can be observed. Images (b) and (c) are contrast adjusted to clearly show the (b) upper, uncollapsed state and (c) lower, collapsed state respectively.

The images shown in *figure 6.8* above capture a dual population of ILY^{WT} oligomers in the absence of membrane cholesterol, unequivocally showing that cholesterol is not required for ILY to undergo collapse. This represents a novel insight into the mechanism of perforation by intermedilysin in which it can be elucidated that the collapse and puncture of the lipid bilayer membranes represent two distinct steps, in which cholesterol is required only for the insertion of the transmembrane helices.

As the membrane surface is saturated with ILY oligomers, measurement of the uncollapsed state can only be obtained against a background of collapsed oligomers. Such measurements yield a value of ca. 4-5 nm from taking cross sections though individual pores, which is consistent with the distance of the transmembrane helices (TMH's) from the membrane surface prior to collapse. Rigorous analysis of the *z* data is compromised by quality of the images, where protein and lipid debris distorts the distributions in *z*. A measurement of the height of the uncollapsed states can be attained with 'locked' mutants against the lipid bilayer background[162].

6.3 Measuring the height of the uncollapsed, pre-pore state

In order to demonstrate that the ILY oligomer unambiguously undergoes a collapse from a higher pre-pore state in the absence of membrane cholesterol, a definite measurement of the height of a such a pre-pore state is required that does not require interpretation that implicates the membrane composition (i.e. the presence or absence of cholesterol). A means of making such a measurement is with the use mutants of the ILY monomers, which act to trap the ILY protein molecules either in their monomer state (that cannot undergo further oligomerisation; denoted ILY^{ML}) or in the pre-pore state (that cannot undergo collapse towards the membrane; denoted ILY^{PPL})[162]. Making AFM measurements of such mutants is problematic as both mutants are trapped at mechanistic stages prior to insertion into the lipid bilayer, and are thus mobile on the membrane surface. Visualization is therefore only possible when the mutant monomers and oligomers respectively aggregate upon the membrane surface.

6.3.1 Pre-pore locked mutant

As previously reported[162], ILY can be locked in the pre-pore state with the introduction of a disulfide bond that inhibits the structural collapse towards the membrane, achieved by mutating Glc-83 to Cys and Ser-217 to Cys. These ILY^{PPL} mutants readily oligomerise upon the membrane surface, as shown in the AFM image presented in *figure 6.9*, with jamming inhibiting diffusion and thus making the ILY^{PPL} clusters robust against the AFM probe. However, visualization was not routinely achieved, with a field of view containing both the uncollapsed, pre-pore state and the exposed lipid bilayer membrane

remaining elusive. As a result, the height difference between the apex of the ILY^{PPL} oligomer and the membrane surface cannot be extracted.

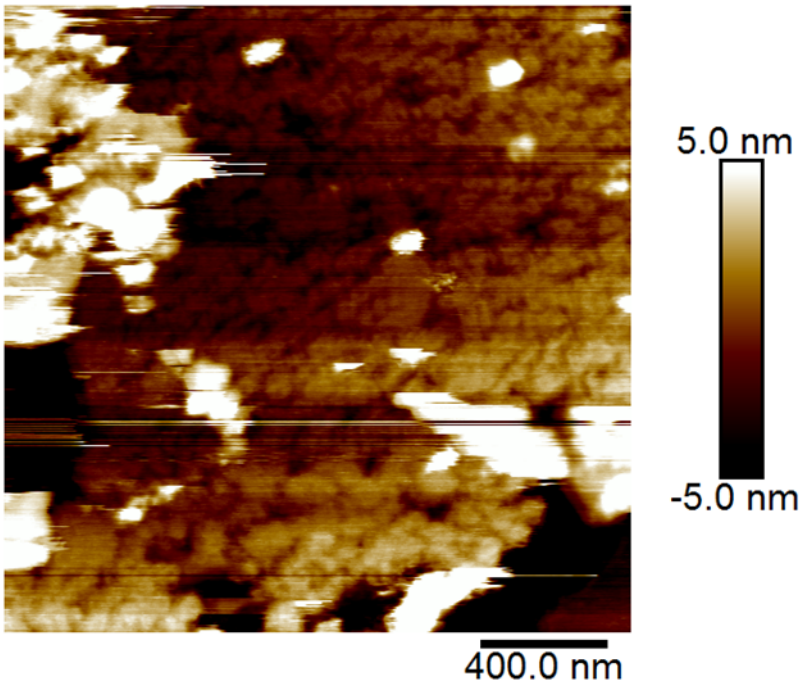

Figure 6.9: AFM image of aggregated oligomers of ILY^{PPL} that has been locked in the uncollapsed, pre-pore state. Protein and lipid debris upon the surface give low quality images from which it is not possible to extract the height difference between the apex of the ILY^{PPL} oligomers and the membrane surface.

6.3.2 Monomer locked mutant

In addition to mutating ILY to inhibit collapse, it can be similarly mutated to inhibit oligomerization by blocking its binding site with the introduction of a disulfide bond[162] (by mutating Thr-346 and Ile-361 to cysteine). Such a monomer-locked mutant can feasibly provide a measurement of the height of ILY above the membrane surface prior to collapse, provided that aggregation occurs in which the protein monomers are largely oriented perpendicular to the membrane surface, providing a clear edge that is easily visualized by AFM. As structural studies have shown that ILY binds to the membrane surface *via* the interface of domain 4 of ILY with the CD59 receptor[168] (as shown in *figure 6.2*), it is valid to assume that individual monomers are oriented perpendicular to the lipid bilayer surface.

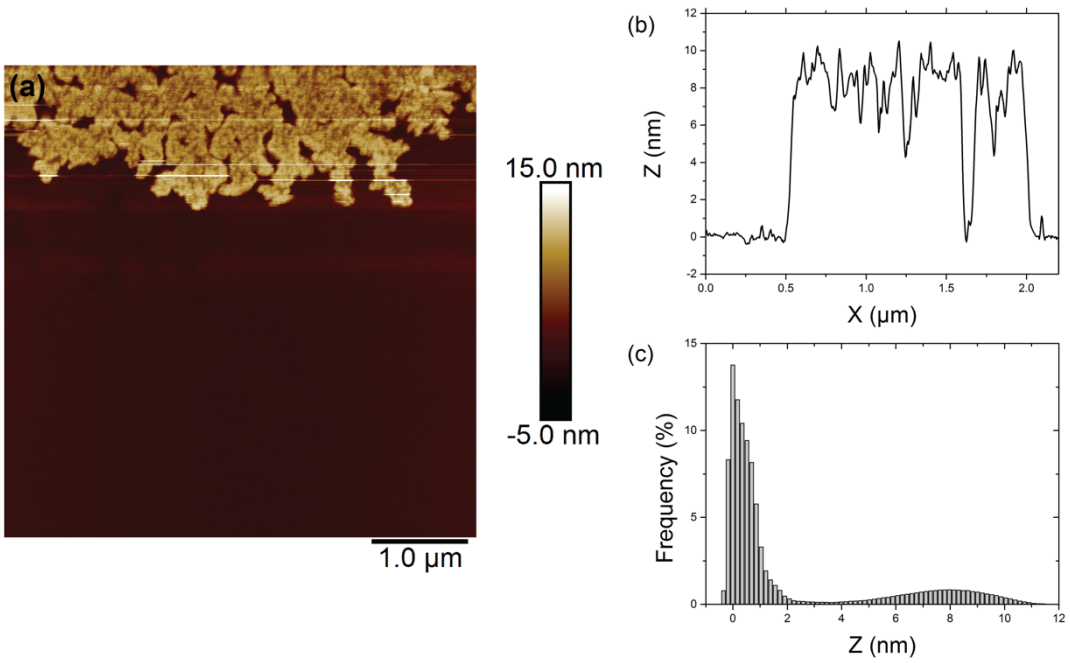

Figure 6.10: (a) AFM image and corresponding (b) cross sections and (c) *z* data of aggregates of monomer locked mutants of ILY. Sections through the ILY^{ML} aggregates *(b)* show that they reach heights of over 10 nm above the membrane surface, with the non-specific packing (observed as darker patches in *image (a)*) leading to a wide distribution of heights across the whole image, as seen in the histogram of *z* data in *(c)*.

Aggregates of ILY^{ML} were visualized by AFM, as shown in *figure 6.10* above, in which non-specific packing of the ILY^{ML} monomers gave rise to aggregates with a discontinuous morphology in which areas at lower heights are exposed. Cross-sections through the aggregates (as shown in *figure 6.10 (b)*) show the ILY^{ML} molecules to reach heights of over 10 nm above the membrane surface, whilst the distribution in *z* data is skewed to lower values owing to the non-specific packing of monomers leading to cracking within the aggregates that manifest themselves as pixels with lower *z* values. Similarly, the distribution in *z* corresponding to the membrane background is broad and asymmetric owing to the presence of bound CD59 molecules. Previous AFM experiments have shown a related CDC, perfringolysin, to decrease in height from 11 nm to 7 nm as the pre-pore collapses and inserts into the membrane[159], in which interpretation of the data is trivial as complete pores are visualized upon a membrane that is not compromised by the presence of additional receptors. The height of the monomer locked mutant, ILY^{ML}, is consistent with these previous observations with a

height that is taken to be ca. 10 nm above the membrane surface. The validity of this measurement is further enhanced by the observation of a dual population of collapsed and uncollapsed states (as shown in *figure 6.8*), which act to demonstrate the stepwise progression of pore formation by ILY.

6.4 Conclusions and outlook

The work presented in this chapter outlines the novel insight into the mechanism of perforation by intermedilysin that is gained with the application of AFM to model membrane systems. It is shown that cholesterol is not required for either membrane binding or collapse towards the membrane (cf. other CDC's), and therefore plays a vital role in the insertion of the the transmembrane helices in the formation of a β-barrel pore. It is demonstrated how AFM can provide an unprecedented view of the these biological surface processes, with visualization of the oligomeric pore and simultaneous measurement of its height above the lipid bilayer membrane. By understanding at which point along the pathway to pore formation that ILY becomes cytotoxic, interventions can be engineered to inhibit the formation of this toxic state.

These mechanistic insights into pore formation by intermedilysin could be further enhanced with the temporal resolution that is possible with the advent of high-speed AFM[81]. Despite the mobility of the ILY monomers upon the membrane surface, it is anticipated that sufficiently sensitive AFM[174] can yield time-lapse images on the order of minutes, where ILY can be tracked from its monomer state to that of a transmembrane pore. Additionally, high-resolution imaging can give unambiguous identification of the pore state if the AFM probe's apex is sharp enough to penetrate into the interior of the membrane pore; this is most likely achieved through the process of trial-and-error to find a super-sharp tip. Finally, if stable imaging of the pre-pore locked mutant (ILY^{PPL}) can be established, the addition of a reducing agent (i.e. DTT) can induce the transition from pre-pore to pore states[159], allowing for controlled imaging of this pore forming process.

Chapter 7: Conclusions and outlook

The aim of this thesis was to gain an insight into the physical phenomena at play in the lipid bilayer membrane by studying the structure and morphology model systems in which the molecular complexity is significantly reduced. The plasma membrane is comprised of an intricate mixture of lipids and proteins that adopts a dynamic, two-dimensional bilayer structure, and therefore mimicking such a complex system to unravel distinct molecular contributions often requires the rebuilding of the membrane from the bottom-up. The major theme running through the distinct chapters presented here is one of how the molecular subtleties of individual lipid species impacts upon bulk phase behavior, that is in turn extrapolated to an associated biological function; this is an established perspective[32] that continues to gain firm footing in the biophysical arena[175]. The common tool applied to these problems is atomic force microscopy, which is able to produce an unprecedented topographic view of the membrane surface with molecular resolution in a near-native aqueous environment. Additionally, AFM can probe the local mechanical properties of the membrane, with the possibility of access to individual ligand-receptor bonds[174,176]. It is demonstrated here how AFM can provide complimentary structural information to that which has previously be most readily obtained using reciprocal space scattering methodologies (i.e. SAXS), greatly enhancing our understanding of such structural motifs and thus our prospective ability to engineer model membranes to a given specification.

In *chapter 3*, phase-separated solid supported bilayers were studied as a model system that mimic the domains postulated to exist as 'lipid rafts' *in vivo*. The magnitude of the height mismatch at the domain boundary can be measured directly using AFM, and an associated line tension derived. By varying the length of the saturated lipids hydrocarbon chain, the height mismatch can be finely controlled and its effect upon domain size, morphology and lifetime can be observed concurrently. It is shown that increasing the height mismatch for 1:1:1 mixtures of saturated-PC:Chol:DPhPC gives an associated increase in line tension, that drives the formation of smaller, more circular domains, until the interactions between longer hydrocarbon chains dominate and

induce the formation of the gel phase. The use of complimentary calorimetric and scattering techniques (DSC and SAXS respectively), demonstrates an increase in the mixing/demixing temperatures of these three-component lipid systems upon increasing height mismatch[101]. A future direction would be to measure the height mismatch as it approaches the mixing/demixing temperature, along with simultaneous visualization of the domain morphology. Such studies would yield information on how transient domains may form with regulation provided by the height mismatch between the lipid species concerned. In addition, high-speed AFM maybe allow for the detection of fluctuating domains and therefore yield a further measurement of line tension in an analogous manner to the methodology that has been applied to domain fluctuations in GUVs[90].

The work presented in *chapter 4* follows the disruption of the sphingomyelin ripple phase with the addition of cholesterol and ceramide dopants. Sphingomyelin is thought to be found in close proximity to these dopants at local elevated concentrations *in vivo*, and therefore their molecular interactions likely manifest themselves in the global phase behavior of their two-component mixtures. As sphingomyelin/cholesterol complexes are implicated as lipid rafts[26], whilst ceramide is formed during apoptosis following the cleavage of the phosphate-linked headgroup from sphingomyelin[111], their molecular interactions are of biological significance. It is demonstrated that the ripple phase formed by sphingomyelin, that contains contributions from *fluid*- and *gel*-like regions in order to accommodate a periodic ripple, is disrupted *via* very different mechanism upon addition of a cholesterol or ceramide dopant. Cholesterol is thought to 'melt' the *gel*-like region of the ripple, with little increase in the ripple period as the bilayer tends towards the liquid-ordered phase. Conversely, ceramide adds to the *gel*-like region of the ripple, with a significant increase in ripple periodicity as the bilayer tends towards the gel-phase. As the disruption of the ripple phase appears on a local level, in a system in which the ripple coexists with planar gel globally, ensemble techniques are generally unsuitable for detecting the disruption of the ripple phase, with AFM providing a powerful local view. It is possible that an aligned lipid film would give rise to an enhanced SAXS peak that corresponds to the ripple period[118], opening up a possible means of tracking ripple

disruption with ensemble methods. The AFM experiments presented here would be consolidated by specifying the thermal history of the sphingomyelin ripple with heating and cooling cycles around the gel-fluid transition *in situ*. If further AFM experiments prove problematic, electron microscopy could provide an alternate means of viewing the local bilayer structure.

Chapter 5 demonstrates the viability of forming films of inverse lipids phases with a view to imaging their terminating structure at the aqueous interface. By resolving the structure of the three-dimensional lattice along its terminating plane, a knowledge of how the bulk structure reconstructs itself at the interface will be gained, informing our understanding in engineering inverse phases for drug delivery and membrane protein crystallization. The 'soft' nature of these inverse lipids films, in addition to the requirement of visualization on the scale of their repeating lattice, makes AFM imaging technically challenging; it is anticipated that more sensitive AFM is required, which would be further enhanced by the known alignment of the lipid film provided by surface scattering studies[144]. For these specific experiments, combined AFM-GISAXS beamtime is scheduled at the ESRF in *July 2016*, and thus cannot inform the preliminary studies presented here.

Chapter 6 extends the complexity of the model membrane system with the addition of a pore-forming protein toxin, ILY. This macromolecular machinery remodels the lipid bilayer with the formation of a ca. 30 nm pore, stabilized by a β-barrel at the membrane interface. Upon formation of a membrane pore, a vertical collapse of the ILY complex occurs, which lends itself to investigation by AFM. By following the formation of the ILY pore in the absence and presence of cholesterol, it is shown that cholesterol is required for puncture of the membrane, but the collapse towards the membrane represents a separate mechanistic step for which cholesterol is not required. An interesting avenue for future study would be in furthering our understanding of how membrane composition affects the pathway of pore formation, where the model membrane can be tuned to increase the degree of stored curvature elastic stress with the introduction of type I lipids such as DOPE. This would allow us to unravel how the membrane lipids

play an active role in the mechanism of pore formation, where the role of the pore forming protein could additionally be that of a mechanosensor.

An obvious improvement to all of the studies presented here, which would significantly extend the scope of these experimental systems, would be the fine control over the temperature of the AFM. As the phase behavior of lyotropic lipid systems often displays dramatic structural perturbations around physiological temperatures, control over the temperature would allow for a less ambiguous interpretation of the lipid system through imaging alone, and could also be used as a thermodynamic trigger in inducing a phase change or in altering the rate of oligomerisation towards the formation of a protein pore. Variable-temperature AFM introduces a degree of instrumental drift to system, but for those length scales addressed here, allowing for equilibration of the system upon changing temperatures will limit the impact upon the resolution attainable. Such temperature control is readily available[10,134], albeit at significant cost, which could not be met for this project. It is however important to note that variation in the temperature is not a panacea, with AFM experiments of soft matter systems made viable mainly in our ability to construct the model membrane systems from the bottom-up, thus allowing for topographic imaging to take place. The step-by-step construction of a supported model membrane is an iterative process that requires delicate operation of the AFM; a significant technical challenge that is inherently resource intensive. The groundwork has been laid for the construction of the model membranes presented in this thesis, with future studies of these likely capitalizing on the instrumental capabilities of external facilities.

It is likely that the future study of model membrane systems, such as those presented in this thesis, will be most significantly extended by developments in instrumentation that allow access to higher spatial and temporal resolution[80], multiparametric imaging modes[174] and simultaneous collection of AFM data with a secondary optical or scattering methodology[144] (e.g. TIRF, GISAXS etc.). Many of these technologies mentioned are becoming more widely adopted as such instruments reach commercialization, with high-speed AFM paving the way for a spectacular view of biomolecular processes in real time[70]. Most importantly, to extend the study of model membranes to systems which

most closely resemble the native plasma membrane, the interplay of lipids with membrane proteins must be accounted for, which requires a critical mass of expertise spanning biology, chemistry and physics. As the model membrane tends towards the crowded environment of the plasma membrane *in vivo*, the complexity of the system is greatly increased, although it is likely that many of the principles gained from studying simple systems, such as those discussed here, will remain valid.

Appendix

All raw AFM and DSC data included in this thesis can be found at:

https://www.dropbox.com/sh/4en1tz02kimw659/AADvFwwZUnpx_9SARBhFVhf7a?dl=0

This above link also provides access to Nanoscope Analysis software that can be used to used to view and process AFM images.

Bibliography

1. Singer, S. J. & Nicolson, G. L. The fluid mosaic model of the structure of cell membranes. *Science* **175,** 720–731 (1972).
2. Marguet, D., Lenne, P.-F., Rigneault, H. & He, H.-T. Dynamics in the plasma membrane: how to combine fluidity and order. *EMBO J.* **25,** 3446–3457 (2006).
3. Smith, A. S., Sengupta, K., Goennenwein, S., Seifert, U. & Sackmann, E. Force-induced growth of adhesion domains is controlled by receptor mobility. *Proc. Natl. Acad. Sci. U.S.A.* **105,** 6906–6911 (2008).
4. Engelman, D. M. Membranes are more mosaic than fluid. *Nature* **438,** 578–580 (2005).
5. Lingwood, D. & Simons, K. Lipid rafts as a membrane-organizing principle. *Science* **327,** 46–50 (2010).
6. Simons, K. & Ikonen, E. Functional rafts in cell membranes. *Nature* (1997).
7. Hancock, J. F. Lipid rafts: contentious only from simplistic standpoints. *Nature Reviews Molecular Cell Biology* **7,** 456–462 (2006).
8. Eggeling, C. *et al.* Direct observation of the nanoscale dynamics of membrane lipids in a living cell. *Nature* **457,** 1159–1162 (2009).
9. Veatch, S. L. & Keller, S. L. Separation of Liquid Phases in Giant Vesicles of Ternary Mixtures of Phospholipids and Cholesterol. *Biophysical Journal* **85,** 3074–3083 (2003).
10. Connell, S. D., Heath, G., Olmsted, P. D. & Kisil, A. Critical point fluctuations in supported lipid membranes. *Faraday Discussions* **161,** 91–111 (2013).
11. Yuan, C., Furlong, J., Burgos, P. & Johnston, L. J. The Size of Lipid Rafts: An Atomic Force Microscopy Study of Ganglioside GM1 Domains in Sphingomyelin/DOPC/Cholesterol Membranes. *Biophysical Journal* **82,** 2526–2535 (2002).
12. Tayebi, L. *et al.* Long-range interlayer alignment of intralayer domains in stacked lipid bilayers. *Nat Mater* **11,** 1074–1080 (2012).
13. Uppamoochikkal, P., Tristram-Nagle, S. & Nagle, J. F. Orientation of Tie-Lines in the Phase Diagram of DOPC/DPPC/Cholesterol Model Biomembranes. *Langmuir* **26,** 17363–17368 (2010).
14. Ces, O. & Mulet, X. Physical coupling between lipids and proteins: a paradigm for cellular control. *Signal Transduction* **6,** 112–132 (2006).
15. Bennett, W. F. D., Sapay, N. & Tieleman, D. P. Atomistic Simulations of Pore Formation and Closure in Lipid Bilayers. *Biophysical Journal* **106,** 210–219 (2014).
16. Sanyal, S. & Menon, A. K. Flipping Lipids: Why an' What's the Reason for? *ACS Chemical Biology* **4,** 895–909 (2009).
17. Chen, Y. A. & Scheller, R. H. SNARE-mediated membrane fusion. *Nature Reviews Molecular Cell Biology* **2,** 98–106 (2001).

18. Chiaruttini, N. *et al.* Relaxation of Loaded ESCRT-III Spiral Springs Drives Membrane Deformation. *Cell* **163,** 866–879 (2015).
19. Gilbert, R. J. C., Dalla Serra, M., Froelich, C. J., Wallace, M. I. & Anderluh, G. Membrane pore formation at protein-lipid interfaces. *Trends Biochem. Sci.* **39,** 510–516 (2014).
20. Daleke, D. L. Phospholipid flippases. *J. Biol. Chem.* **282,** 821–825 (2007).
21. Shevchenko, A. & Simons, K. Lipidomics: coming to grips with lipid diversity. *Nature Reviews Molecular Cell Biology* **11,** 593–598 (2010).
22. van Meer, G., Voelker, D. R. & Feigenson, G. W. Membrane lipids: where they are and how they behave. *Nature Reviews Molecular Cell Biology* **9,** 112–124 (2008).
23. van Meer, G. Cellular lipidomics. *EMBO J.* **24,** 3159–3165 (2005).
24. van Meer, G. & de Kroon, A. I. P. M. Lipid map of the mammalian cell. *J. Cell. Sci.* **124,** 5–8 (2011).
25. Holthuis, J. C., Pomorski, T., Raggers, R. J., Sprong, H. & van Meer, G. The organizing potential of sphingolipids in intracellular membrane transport. *Physiol. Rev.* **81,** 1689–1723 (2001).
26. McIntosh, T. J., Simon, S. A., Needham, D. & Huang, C. H. Structure and cohesive properties of sphingomyelin/cholesterol bilayers. *Biochemistry* **31,** 2012–2020 (1992).
27. Subczynski, W. K., Wisniewska, A., Yin, J. J., Hyde, J. S. & Kusumi, A. Hydrophobic barriers of lipid bilayer membranes formed by reduction of water penetration by alkyl chain unsaturation and cholesterol. *Biochemistry* **33,** 7670–7681 (1994).
28. Brooks, N. J. *et al.* Thermotropic and lyotropic liquid crystalline phases of Guerbet branched-chain -D-glucosides. *Liquid Crystals* **38,** 1725–1734 (2011).
29. Tyler, A. I. I. *et al.* Hydrostatic pressure effects on a hydrated lipid inverse micellar Fd 3 m cubic phase. *Physical Chemistry Chemical Physics* **13,** 3033–3038 (2011).
30. Kulkarni, C. V., Wachter, W., Iglesias-Salto, G., Engelskirchen, S. & Ahualli, S. Monoolein: a magic lipid? *Phys Chem Chem Phys* **13,** 3004–3021 (2011).
31. Israelachvili, J. N. *Intermolecular and surface forces: with applications to colloidal and biological systems (Colloid Science)*. (1992).
32. Seddon, J. M. Structure of the inverted hexagonal (HII) phase, and non-lamellar phase transitions of lipids. *Biochimica et Biophysica Acta (BBA) - Reviews on Biomembranes* **1031,** 1–69 (1990).
33. Charalambous, K. *et al.* Engineering de novo membrane-mediated protein-protein communication networks. *Journal of the American Chemical Society* **134,** 5746–5749 (2012).
34. Shearman, G. C., Ces, O., Templer, R. H. & Seddon, J. M. Inverse lyotropic phases of lipids and membrane curvature. *J Phys Condens Matter* **18,** S1105–24 (2006).
35. Shearman, G. C. *et al.* A 3-D hexagonal inverse micellar lyotropic phase. *Journal of the American Chemical Society* **131,** 1678–1679 (2009).

36. Seddon, J. M. An inverse face-centered cubic phase formed by diacylglycerol-phosphatidylcholine mixtures. *Biochemistry* **29,** 7997–8002 (1990).
37. Conn, C. E. & Drummond, C. J. Nanostructured bicontinuous cubic lipid self-assembly materials as matrices for protein encapsulation. *Soft Matter* **9,** 3449–3464 (2013).
38. Templer, R. H., Seddon, J. M., Duesing, P. M., Winter, R. & Erbes, J. Modeling the Phase Behavior of the Inverse Hexagonal and Inverse Bicontinuous Cubic Phases in 2:1 Fatty Acid/Phosphatidylcholine Mixtures. *J. Phys. Chem. B* **102,** 7262–7271 (1998).
39. Tyler, A. I. I. *et al.* Electrostatic swelling of bicontinuous cubic lipid phases. *Soft Matter* **11,** 3279–3286 (2015).
40. Landau, E. M. & Rosenbusch, J. P. Lipidic cubic phases: a novel concept for the crystallization of membrane proteins. *Proceedings of the National Academy of Sciences* **93,** 14532–14535 (1996).
41. Richardson, S. J. *et al.* Aligned platinum nanowire networks from surface-oriented lipid cubic phase templates. *Nanoscale* **8,** 2850–2856 (2016).
42. Nagle, J. F. Introductory Lecture: Basic quantities in model biomembranes. *Faraday Discussions* **161,** 11–29 (2013).
43. Evans, E., Rawicz, W. & Smith, B. A. Concluding remarks Back to the future: mechanics and thermodynamics of lipid biomembranes. *Faraday Discuss.* **161,** 591–611 (2013).
44. Helfrich, W. Elastic properties of lipid bilayers: theory and possible experiments. *Z Naturforsch C* **28,** 693–703 (1973).
45. Pan, J., Tristram-Nagle, S., Kučerka, N. & Nagle, J. F. Temperature Dependence of Structure, Bending Rigidity, and Bilayer Interactions of Dioleoylphosphatidylcholine Bilayers. *Biophysical Journal* **94,** 117–124 (2008).
46. Korlach, J., Schwille, P., Webb, W. W. & Feigenson, G. W. Characterization of lipid bilayer phases by confocal microscopy and fluorescence correlation spectroscopy. *Proceedings of the National Academy of Sciences* **96,** 8461–8466 (1999).
47. Grélard, A., Loudet, C., Diller, A. & Dufourc, E. J. in *Membrane Protein Structure Determination* **654,** 341–359 (Humana Press, 2010).
48. Mabrey, S. & Sturtevant, J. M. Investigation of phase transitions of lipids and lipid mixtures by sensitivity differential scanning calorimetry. *Proceedings of the National Academy of Sciences* **73,** 3862–3866 (1976).
49. Karamdad, K., Law, R. V., Seddon, J. M., Brooks, N. J. & Ces, O. Studying the effects of asymmetry on the bending rigidity of lipid membranes formed by microfluidics. *Chem. Commun. (Camb.)* **52,** 5277–5280 (2016).
50. Baumgart, T., Hess, S. T. & Webb, W. W. Imaging coexisting fluid domains in biomembrane models coupling curvature and line tension. *Nature* **425,** 821–824 (2003).

51. Rautu, S. A. *et al.* The Role of Optical Projection in the Analysis of Membrane Fluctuations. (2015).
52. Evans, E. & Rawicz, W. Entropy-driven tension and bending elasticity in condensed-fluid membranes. *Physical Review Letters* **64,** 2094–2097 (1990).
53. Czogalla, A., Franquelim, H. G. & Schwille, P. DNA Nanostructures on Membranes as Tools for Synthetic Biology. *Biophysical Journal* **110,** 1698–1707 (2016).
54. Bigay, J., Gounon, P., Robineau, S. & Antonny, B. Lipid packing sensed by ArfGAP1 couples COPI coat disassembly to membrane bilayer curvature. *Nature* **426,** 563–566 (2003).
55. Holden, M. A., Needham, D. & Bayley, H. Functional bionetworks from nanoliter water droplets. *Journal of the American Chemical Society* **129,** 8650–8655 (2007).
56. Needham, D. Lipid structures: a brief history of multisomes. *Nature Nanotechnology* **6,** 761–762 (2011).
57. Hwang, W. L., Chen, M., Cronin, B., Holden, M. A. & Bayley, H. Asymmetric droplet interface bilayers. *Journal of the American Chemical Society* **130,** 5878–5879 (2008).
58. Rojko, N. *et al.* Imaging the lipid-phase-dependent pore formation of equinatoxin II in droplet interface bilayers. *Biophysical Journal* **106,** 1630–1637 (2014).
59. de Wit, G., Danial, J. S. H., Kukura, P. & Wallace, M. I. Dynamic label-free imaging of lipid nanodomains. *Proc. Natl. Acad. Sci. U.S.A.* **112,** 12299–12303 (2015).
60. Richter, R. P., Bérat, R. & Brisson, A. R. Formation of Solid-Supported Lipid Bilayers: An Integrated View. *Langmuir* **22,** 3497–3505 (2006).
61. Castellana, E. T. & Cremer, P. S. Solid supported lipid bilayers: From biophysical studies to sensor design. *Surface Science Reports* **61,** 429–444 (2006).
62. Sackmann, E. Supported membranes: scientific and practical applications. *Science* **271,** 43–48 (1996).
63. Peng, J. B., Prakash, M., Macdonald, R., Dutta, P. & Ketterson, J. B. Formation of multilayers of dipalmitoylphosphatidylcholine using the Langmuir-Blodgett technique. *Langmuir* **3,** 1096–1097 (2002).
64. Kalb, E., Frey, S. & Tamm, L. K. Formation of supported planar bilayers by fusion of vesicles to supported phospholipid monolayers. *Biochim. Biophys. Acta* **1103,** 307–316 (1992).
65. and, U. M. & Salditt, T. Preparation of Solid-Supported Lipid Bilayers by Spin-Coating. *Langmuir* **18,** 8172–8177 (2002).
66. Binnig, G., Rohrer, H., Gerber, C. & Weibel, E. Surface Studies by Scanning Tunneling Microscopy. *Physical Review Letters* **49,** 57–61 (1982).
67. Binnig, G., Quate, C. F. & Gerber, C. Atomic Force Microscope. *Physical Review Letters* **56,** 930–933 (1986).
68. Leung, C. *et al.* Atomic force microscopy with nanoscale cantilevers resolves different structural conformations of the DNA double helix. *Nano Lett.* **12,** 3846–

3850 (2012).

69. Rico, F., Gonzalez, L., Casuso, I., Puig-Vidal, M. & Scheuring, S. High-speed force spectroscopy unfolds titin at the velocity of molecular dynamics simulations. *Science* **342,** 741–743 (2013).
70. Kodera, N., Yamamoto, D., Ishikawa, R. & Ando, T. Video imaging of walking myosin V by high-speed atomic force microscopy. *Nature* **468,** 72–76 (2010).
71. Giocondi, M.-C. *et al.* Surface topography of membrane domains. *Biochimica et Biophysica Acta (BBA) - Biomembranes* **1798,** 703–718 (2010).
72. Sheikh, K. H., Giordani, C., Kilpatrick, J. I. & Jarvis, S. P. Direct submolecular scale imaging of mesoscale molecular order in supported dipalmitoylphosphatidylcholine bilayers. *Langmuir* **27,** 3749–3753 (2011).
73. Sheikh, K. H. & Jarvis, S. P. Crystalline hydration structure at the membrane-fluid interface of model lipid rafts indicates a highly reactive boundary region. *Journal of the American Chemical Society* **133,** 18296–18303 (2011).
74. Mingeot-Leclercq, M.-P., Deleu, M., Brasseur, R. & Dufrêne, Y. F. Atomic force microscopy of supported lipid bilayers. *Nature Protocols* **3,** 1654–1659 (2008).
75. Hodel, A. W., Leung, C., Dudkina, N. V., Saibil, H. R. & Hoogenboom, B. W. Atomic force microscopy of membrane pore formation by cholesterol dependent cytolysins. *Current Opinion in Structural Biology* **39,** 8–15 (2016).
76. Müller, D. J. & Dufrêne, Y. F. Atomic force microscopy: a nanoscopic window on the cell surface. *Trends Cell Biol.* **21,** 461–469 (2011).
77. Garcia-Manyes, S., Redondo-Morata, L., Oncins, G. & Sanz, F. Nanomechanics of Lipid Bilayers: Heads or Tails? *Journal of the American Chemical Society* **132,** 12874–12886 (2010).
78. Garcia-Manyes, S., Oncins, G. & Sanz, F. Effect of ion-binding and chemical phospholipid structure on the nanomechanics of lipid bilayers studied by force spectroscopy. *Biophysical Journal* **89,** 1812–1826 (2005).
79. Picas, L., Rico, F. & Scheuring, S. Direct measurement of the mechanical properties of lipid phases in supported bilayers. *Biophysical Journal* **102,** L01–3 (2012).
80. Ando, T. High-speed atomic force microscopy coming of age. *Nanotechnology* **23,** 062001 (2012).
81. Casuso, I. *et al.* Characterization of the motion of membrane proteins using high-speed atomic force microscopy. *Nature Nanotech* **7,** 525–529 (2012).
82. Butt, H.-J., Cappella, B. & Kappl, M. Force measurements with the atomic force microscope: Technique, interpretation and applications. *Surface Science Reports* **59,** 1–152 (2005).
83. Horcas, I. *et al.* WSXM: a software for scanning probe microscopy and a tool for nanotechnology. *Rev Sci Instrum* **78,** 013705 (2007).
84. Brooks, N. J. *et al.* Automated high pressure cell for pressure jump x-ray diffraction. *Rev Sci Instrum* **81,** 064103 (2010).

85. Day, C. A. & Kenworthy, A. K. Tracking microdomain dynamics in cell membranes. *Biochim. Biophys. Acta* **1788,** 245–253 (2009).
86. Mouritsen, O. G. The liquid-ordered state comes of age. *Biochimica et Biophysica Acta (BBA) - Biomembranes* **1798,** 1286–1288 (2010).
87. Quinn, P. J. & Wolf, C. The liquid-ordered phase in membranes. *Biochimica et Biophysica Acta (BBA) - Biomembranes* **1788,** 33–46 (2009).
88. Filippov, A., Orädd, G. & Lindblom, G. Lipid Lateral Diffusion in Ordered and Disordered Phases in Raft Mixtures. *Biophysical Journal* **86,** 891–896 (2004).
89. de Meyer, F. & Smit, B. Effect of cholesterol on the structure of a phospholipid bilayer. *Proceedings of the National Academy of Sciences* **106,** 3654–3658 (2009).
90. Honerkamp-Smith, A. R. *et al.* Line tensions, correlation lengths, and critical exponents in lipid membranes near critical points. *Biophysical Journal* **95,** 236–246 (2008).
91. Bleecker, J. V. *et al.* Thickness Mismatch of Coexisting Liquid Phases in Noncanonical Lipid Bilayers. *J. Phys. Chem. B* **120,** 2761–2770 (2016).
92. Kuzmin, P. I., Akimov, S. A., Chizmadzhev, Y. A., Zimmerberg, J. & Cohen, F. S. Line tension and interaction energies of membrane rafts calculated from lipid splay and tilt. *Biophysical Journal* **88,** 1120–1133 (2005).
93. Heberle, F. A. *et al.* Bilayer Thickness Mismatch Controls Domain Size in Model Membranes. *Journal of the American Chemical Society* **135,** 6853–6859 (2013).
94. García-Sáez, A. J., Chiantia, S. & Schwille, P. Effect of line tension on the lateral organization of lipid membranes. *J. Biol. Chem.* **282,** 33537–33544 (2007).
95. Hassan-Zadeh, E., Baykal-Caglar, E., Alwarawrah, M. & Huang, J. Complex roles of hybrid lipids in the composition, order, and size of lipid membrane domains. *Langmuir* **30,** 1361–1369 (2014).
96. Palmieri, B., Grant, M. & Safran, S. A. Prediction of the dependence of the line tension on the composition of linactants and the temperature in phase separated membranes. *Langmuir* **30,** 11734–11745 (2014).
97. Fowler, P. W., Williamson, J. J., Sansom, M. S. P. & Olmsted, P. D. Roles of Interleaflet Coupling and Hydrophobic Mismatch in Lipid Membrane Phase-Separation Kinetics. *Journal of the American Chemical Society* **138,** 11633–11642 (2016).
98. Williamson, J. J. & Olmsted, P. Kinetics of Registration, Antiregistration, and Flip-Flop in Phase-Separating Bilayers. *Biophysical Journal* (2016).
99. Williamson, J. J. & Olmsted, P. D. Registered and Antiregistered Phase Separation of Mixed Amphiphilic Bilayers. *Biophysical Journal* **108,** 1963–1976 (2015).
100. Milovanovic, D. *et al.* Hydrophobic mismatch sorts SNARE proteins into distinct membrane domains. *Nature Communications* **6,** 5984 (2015).
101. Bleecker, J. V., Cox, P. A. & Keller, S. L. Mixing Temperatures of Bilayers Not Simply Related to Thickness Differences between Lo and Ld Phases. *Biophysical Journal* **110,** 2305–2308 (2016).

102. Hung, W. C., Chen, F. Y. & Huang, H. W. Order–disorder transition in bilayers of diphytanoyl phosphatidylcholine. *Biochimica et Biophysica Acta (BBA) - Biomembranes* **1467,** 198–206 (2000).
103. Ladha, S. *et al.* Lateral diffusion in planar lipid bilayers: a fluorescence recovery after photobleaching investigation of its modulation by lipid composition, cholesterol, or alamethicin content and divalent cations. *Biophysical Journal* **71,** 1364–1373 (1996).
104. Lin, W.-C., Blanchette, C. D., Ratto, T. V. & Longo, M. L. Lipid asymmetry in DLPC/DSPC-supported lipid bilayers: a combined AFM and fluorescence microscopy study. *Biophysical Journal* **90,** 228–237 (2006).
105. Butt, H.-J. & Franz, V. Rupture of molecular thin films observed in atomic force microscopy. I. Theory. *Phys. Rev. E* **66,** 031601 (2002).
106. Loi, S., Sun, G., Franz, V. & Butt, H.-J. Rupture of molecular thin films observed in atomic force microscopy. II. Experiment. *Phys Rev E Stat Nonlin Soft Matter Phys* **66,** 031602 (2002).
107. Künneke, S., Krüger, D. & Janshoff, A. Scrutiny of the Failure of Lipid Membranes as a Function of Headgroups, Chain Length, and Lamellarity Measured by Scanning Force Microscopy. *Biophysical Journal* **86,** 1545–1553 (2004).
108. Leckband, D. The surface force apparatus ? a tool for probing molecular protein interactions. *Nature* **376,** 617–618 (1995).
109. Hannun, Y. A. & Obeid, L. M. Principles of bioactive lipid signalling: lessons from sphingolipids. *Nature Reviews Molecular Cell Biology* **9,** 139–150 (2008).
110. Slotte, J. P. & Ramstedt, B. The functional role of sphingomyelin in cell membranes. *Eur. J. Lipid Sci. Technol.* **109,** 977–981 (2007).
111. Pettus, B. J., Chalfant, C. E. & Hannun, Y. A. Ceramide in apoptosis: an overview and current perspectives. *Biochim. Biophys. Acta* **1585,** 114–125 (2002).
112. Mannock, D. A., McIntosh, T. J., Jiang, X., Covey, D. F. & McElhaney, R. N. Effects of Natural and Enantiomeric Cholesterol on the Thermotropic Phase Behavior and Structure of Egg Sphingomyelin Bilayer Membranes. *Biophysical Journal* **84,** 1038–1046 (2003).
113. Shipley, G. G., Avecilla, L. S. & Small, D. M. Phase behavior and structure of aqueous dispersions of sphingomyelin. *J. Lipid Res.* **15,** 124–131 (1974).
114. de Vries, A. H., Yefimov, S., Mark, A. E. & Marrink, S. J. Molecular structure of the lecithin ripple phase. *Proc. Natl. Acad. Sci. U.S.A.* **102,** 5392–5396 (2005).
115. Nagle, J. F. & Tristram-Nagle, S. Structure of lipid bilayers. *Biochimica et Biophysica Acta (BBA)-Reviews …* (2000).
116. Rappolt, M. *et al.* New evidence for gel-liquid crystalline phase coexistence in the ripple phase of phosphatidylcholines. *Eur Biophys J* **29,** 125–133 (2000).
117. Sengupta, K., Raghunathan, V. A. & Katsaras, J. Structure of the ripple phase of phospholipid multibilayers. *Phys. Rev. E* **68,** 031710 (2003).

118. Akabori, K. & Nagle, J. F. Structure of the DMPC lipid bilayer ripple phase. *Soft Matter* **11,** 918–926 (2015).
119. Shaw, K. P. *et al.* Pressure–temperature phase behaviour of natural sphingomyelin extracts. *Soft Matter* **8,** 1070–1078 (2012).
120. Leidy, C., Mouritsen, O. G., Jørgensen, K. & Peters, G. H. Evolution of a Rippled Membrane during Phospholipase A2 Hydrolysis Studied by Time-Resolved AFM. *Biophysical Journal* **87,** 408–418 (2004).
121. Mou, J., Yang, J. & Shao, Z. Tris(hydroxymethyl)aminomethane (C4H11NO3) induced a ripple phase in supported unilamellar phospholipid bilayers. *Biochemistry* **33,** 4439–4443 (1994).
122. Leidy, C., Kaasgaard, T., Crowe, J. H., Mouritsen, O. G. & Jørgensen, K. Ripples and the Formation of Anisotropic Lipid Domains: Imaging Two- Component Supported Double Bilayers by Atomic Force Microscopy. *Biophysical Journal* **83,** 2625–2633 (2002).
123. Heimburg, T. A Model for the Lipid Pretransition: Coupling of Ripple Formation with the Chain-Melting Transition. *Biophysical Journal* **78,** 1154–1165 (2000).
124. Quinn, P. J. Structure of Sphingomyelin Bilayers and Complexes with Cholesterol Forming Membrane Rafts. *Langmuir* **29,** 9447–9456 (2013).
125. Lewis, R. N. A. H., Mannock, D. A. & McElhaney, R. N. Differential scanning calorimetry in the study of lipid phase transitions in model and biological membranes: practical considerations. *Methods Mol. Biol.* **400,** 171–195 (2007).
126. Filippov, A., Orädd, G. & Lindblom, G. Sphingomyelin structure influences the lateral diffusion and raft formation in lipid bilayers. *Biophysical Journal* **90,** 2086–2092 (2006).
127. Shah, J. *et al.* Structural and thermotropic properties of synthetic C16:0 (palmitoyl) ceramide: effect of hydration. *J. Lipid Res.* **36,** 1936–1944 (1995).
128. Chiu. Differential scanning calorimetry: An invaluable tool for a detailed thermodynamic characterization of macromolecules and their interactions. *Journal of Pharmacy And Bioallied Sciences* **3,** 39–59 (2011).
129. Veiga, M. P., Arrondo, J. L., Goñi, F. M. & Alonso, A. Ceramides in phospholipid membranes: effects on bilayer stability and transition to nonlamellar phases. *Biophysical Journal* **76,** 342–350 (1999).
130. Sot, J., Aranda, F. J., Collado, M.-I., Goñi, F. M. & Alonso, A. Different effects of long- and short-chain ceramides on the gel-fluid and lamellar-hexagonal transitions of phospholipids: a calorimetric, NMR, and x-ray diffraction study. *Biophysical Journal* **88,** 3368–3380 (2005).
131. Yao, H., Matuoka, S., Tenchov, B. & Hatta, I. Metastable ripple phase of fully hydrated dipalmitoylphosphatidylcholine as studied by small angle x-ray scattering. *Biophysical Journal* **59,** 252–255 (1991).
132. Brooks, N. J., Ces, O., Templer, R. H. & Seddon, J. M. Pressure effects on lipid

membrane structure and dynamics. *Chem. Phys. Lipids* **164,** 89–98 (2011).

133. Barriga, H. M. G. *et al.* Pressure–Temperature Phase Behavior of Mixtures of Natural Sphingomyelin and Ceramide Extracts. *Langmuir* **31,** 3678–3686 (2015).
134. Kaasgaard, T., Leidy, C., Crowe, J. H., Mouritsen, O. G. & Jørgensen, K. Temperature-Controlled Structure and Kinetics of Ripple Phases in One- and Two-Component Supported Lipid Bilayers. *Biophysical Journal* **85,** 350–360 (2003).
135. Chachaty, C., Rainteau, D., Tessier, C., Quinn, P. J. & Wolf, C. Building up of the liquid-ordered phase formed by sphingomyelin and cholesterol. *Biophysical Journal* **88,** 4032–4044 (2005).
136. Akbar, S., Elliott, J. M., Rittman, M. & Squires, A. M. Facile production of ordered 3D platinum nanowire networks with 'single diamond' bicontinuous cubic morphology. *Adv. Mater. Weinheim* **25,** 1160–1164 (2013).
137. Service, R. F. Gently Does It. *Science* **343,** 1094–1097 (2014).
138. Rittman, M., Frischherz, M., Burgmann, F., Hartley, P. G. & Squires, A. Direct visualisation of lipid bilayer cubic phases using Atomic Force Microscopy. *Soft Matter* **6,** 4058–4061 (2010).
139. Wadsäter, M., Barauskas, J., Nylander, T. & Tiberg, F. Nonlamellar lipid liquid crystalline model surfaces for biofunctional studies. *Soft Matter* **9,** 8815–8819 (2013).
140. Seddon, J. M. & Templer, R. H. Cubic Phases of Self-Assembled Amphiphilic Aggregates. *Philosophical Transactions of the Royal Society A: Mathematical, Physical and Engineering Sciences* **344,** 377–401 (1993).
141. Seddon, J. M., Robins, J., Gulik-Krzywicki, T. & Delacroix, H. Inverse micellar phases of phospholipids and glycolipids. *Physical Chemistry Chemical Physics* **2,** 4485–4493 (2000).
142. Almsherqi, Z. A., Kohlwein, S. D. & Deng, Y. Cubic membranes: a legend beyond the Flatland* of cell membrane organization. *J. Cell Biol.* **173,** 839–844 (2006).
143. Guichard, P. *et al.* Direct visualization of dispersed lipid bicontinuous cubic phases by cryo-electron tomography. *Nature Communications* **6,** 1–8 (2015).
144. Gumí-Audenis, B. *et al.* Custom AFM for X-ray beamlines: in situ biological investigations under physiological conditions. *J Synchrotron Radiat* **22,** 1364–1371 (2015).
145. Fong, C., Le, T. & Drummond, C. J. Lyotropic liquid crystal engineering–ordered nanostructured small molecule amphiphile self-assembly materials by design. *Chemical Society Reviews* **41,** 1297–1322 (2012).
146. Hoogenboom, B. W. *et al.* Quantitative dynamic-mode scanning force microscopy in liquid. *Applied Physics Letters* **88,** 193109 (2006).
147. Briggs, J., Chung, H. & Caffrey, M. The Temperature-Composition Phase Diagram and Mesophase Structure Characterization of the Monoolein/Water System. *Journal de Physique II* **6,** 723–751 (1996).
148. McGovern, M. E., Kallury, K. M. R. & Thompson, M. Role of Solvent on the

Silanization of Glass with Octadecyltrichlorosilane. *Langmuir* **10,** 3607–3614 (1994).

149. Wilson, N. R. & Macpherson, J. V. Carbon nanotube tips for atomic force microscopy. *Nature Nanotech* **4,** 483–491 (2009).
150. Bruinsma, R. Elasticity and excitations of minimal crystals. *Journal de Physique II* **2,** 425–451 (1992).
151. Cherezov, V., Clogston, J., Misquitta, Y., Abdel-Gawad, W. & Caffrey, M. Membrane Protein Crystallization In Meso: Lipid Type-Tailoring of the Cubic Phase. *Biophysical Journal* **83,** 3393–3407 (2002).
152. Robinson, A. J., Richards, W. G., Thomas, P. J. & Hann, M. M. Behavior of cholesterol and its effect on head group and chain conformations in lipid bilayers: a molecular dynamics study. *Biophysical Journal* **68,** 164–170 (1995).
153. Gillams, R. J., Nylander, T., Plivelic, T. S., Dymond, M. K. & Attard, G. S. Formation of inverse topology lyotropic phases in dioleoylphosphatidylcholine/oleic acid and dioleoylphosphatidylethanolamine/oleic acid binary mixtures. *Langmuir* **30,** 3337–3344 (2014).
154. Lukoyanova, N., Hoogenboom, B. W. & Saibil, H. R. The membrane attack complex, perforin and cholesterol-dependent cytolysin superfamily of pore-forming proteins. *J. Cell. Sci.* jcs.182741 (2016). doi:10.1242/jcs.182741
155. Nagamune, H. *et al.* Intermedilysin, a novel cytotoxin specific for human cells secreted by Streptococcus intermedius UNS46 isolated from a human liver abscess. *Infection and Immunity* **64,** 3093–3100 (1996).
156. Johnson, B. B. *et al.* Modifications in perfringolysin O domain 4 alter the cholesterol concentration threshold required for binding. *Biochemistry* **51,** 3373–3382 (2012).
157. Ramachandran, R., Heuck, A. P., Tweten, R. K. & Johnson, A. E. Structural insights into the membrane-anchoring mechanism of a cholesterol-dependent cytolysin. *Nat. Struct. Biol.* **9,** 823–827 (2002).
158. Hotze, E. M. *et al.* Arresting pore formation of a cholesterol-dependent cytolysin by disulfide trapping synchronizes the insertion of the transmembrane beta-sheet from a prepore intermediate. *J. Biol. Chem.* **276,** 8261–8268 (2001).
159. Czajkowsky, D. M., Hotze, E. M., Shao, Z. & Tweten, R. K. Vertical collapse of a cytolysin prepore moves its transmembrane beta-hairpins to the membrane. *EMBO J.* **23,** 3206–3215 (2004).
160. Shatursky, O. *et al.* The mechanism of membrane insertion for a cholesterol-dependent cytolysin: a novel paradigm for pore-forming toxins. *Cell* **99,** 293–299 (1999).
161. Giddings, K. S., Zhao, J., Sims, P. J. & Tweten, R. K. Human CD59 is a receptor for the cholesterol-dependent cytolysin intermedilysin. *Nat. Struct. Mol. Biol.* **11,** 1173–1178 (2004).
162. LaChapelle, S., Tweten, R. K. & Hotze, E. M. Intermedilysin-receptor interactions during assembly of the pore complex: assembly intermediates increase host cell

susceptibility to complement-mediated lysis. *J. Biol. Chem.* **284,** 12719–12726 (2009).

163. Egelman, E. H. The Current Revolution in Cryo-EM. *Biophysical Journal* **110,** 1008–1012 (2016).
164. Leung, C. *et al.* Stepwise visualization of membrane pore formation by suilysin, a bacterial cholesterol-dependent cytolysin. *Elife* **3,** e04247 (2014).
165. Mulvihill, E., van Pee, K., Mari, S. A., Müller, D. J. & Yildiz, Ö. Directly Observing the Lipid-Dependent Self-Assembly and Pore-Forming Mechanism of the Cytolytic Toxin Listeriolysin O. *Nano Lett.* **15,** 6965–6973 (2015).
166. Yilmaz, N. & Kobayashi, T. Visualization of Lipid Membrane Reorganization Induced by a Pore-Forming Toxin Using High-Speed Atomic Force Microscopy. *ACS Nano* **9,** 7960–7967 (2015).
167. Czajkowsky, D. M., Sun, J. & Shao, Z. Single molecule compression reveals intra-protein forces drive cytotoxin pore formation. *Elife* **4,** e08421 (2015).
168. Johnson, S., Brooks, N. J., Smith, R. A. G., Lea, S. M. & Bubeck, D. Structural Basis for Recognition of the Pore-Forming Toxin Intermedilysin by Human Complement Receptor CD59. *CellReports* **3,** 1369–1377 (2013).
169. Hung, W.-C., Lee, M.-T., Chen, F.-Y. & Huang, H. W. The condensing effect of cholesterol in lipid bilayers. *Biophysical Journal* **92,** 3960–3967 (2007).
170. Hill, A. *et al.* Protection of erythrocytes from human complement-mediated lysis by membrane-targeted recombinant soluble CD59: a new approach to PNH therapy. *Blood* **107,** 2131–2137 (2006).
171. Song, C., Wang, P. & Makse, H. A. A phase diagram for jammed matter. *Nature* **453,** 629–632 (2008).
172. Prieto, L., He, Y. & Lazaridis, T. Protein arcs may form stable pores in lipid membranes. *Biophysical Journal* **106,** 154–161 (2014).
173. Giddings, K. S., Johnson, A. E. & Tweten, R. K. Redefining cholesterol's role in the mechanism of the cholesterol-dependent cytolysins. *Proc. Natl. Acad. Sci. U.S.A.* **100,** 11315–11320 (2003).
174. Dufrêne, Y. F., Martínez-Martín, D., Medalsy, I., Alsteens, D. & Müller, D. J. Multiparametric imaging of biological systems by force-distance curve–based AFM. *Nat Meth* **10,** 847–854 (2013).
175. Kosmalska, A. J. *et al.* Physical principles of membrane remodelling during cell mechanoadaptation. *Nature Communications* **6,** 7292 (2015).
176. Pfreundschuh, M. *et al.* Identifying and quantifying two ligand-binding sites while imaging native human membrane receptors by AFM. *Nature Communications* **6,** 8857 (2015).